Diss. ETH No. 20448

Assessment of Therapeutic, Scatter, and Imaging Doses in Radiation Oncology and Implications for Cancer Risk

A dissertation submitted to
ETH Zürich

for the degree of
Doctor of Sciences

presented by

Roger Antoine Hälg

Dipl. Phys. ETH Zürich
born 15. August 1979

citizen of
Niederhelfenschwil (St. Gallen)

accepted on the recommendation of

Prof. Dr. Antony J. Lomax, Examiner
Prof. Dr. Uwe Schneider, Co-Examiner
Prof. Dr. Bertram Batlogg, Co-Examiner
PD Dr. Raphaël Moeckli, Co-Examiner

2012

To my family.

Contents

Abstract

In this thesis the assessment of therapeutic, stray, and imaging doses for a typical treatment course of a patient in radiation oncology is presented and the implications for cancer risk are discussed.

Contemporary radiotherapy treatment techniques such as intensity-modulated radiation therapy and volumetric modulated arc therapy, are believed to increase radiation-induced malignancies. They are limited by prolonged beam-on times needed to deliver the same dose to the target and larger volumes are irradiated with low doses. High energy photon ($> 10\,\mathrm{MV}$) and proton therapy beams cause the production of secondary neutrons. This leads to an unwanted dose contribution, which can be considerable for tissues outside the target volume in terms of the long term health of cancer patients. Due to the high biological effectiveness of neutrons concerning cancer induction, even small neutron doses can be important. In order to quantify the stray dose to a patient for radiation treatment techniques, measurements inside phantoms, representing the patient, are necessary. To date published reports on neutron dose measurements were performed free in air or on the surface of phantoms and the doses are expressed in terms of personal dose equivalent or ambient dose equivalent. Another source of dose to the whole body of the patient is deposited energy from imaging procedures in image-guided radiation therapy. A steadily increasing number of imaging modalities is used in the process of the patient setup in clinical routine of radiation therapy to achieve a reproducible positioning of the patient. The full benefit of the increased precision of contemporary treatment techniques in the application of the radiation dose to the tumour can only be exploited if the accuracy of the patient positioning is guaranteed. However, the achieved gain in the accuracy of patient position comes at the cost of new sources of dose contributions to the integral dose of a patient.

To quantify all the dose contributions involved in a typical course of

treatment of a patient in radiation oncology, measurements of neutron and photon dose from different treatment techniques and therapy machines as well as photon dose from typical imaging procedures were performed in an anthropomorphic phantom. The experimental setup and the treatment intention was the same for all dose measurements. This allows a direct combination of stray and imaging dose distributions for further analysis.

In order to perform local neutron dose measurements at 23 positions in terms of neutron dose equivalent inside an anthropomorphic phantom, a new field calibration procedure for poly(allyl diglycol carbonate) track etch dosimeters was developed in this thesis. Calibration factors were derived to account for the spectral changes in the neutron fluence for different radiation therapy beam qualities and depth in the phantom. The neutron spectra used for the calculation of the calibration factors were determined in different depths by Monte Carlo simulations for the investigated radiation qualities. These spectra were used together with the energy dependent response function of the track etch detectors to account for the spectral changes in the neutron fluence. The measured neutron dose was compared with respect to treatment technique, therapy machines, and radiation quality. The investigated treatment techniques for this comparison were 3D-conformal, volumetric modulated arc therapy, intensity-modulated radiation therapy, spot scanning, and passive scattering. The measurements were performed using linear accelerators from the manufacturers Varian, Elekta, and Siemens. The applied radiation qualities were photons and protons. Additional measurements of neutron dose equivalent were performed in a geometrical phantom for an open and an intensity-modulated high-energy photon field inside and outside of the treatment field. This was done in order to investigate the dependency of the neutron dose equivalent on the increase of the beam-on time for intensity modulation, as it is commonly assumed that the neutron dose scales with the beam-on time. The dose distributions from photon therapy and imaging beams were measured with individually calibrated thermoluminescent dosimeters at 184 locations in the same phantom. The dose distributions from 6 MV beams were compared in terms of treatment technique and therapy machine. The measurements were performed using the irradiation techniques 3D-conformal, intensity-modulated radiation therapy, volumetric modulated arc therapy, helical TomoTherapy, stereotactic radiotherapy, hard wedges, and flattening filter-free radiotherapy on linear accelerators from the manufacturers Elekta, Siemens, and Varian and on a CyberKnife and a TomoTherapy unit from Accuray. The dose distributions from treatment machine-mounted imaging devices and from

computed tomography scanners from GE Healthcare were determined and the resulting organ and effective doses were calculated. The list of investigated imaging techniques consisted of cone beam computed tomography (kilo- and megavoltage), megavoltage fan beam computed tomography, kilo- and megavoltage planar imaging, planning computed tomography with and without gating methods, and planar scout views.

Neutron dose equivalent varied between 2 µSv and 3 mSv per treatment Gray over all measurements. Only small differences were found when comparing treatment techniques, but substantial differences were observed between the linear accelerator models. The neutron dose for proton therapy was higher than for photons in general and in particular for double scattered protons. Close to the target volume, the stray doses from intensity-modulated photon treatments (including flattening filter-free) were below the dose from a static treatment plan, whereas the CyberKnife showed a larger dose by a factor of two. Far away from the treatment field, the dose from intensity-modulated treatments showed an increase in stray dose of about 50 % compared to the 3D-conformal treatment. For the flattening filter-free photon beams, the stray dose far away from the target was slightly lower than the dose from a static treatment. The CyberKnife irradiation and the treatment using hard wedges increased the stray dose by nearly a factor of three compared to the 3D-conformal treatment using open fields. It was also shown in this thesis that the dose from photon stray radiation dominates the out-of-field dose for 16 MV irradiations. The neutron stray dose was an order of magnitude lower than the out-of-field dose from photons. A conventional 3D planning CT added an effective dose of less than 1 % to the effective dose from treatment stray radiation outside of the treated volume, whereas a 4D planning CT resulted in an increase of 10 %. For a daily setup of the patient with two planar kilovoltage images or with a fan beam CT at the TomoTherapy unit, an additional effective dose of less than 0.5 % and 1 % was measured, respectively. Using kilovoltage or megavoltage radiation to obtain cone beam computed tomography scans lead to an additional dose of 5 % to 30 %. For treatment verification images performed once per week using double exposure technique, an additional effective dose of up to 20 % was measured.

The extended calibration procedure for neutron dosimetry presented in this thesis showed that it is possible to use track etch detectors for measurements of local neutron dose equivalent inside an anthropomorphic phantom by accounting for spectral changes in the neutron fluence. The overall neutron dose equivalent measured for double scattered proton beams was an order of magnitude lower than the stray dose of a treat-

ment using 6 MV photons. Neutron dose equivalent measured for spot scanning delivery of proton beams was substantially below the dose from double scattering beam lines far away from the treated volume, suggesting that the contribution of the secondary neutron dose to the integral dose of a cancer patient is small. It was shown that the neutron dose equivalent, which a patient receives during an intensity-modulated radiotherapy treatment, does not scale with the ratio of the beam-on time relative to an open field irradiation. Outside the treated volume at larger depth, 35 % less neutron dose equivalent was delivered than expected. Therefore, the predicted increase of second cancer induction rates due to neutrons from intensity-modulated treatment techniques might have been overestimated in the past. The photon dose measurements showed that the dose outside the treated volume is influenced by several sources. Therefore when comparing different treatment techniques, the dose ratios vary with distance from the isocenter. The effective dose outside the treated volume of intensity-modulated treatments with or without flattening filter was 10 % to 30 % larger when compared to 3D-conformal radiotherapy. This dose increase was much lower than the beam-on time scaled effective dose from a static treatment. Daily setup imaging using kilovoltage planar images or TomoTherapy megavoltage fan beam CT imaging can be used as a standard procedure in clinical routine. Daily kilovoltage and megavoltage cone beam computed tomography setup imaging should be applied on an individual or indication based protocol. It was found that image-guided radiation therapy does not necessarily increase the dose to the patient. For example a complete volumetric modulated arc therapy treatment course including planning CT and daily kilovoltage planar setup imaging reduced the effective dose by around 7 % when compared to a treatment without image guidance using four fields, a planning CT, and weekly treatment verification images.

To our knowledge, the presented dose catalogue is to date one of the most extensive in the literature and it is the only one that combines imaging and stray dose to evaluate whole-body dose distributions for image-guided radiotherapy. This work provides a comprehensive basis for the modelling of radiation related cancer risk in modern radiation oncology.

Zusammenfassung

Die vorliegende Dissertation befasst sich mit der dosimetrischen Messung von Therapie-, Streu- und Bildgebungsdosen für eine typische Behandlung eines Patienten in der Radio-Onkologie und diskutiert die Konsequenzen für das Krebsrisiko.

Moderne radiotherapeutische Behandlungstechniken wie intensitätsmodulierte Radiotherapie oder volumetrisch modulierte Bogentherapie können das Risiko eines strahleninduzierten Krebs (gegenüber der herkömmlichen 3D-konformen Bestrahlung) erhöhen. Sie benötigen auf der einen Seite eine längere Bestrahlungszeit für dieselbe am Tumor applizierte Dosis und vergrössern andererseits das periphere Volumen, das ungewollt mit niedrigen Dosen belegt wird. Des weiteren birgt der zusätzliche Dosisbeitrag durch sekundäre Neutronen, die bei der Verwendung von Protonen oder Photonen mit nominellen Energien von mehr als 10 MV entstehen, die Gefahr von Spätfolgen im Gewebe ausserhalb des Zielvolumens. Aufgrund der hohen relativen biologischen Wirksamkeit bezüglich der Krebsinduktion, können hier bereits niedrige Neutronendosen von Bedeutung sein. Zur Bestimmung der Streudosis, bedarf es Messungen im Inneren eines Phantoms, welches den Patienten ersetzt. Aktuelle Studien beschränken sich allerdings meist auf die Messung von Neutronendosen in Luft oder an der Oberfläche von Phantomen. Die Dosis wird dabei in Personenäquivalentdosis oder in Umgebungsäquivalentdosis angegeben. Da der Anspruch an die Genauigkeit der Positionierung in modernen Therapiemethoden immer grösser wird, finden bildgebende Methoden zunehmend Anwendung. Nur so ist es möglich das ganze Potential dieser neuen Techniken auszuschöpfen und die Dosis hoch konform im Tumor zu deponieren. Mit dieser Genauigkeitsverbesserung bei der Positionierung des Patienten geht ein zusätzlicher Beitrag zur integralen Dosis einher. Um alle Dosisbeiträge einer typischen Bestrahlung bestimmen zu können, wurden in dieser Arbeit Messungen der Neutronen-

und Photonendosis von verschiedenen Bestrahlungstechniken an unterschiedlichen Behandlungsgeräten, sowie Messungen der Photonendosis bei üblicherweise eingesetzten Bildgebungsverfahren in einem anthropomorphen Phantom für eine komplette therapeutische Behandlungsserie durchgeführt. Die experimentellen Methoden und die gewählte Behandlungsabsicht waren identisch für alle vorgestellten Messungen. Dies erlaubt eine direkte Kombination aller Streu- und Bildgebungsdosen für weitere Untersuchungen.

Zur lokalen Messung der Neutronendosis als Äquivalentdosis wurde eine Methode zur Feldkalibrierung von Ätzspur-Detektoren aus Polyallyldiglykolcarbonat entwickelt. Für die Neutronendosismessungen wurden insgesamt 23 Messpositionen in einem anthropomorphen Phantom ausgewählt. Die spektrale Änderung in der Neutronenfluenz mit der Tiefe im Phantom und die verschiedenen Therapiestrahlqualitäten wurden in Kalibrationsfaktoren erfasst. Dafür wurden Neutronenspektren in verschiedenen Tiefen im Phantommaterial mit Hilfe von Monte Carlo Simulationen für jede Strahlqualität generiert. Diese Spektren wurden zusammen mit der energieabhängigen Antwort der Ätzspur-Detektoren verwendet um die spektralen Veränderungen in der Neutronenfluenz für die Messung zu berücksichtigen. Die gemessenen Neutronendosen wurden bezüglich der Therapietechnik, des Bestrahlungsgerätes und bezüglich der Strahlqualität verglichen. Bei den untersuchten Techniken handelte es sich um 3D-konforme Bestrahlung, intensitätsmodulierte Strahlentherapie, volumetrisch modulierte Bogentherapie, sowie um aktive und passive Protonentherapie. Es wurden Elektronen-Linearbeschleuniger von den Herstellern Elekta, Siemens und Varian sowie Photonen- und Protonenstrahlen untersucht. Zusätzliche Neutronendosismessungen wurden in einem geometrischen Phantom für ein offenes und ein intensitätsmoduliertes hoch energetisches Photonenfeld innerhalb und ausserhalb des primären Bestrahlungsfeldes durchgeführt. Dabei wurde der Zusammenhang zwischen der Zunahme der benötigten Bestrahlungszeit für die Intensitätsmodulation und der Neutronendosis untersucht, da gegenwärtig angenommen wird, dass die Neutronendosis direkt proportional mit der Bestrahlungszeit zunimmt. In einer weiteren Messreihe wurden ganzkörper Dosisverteilungen für Therapie- und Bildgebungsbestrahlungen mittels Photonen mit individuell kalibrierten Thermolumineszensdosimetern an 184 Positionen im genannten Phantom gemessen. Die Dosismessungen von 6 MV Photonenstrahlen wurden bezüglich der verwendeten Therapietechnik und des Bestrahlungsgerätes verglichen. Die eingesetzten Bestrahlungstechniken waren 3D-konforme Bestrahlung, intensitätsmodu-

lierte Radiotherapie, volumetrisch modulierte Bogentherapie, spiralförmige TomoTherapie, stereotaktische Radiotherapie, Strahlentherapie mit Keilen sowie Strahlentherapie ohne Ausgleichskörper. Als Bestrahlungsgeräte für diese Messreihe wurden Elektronen-Linearbeschleuniger der Herstellern Elekta, Siemens und Varian, sowie ein CyberKnife und ein TomoTherapie Gerät der Firma Accuray herangezogen. Die Dosisverteilungen von Bildgebungsgeräten, welche am Bestrahlungsgerät montiert sind und von Computertomographen der Firma GE Healthcare wurden untersucht um die resultierenden Organdosen sowie die effektiven Dosen zu ermitteln. Als Bildgebungstechniken wurden Computertomographie mit Kegelstrahlgeometrie mit Kilo- und Megavolt Photonenstrahlung, Megavolt Computertomographie mittels Fächerstrahlgeometrie, planare Bildgebung mittels Kilo- und Megavolt Strahlung, Computertomographie zur Therapieplanung mit und ohne Atmungssteuerung sowie planaren Übersichtsaufnahmen untersucht.

Die Neutronenäquivalentdosis variierte zwischen 2 µSv und 3 mSv pro Behandlungs-Gray über alle Messungen. Zwischen den Behandlungstechniken waren die gemessenen Unterschiede klein. Die verschiedenen Modelle der Bestrahlungsgeräte hingegen wiesen substantielle Unterschiede auf. Die Neutronendosis war generell höher bei der Protonentherapie als bei der Therapie mit Photonen und innerhalb der Protonentherapien war die Neutronendosis der passiven Bestrahlungstechnik höher als der aktiven. Nahe vom Bestrahlungsfeld war die Photonenstreudosis für intensitätsmodulierte Therapie mit Ausgleichskörper kleiner als die Streudosis einer statischen Bestrahlung, wohingegen die Bestrahlung am CyberKnife eine etwa doppelt so hohe Dosis zeigte. Weit weg vom Bestrahlungsfeld lag die Dosis der intensitätsmodulierten Techniken etwa 50 % über der der 3D-konformen Bestrahlung. Die Photonenfelder ohne Ausgleichskörper führten zu einer leicht verminderten Streudosis weit weg vom Zielvolumen verglichen mit der statischen Bestrahlung. Die Bestrahlung am CyberKnife und die Behandlung mit Keilen erhöhte die Streudosis um das Dreifache verglichen mit der 3D-konformen Behandlung mittels offenen Feldern. In der vorliegenden Arbeit wurde zudem gezeigt, dass die Photonenstreudosis eines 15 MV Strahls die Dosis ausserhalb des Bestrahlungsfeldes dominiert. Ausserhalb des Bestrahlungsvolumens war die Streudosis durch Neutronen um eine Grössenordnung kleiner. Bei den bildgebenden Verfahren resultierte eine konventionelle 3D Computertomographie zur Therapieplanung in einer effektiven Dosis von weniger als 1 % zusätzlich zur Streudosis der Therapie ausserhalb des bestrahlten Volumens. Bei einer zeitaufgelösten Computertomographie lag die Erhöhung

der effektiven Dosis ausserhalb des bestrahlten Volumens bei 10 %. Bei einer täglichen Aufnahme von planaren Bildern mittels Kilovolt Strahlung oder einer Fächerstrahl-Computertomographie am TomoTherapie Gerät für die Patientenpositionierung entstand eine zusätzliche effektive Dosis von weniger als 0.5 %, respektive 1 %. Bei der Aufnahme mittels Computertomographie mit Kegelstrahlgeometrie und Kilo- oder Megavolt Strahlung lag die zusätzliche Dosis zwischen 5 % und 30 %. Für wöchentliche Aufnahmen zur Verifikation des Bestrahlungsfelds mittels Doppelbelichtungstechnik, erhöht sich die effektive Dosis um bis zu 20 %.

Die erweiterte Methode zur Feldkalibrierung der Neutronendosimeter, welche in dieser Arbeit vorgestellt wurde, zeigte, dass es dann möglich ist mit Hilfe von Ätzspur-Detektoren lokale Neutronenäquivalentdosen in einem anthropomorphen Phantom zu messen, wenn die spektralen Veränderungen in der Neutronenfluenz berücksichtigt werden. Die Äquivalentdosis der Neutronen welche für passiv applizierte Protonenstrahlen gemessen wurde, war eine Grössenordnung kleiner als die Streudosis bei einer Bestrahlung mit 6 MV Photonen. Für Protonen, die mittels aktiver Bestrahlungstechnik appliziert wurden, wurde eine wesentlich tiefere Dosis gemessen weit weg vom Zielvolumen als für die Technik mit passiv gestreuten Protonen, was einem kleinen Beitrag von Neutronen zur integralen Dosis eines Radiotherapiepatienten entspricht. Es wurde gezeigt, dass die Neutronenäquivalentdosis für einen Patienten, der mit intensitätsmodulierter Photonentherapie behandelt wird, nicht mit dem Verhältnis der Bestrahlungszeiten zwischen intensitätsmodulierter und statischer Bestrahlung mit offenen Feldern skaliert. Ausserhalb des bestrahlten Volumens in grossen Tiefen wurde eine um 35 % kleinere Neutronenäquivalentdosis gemessen als erwartet. Daher ist anzunehmen, dass der Anstieg der Erkrankungen an neutroneninduziertem Krebs in intensitätsmodulierten Behandlungen bisher überschätzt wurde. Die Messungen der Photonendosis zeigten, dass die Dosis ausserhalb des bestrahlten Volumens von mehreren Faktoren abhängig ist. Wenn man verschiedene Bestrahlungstechniken miteinander vergleicht, variieren daher die Verhältnisse der Dosen als Funktion des Abstandes vom Bestrahlungsfeld. Die effektive Dosis ausserhalb des bestrahlten Volumens war 10 % bis 30 % höher für intensitätsmodulierte Behandlungen mit oder ohne Ausgleichskörper verglichen mit 3D-konformer Radiotherapie. Dieser Dosisanstieg ist viel kleiner als die mit dem Verhältnis der Bestrahlungszeiten skalierte effektive Dosis einer statischen Behandlung. Die tägliche Anwendung von planarer Kilovolt Bildgebung oder der Megavolt Fächerstrahl-Computertomographie am TomoTherapie Gerät zur Patientenpositionie-

rung kann als Standardprozedur in der klinischen Routine eingesetzt werden. Hingegen sollte die tägliche Anwendung von Kilo- oder Megavolt Photonenstrahlung für Computertomographien mittels einer Kegelstrahlgeometrie zur Überprüfung der Patientenpositionierung nur nach einer individuellen oder indikationsspezifischen Abklärung durchgeführt werden. Die hier vorgestellten Untersuchungen über die Dosen in der bildgebungsgestützten Radiotherapie haben gezeigt, dass die Patientenpositionierung mit moderner Bildgebung nicht zwangsweise zu einer erhöhten peripheren Dosis führen muss. Zum Beispiel war die effektive Dosis für eine komplette Behandlung mit volumetrisch modulierter Bogentherapie, einer Computertomographie zur Bestrahlungsplanung und täglichen Setupaufnahmen mittels planarer Kilovolt Bildern um etwa 7 % kleiner als die resultierende Dosis von einer nicht bildgebungsgestützten Bestrahlung, einer Computertomographie zur Bestrahlungsplanung und wöchentlichen Verifikationsaufnahmen mit dem Therapiestrahl.

Der in dieser Doktorarbeit vorgestellte Dosiskatalog ist einer der ausführlichsten die derzeit verfügbar sind und der einzige, der die Kombination von Bildgebungs- und Streudosen der Therapie ermöglicht um ganzkörper Dosisverteilungen zu beurteilen. Diese Arbeit bietet eine umfassende Grundlage für die Modellierung des strahleninduzierten Krebsrisikos in der modernen Radio-Onkologie.

Chapter 1

Background and Motivation

Over the last few decades, continuous efforts in research and development for the treatment of cancer patients have lead to new modalities and further optimised techniques. This is true for all three fundamental approaches in cancer treatment, which are surgery, chemotherapy, and radiation therapy. The surgical resection of the tumour is one of the most important approaches in cancer therapy and benefits from advances in modern interventional procedures. In chemotherapy, anti-neoplastic drugs kill rapidly dividing cells to eliminate the tumour. Progress in the understanding of cancer cell properties and in the design of chemotherapeutic drugs has allowed the targeting of abnormal proteins in cancer cells. The third essential approach in treating cancer patients is the application of ionising radiation to kill cancer cells. Although the underlying physics of the radiation and its interaction with matter cannot be changed, the techniques used to deliver the radiation dose to the patient have been constantly improved. Radiation therapy is a very common procedure in cancer therapy: approximately half of the long-term survivors of a malignant disease receive radiotherapy as part of their treatment [1]. In general, long-term survivors of radiation therapy treatments have a high incidence of chronic health problems including radiation induced malignancies [1]. Therefore radiation therapy is sometimes considered a double-edged sword. Ionising radiation can help in curing cancer by killing malignant cells, but it can also induce cancer by causing mutations of the genome in healthy cells [2, 3]. These second primary cancers, known as second cancers, are treatment induced malignancies with a different histology than the initially treated primary cancer. Second cancers must be distinguished from relapses of the initial disease with the same histology and metastases which are not primary cancers. In the United

States second cancers have been reported to be the fourth or fifth most common cancer [4]. For a radiotherapy patient, an increase in the dose to the healthy tissue from the treatment can increase the risk for a radiation induced second cancer [5, 6]. For the treatment of childhood cancers with radiation therapy, an increase in the dose outside the tumour can have a larger impact on the rate of second cancers than for adults. The five-year survival rate for children has been reported to be higher than for adult patients [7] and therefore the relative number of persons at risk for developing a second cancer is higher too. Bhatia and Sklar reported a 3 to 6 fold increased risk of a second cancer for childhood cancer survivors, when compared with the background incidence of cancer in the general population and this risk continues to increase as the cohort ages [8].

Since modern intensity modulation techniques have only been employed for a short time in radiation oncology compared to the latency time for solid tumour induction and the time needed to perform meaningful epidemiological studies, the long term risk of these delivery techniques has not yet been determined and will not be possible for many years [9]. It is therefore necessary to deliberate about whether these techniques should be applied extensively or not by using theoretical predictions. These predictions must be based on systematic investigations on the determinable quantities involved in radiation induced carcinogenesis according to our current knowledge. This is a common approach in other rapidly advancing disciplines in medicine [10]. The purpose of this doctoral thesis is to give a new comprehensive picture about the problem of overall dose to the patient for all relevant processes involved in a typical treatment course in radiation oncology. This catalogue of radiation dose distributions in the whole patient can be used to determine the corresponding radiation risk.

Newly developed radiation delivery techniques allow the application of therapeutic radiation with increased precision. This is of great importance as it is not possible to irradiate solely cancerous tissue. Part of the healthy tissue will always be irradiated concomitant to the target volume. Therefore it is essential to minimise the dose and the irradiated volume outside the tumour while still treating the whole target volume. The unwanted dose to the healthy tissue outside of the target volume is usually called the peripheral or out-of-field dose. One approach to increase the precision of the application of the radiation to the tumour is to use intensity-modulated beams of ionising radiation, called intensity-modulated radiation therapy (IMRT) [11]. The dynamic modulation of the radiation fluence allows the adaptation of the deposited dose to the individual tumour target volume of a patient with high conformity. With

this technique it is possible to produce concave dose distributions to follow the contour of the target volume, which is not possible with conventional radiotherapy treatment techniques. This can be very important for the sparing of healthy tissue. For instance, if the target volume is located around an organ unaffected by the disease which should not be irradiated, the organ is considered at risk. Most of the patients in radiation oncology are treated with photon beams.

Another possibility to achieve high conformity of the dose distribution to the target volume is the application of charged particles as the radiation source. Electrically charged particles interact with matter in a different way than photons, which leads to substantial differences in the deposition of the dose with depth in material. Because of their small mass, electrons are suitable to treat superficial diseases, whereas heavy charged particles like protons and heavy ions are convenient to treat deep seated tumours. The interaction of heavy charged particles with matter is described by the Bethe formula [12], which explains the appearance of the so-called Bragg peak, named after William Henry Bragg, at the end of the range of a heavy charged particle passing trough matter. The fundamental difference in the deposition of the dose with depth in matter for heavy charged particles compared to a photon beam is shown in Figure 1.1. Depicted are so-called percentage depth dose (PDD) curves in water for a photon beam with a nominal energy of 6 MV and proton and carbon ion beams with energies of 160 MeV and 305 MeV per nucleon, respectively.

The finite range of heavy charged particles gives new possibilities to conform the dose to the target volume. This means that not only the lateral collimation of the beam can be used to define the irradiated volume but also the range of the particles. Such an adaptation of the dose to the distal edge of the target is not possible with photon beams. In addition to the physical benefits of heavy charged particle beams, intensity modulation techniques are used to further optimise the dose distribution. The Paul Scherrer Institut (PSI) in Villigen, Switzerland, is one of the leading institutions in the application and advancement of proton therapy worldwide. Pioneering work was done at PSI for the implementation of the proton spot scanning technique [16] and intensity-modulated proton therapy (IMPT) [17, 18] into clinical routine.

For radiation therapy using bremsstrahlung photon beams, the peripheral dose is mostly determined by the dose from scattered photons. In proton and heavy ion radiation therapy the peripheral dose is not dominated by the dose deposited by scattered primary radiation, but by secondary particles produced in interactions of the primary particles with

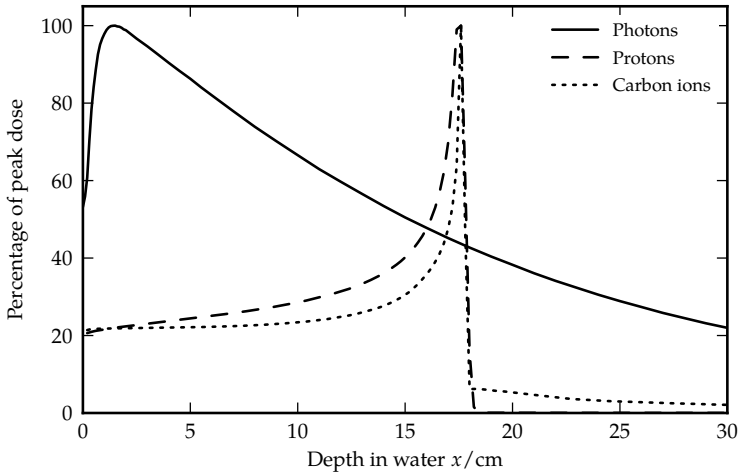

Figure 1.1: Percentage depth dose curve of measured 6 MV photon and Monte Carlo simulated proton (160 MeV) and carbon ion (305 MeV per nucleon) beams in water. The curves for the proton and the carbon ion beams show a Bragg peak at the end of the range of the primary particles. The depth dose curve for the photon beam was measured using an ionisation chamber (Thimble Chamber, PTW, Freiburg, Germany) and the heavy charged particle beams were simulated using the FLUKA Monte Carlo code [13–15].

the beam delivery system or with the patient. The most important contribution to the peripheral dose arises from neutrons produced in nuclear interactions of the primary particles with matter. These secondary neutrons interact in a different way with matter than the primary particles, as they carry no electrical charge. This leads to an increased range of neutrons compared to protons and heavy ions. The original direction of propagation of neutrons is lost after only a few interactions with matter, causing dose depositions everywhere in the patient—the so-called neutron dose bath. The amount of neutron production is dependent on the technique used to produce the treatment field. For active spot scanning, the neutrons are mostly produced in the patient, as the treatment field is formed by a pencil beam which is magnetically scanned over the target volume and no beam modifying devices are necessary. For passive scattering beam lines, neutrons are produced in the beam modifying devices and in the patient. Scatterers, beam-flattening devices, collimators, and energy modulation devices are used to produce the treatment field. This scattering of the primary beam leads to an increased neutron fluence for

passive delivery techniques. The production of neutrons is not limited to proton and heavy ion beams. Photons have an energy threshold of 6 MeV to 13 MeV for most materials for the production of secondary neutrons through photonuclear interactions [19]. These photoneutrons are mainly produced in the gantry head, as high-Z materials have a larger cross section than human tissue. Therefore for therapeutic photon beams with a nominal energy of more than 10 MV, as well as for proton and heavy ion beams, an additional neutron contribution to the stray dose is added.

The additional dose from neutrons has raised concerns about a possible increase in radiation induced late effects and have been discussed within the radiotherapy community [20–22]. Several studies were performed in the last few years to determine the neutron dose with measurements and Monte Carlo simulations, but the importance of neutrons for radiation induced carcinogenesis is still unclear.

The absorbed dose from neutrons for a patient in radiotherapy is small compared to the dose from primary radiation. But because of the way neutrons interact with human tissue, already a small dose can be of importance. The dose from neutrons is deposited by secondary particles. The most important secondary particles are protons and deuterons, which are high linear energy transfer particles. These particles produce a high density of ionisations along their path and therefore the damage to cellular structures in the tissue is difficult to repair. To quantify the biological effect of a dose deposition by neutrons, the absorbed dose is weighted by radiation specific weighting factors. Weighting factors for different dosimetric quantities were introduced by the International Commission on Radiation Units & Measurements (ICRU) [23, 24] and by the International Commission on Radiological Protection (ICRP) [25, 26]. In summary, the way neutrons interact with matter, cause damage to the human tissue and the complicated dosimetric quantities needed to describe the dose from neutrons makes it difficult to assess the effects of neutrons in radiation therapy. In Chapter 2 a newly developed calibration procedure for the use of neutron dosimeters in radiotherapy is described. The neutron spectra from photon, spot scanned and double scattered proton radiotherapy are used together with the energy dependent response function of the neutron detectors to determine calibration factors to assess local neutron dose. This calibration procedure is applied in Chapter 3 to measure the stray dose from neutrons inside an anthropomorphic phantom for various radiation qualities, treatment machines, and delivery techniques in radiation therapy. The dependence of neutron dose in high-energy 3D-conformal and intensity-modulated photon radiotherapy on the beam-on time, is in-

vestigated in Chapter 4.

In radiation therapy, materials with a high density and a high atomic number (high-Z materials) are used for the collimation of the treatment beam and for shielding purposes. This blocks out a part of the beam and therefore focus the radiation into so-called treatment fields for the application to the patient. Therapeutic photon beams are usually produced using linear electron accelerators. A focused electron beam is accelerated to energies in the megaelectronvolt regime and directed onto a high-Z material target. The interaction of the electron beam with the target leads to the production of bremsstrahlung photons. This forward directed photon beam is then used to form the treatment field. The photon beam is often modified using flattening filters to produce a flat dose distribution within the treatment field. This has been done for static treatments to irradiate the tumour volume with a homogeneous dose. Contemporary treatment planning systems used to calculate the dose distribution within the patient in combination with intensity-modulated radiation therapy techniques, can handle any beam profile and thus a flattened beam profile is in principle not necessary any more. The shape of the beam is modified by collimator jaws as mentioned above. Usually multileaf collimators are used in addition to form non-rectangular treatment fields. These beam modifying devices help to apply the radiation to the patient in the needed form and to conform the dose to the tumour. Although these devices are needed to treat a patient, the photon beam will interact with every object that is in the beam path and will produce a certain amount of stray radiation. This stray radiation has a different energy and direction than the primary beam. The change of direction causes the radiation to reach the patient in anatomical regions outside of the treated volume. This dose deposition is unwanted and not of therapeutic use, but it is unavoidable. Another source of unwanted dose to the patient is the dose from leakage radiation. Conventional linear accelerators used in radiation therapy are built into a gantry which can be rotated around the isocenter, a fixed point in the treatment room. The patient is usually positioned precisely on a movable couch for the treatment, such that the isocenter lies within the target volume. The bremsstrahlung target and all the beam modifying devices are located in the gantry head which is directed towards the isocenter. Although the gantry head is shielded to minimise the radiation escaping in directions other than towards the isocenter, there is always some head leakage radiation. The constituents of the peripheral dose, are of varying importance for different regions relative to the treatment field. A coarse classification of the contributions to the peripheral dose from

patient scatter radiation, collimator scatter radiation, gantry head leakage radiation, and secondary neutrons as a function of the distance from the treatment field is illustrated in Figure 1.2. The internal patient scatter radiation is produced by the interaction of the primary beam with the patient, or for measurements, with a phantom. This part is the most important contribution to the peripheral dose and is unfortunately unavoidable [27].

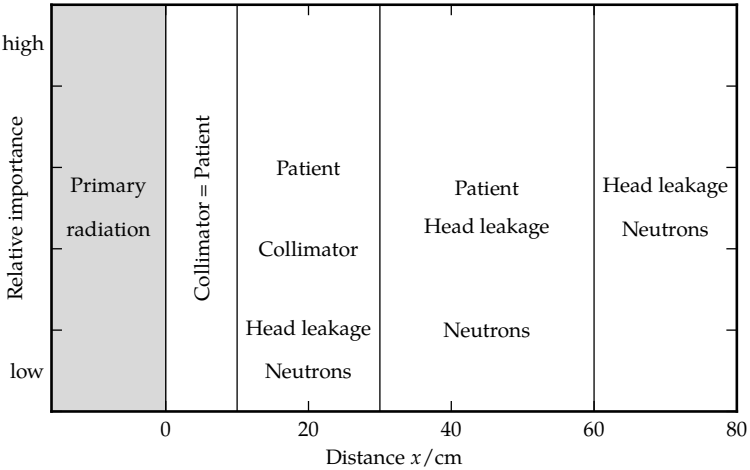

Figure 1.2: Importance of the constituents of the peripheral dose as a function of the distance to the field edge. Shown are the contributions from patient scatter radiation, collimator scatter radiation, the dose from gantry head leakage radiation, and from secondary neutrons.

Different treatment machines and delivery techniques produce different stray radiation and consequently the peripheral doses are different. The above-mentioned principles of stray radiation in photon radiation therapy are also valid for proton and heavy ion therapy. The use of beam modifying devices and the physical processes for the interactions involved are different for protons and heavy ions, but the consequences of the interaction of the primary radiation with the beam delivery system and the patient are the same. Because of the different constituents of the stray radiation and the variable use of beam modifying devices by different delivery techniques and manufacturers of treatment machines, the comparison of the out-of-field dose is complex. It is not possible to simply state that a specific treatment machine or delivery technique is better than another. In Chapter 5 systematic measurements of whole-body dose distributions

for different treatment machines and delivery techniques in photon radiotherapy are presented. The same measurement setup and treatment intention was used to compare the resulting dose distributions, which allows to assess the differences between treatment machines and techniques. Commercial treatment planning systems are used in radiotherapy institutions to calculate the dose distribution in the volume irradiated by the primary beam. The achieved accuracy is high and allows to judge the dose to the target volume and to organs at risk adjacent to the target for clinical practise in radiation oncology. On the other hand, treatment planning systems cannot be used to precisely calculate dose in organs further away from the target volume or for peripheral dose in general [28, 29]. In recent times, simulations of peripheral dose using general purpose Monte Carlo transport codes have become a valuable tool [30–33]. But to accurately determine dose to organs far away from the treated volume, measurements are still the gold standard.

For intensity-modulated treatments using photon, proton or heavy ion beams, the optimised and rather complex fluences are administered to the patient with different angles of incidence. This is necessary especially for photons, with or without intensity modulation, in order to distribute the high dose in the entrance ports over a larger volume (see Figure 1.1). This cross fire technique is the only way to deposit a higher dose in the target for deep-seated tumours than in the healthy tissue. The resulting dose distributions from intensity-modulated treatments are expected to be better in terms of tumour control probability and normal tissue complication probability [34, 35], compared to conformal treatment techniques. If the potential of intensity modulation techniques is fully exploited, there are clear therapeutic advantages for the patient. However for radiotherapy with photon beams, this gain comes at a cost. The peripheral dose to the patient is increased for several reasons. Firstly, IMRT treatments usually use more treatment fields than static treatments, also called 3D-conformal treatments [6, 36]. This increases the volume irradiated by primary photons and therefore increases the volume with a dose deposition larger than from stray radiation only. Secondly, the dose from stray radiation is increased for irradiations using intensity-modulation. As a varying part of the treatment field is blocked out by a multileaf collimator to modulate the photon fluence, the beam-on time is increased to deliver the same dose to the patient compared to a static treatment. A direct consequence of the increased beam-on time for IMRT is an increased dose from gantry head leakage.

This increase in the peripheral dose from delivery techniques using

intensity modulation and the potential consequences for the long term health of cancer patients have been subject of controversial discussions and were initiated by a paper by Followill [5]. Concerns have been raised that the application of intensity-modulated treatments can lead to an increase in radiation induced malignancies. An increased number of radiation induced second cancers related to intensity-modulated radiotherapy can be expected mainly for two reasons. Firstly, as discussed above, these new treatment techniques lead to an improved cure rate and tumour control for cancer patients. This directly leads to an increased number of cancer survivors who are at risk of developing a second cancer. Secondly, the previously mentioned prolonged beam-on time required to apply the intensity modulation compared to static treatments, leads to an increased peripheral dose. It is not a priori clear if this increase in the peripheral dose can directly be linked to an increase in second cancer risk. The application of intensity modulation changes the complete dose distribution, giving larger dose gradients and larger low dose bath compared to 3D-conformal therapy. As cancer induction by ionising radiation is not a linear function of the dose, risk estimates are more complicated to assess.

In radiation oncology there are several ways to technically implement the application of intensity modulation for a patient irradiation. Commonly the modulation of the fluence is done dynamically and therefore the required fluence is produced by processes varying with time. The application of such dynamic delivery techniques has the disadvantage that the dose distribution is susceptible to displacements in the positioning of the patient and to the motion of target structures or organs at risk. Therefore, the full benefit of treatment techniques using intensity modulation can only be exploited if the accuracy of the positioning of the target volume is guaranteed and the magnitude of external and internal motion of the patient is minimised. To verify the position of the target volume before and potentially during the treatment, more and more imaging modalities are used in the process of the patient setup. For this purpose dedicated imaging devices are mounted on the gantry or installed in the treatment room. The combination of imaging devices mounted on the gantry or in the treatment room for patient positioning and radiotherapy treatment techniques is known as image-guided radiation therapy (IGRT) [11]. With the application of pretreatment imaging procedures it is possible to correct for inter-fractional displacements in the positioning of the patient and to assure that the treatment fields are applied to the anatomical region defined during treatment planning. Imaging procedures during the irradiation can be used to correct for intra-fractional motion of the target

volume. This can be done during the beam-on time by tracking methods, or the imaging can be used to trigger the beam which is known as gating. Most of the imaging modalities used for image guidance use ionising radiation. Therefore the verification of the positioning of the patient for the treatment using imaging procedures increases the dose burden and can increase radiation-related side effects. In addition, the patient may be exposed to a higher risk of developing a second cancer. On the other hand, in the absence of position verification using imaging guidance, a misalignment of the patient could cause a higher dose delivered to the surrounding healthy tissue, which could induce side and late effects as well. The number of imaging procedures applied in clinical routine has steadily been increasing over the last few years [37], leading to the question if and how imaging doses should be managed and monitored for radiotherapy patients. Systematic measurements of imaging dose for a representative list of imaging modalities applied in contemporary radiation therapy are presented in Chapter 6. The focus of the investigation is on the dose outside of the treated volume where the relative increase in the total dose to the patient caused by imaging procedures is highest. The determined imaging doses are combined with the stray dose from radiotherapy treatments analysed in Chapter 5. This facilitates the assessment of the total dose distribution in a patient depending on the treatment modality and the imaging protocol used.

The presented measurements of dose contributions involved in radiation therapy in Chapters 3, 5 and 6 allow the assessment of all radiation doses for a typical treatment course of a patient. The dose values can be directly combined because the same anthropomorphic phantom is used for the measurements and the same treatment intention has been chosen. This phantom allows the determination of the dose in radiation sensitive organs and the resulting mean organ doses are listed in the individual chapters. The determination of organ doses is necessary for cancer risk estimations, as individual organs have a different susceptibility to radiation induced cancers [1]. The presented catalogue of radiation doses can be used to build combinations of therapy and imaging procedures and to determine the resulting dose. The outcome of this thesis is a comprehensive basis for the modelling of radiation related cancer risk in radiation oncology.

Certain commercial entities, equipment, or materials may be identified in this document in order to adequately describe an experimental procedure or concept. Such identification is not intended to imply recommendation or endorsement by the author(s), affiliated institutions, funding agen-

cies, or the ETH Zurich. Nor is it intended to imply that the entities, materials, or equipment are necessarily the best available for these purposes.

Chapter 2

Field Calibration of PADC Track Etch Detectors for Local Neutron Dosimetry in Man Using Different Radiation Qualities

Roger A. Hälg[1], Jürgen Besserer[1], Markus Boschung[2], Sabine Mayer[2], Benjamin Clasie[3], Stephen F. Kry[4], and Uwe Schneider[1,5]

[1] Institute for Radiotherapy, Radiotherapie Hirslanden AG, Aarau, Switzerland

[2] Division for Radiation Safety and Security, Paul Scherrer Institut, Villigen, Switzerland

[3] Department of Radiation Oncology, Massachusetts General Hospital, Boston, USA

[4] Department of Radiation Physics, The University of Texas M.D. Anderson Cancer Center, Houston, USA

[5] Vetsuisse Faculty, University of Zurich, Zurich, Switzerland

Submitted to
Nuclear Instruments & Methods in Physics Research Section A
2011

2.1 Introduction

In radiation therapy, treatment techniques are constantly being improved to achieve better tumour control rates and reduce the dose to healthy tissues. One of these new treatment techniques is intensity-modulated radiation therapy (IMRT) with photons [11]. There are clear therapeutic advantages using this technique, for instance the improved conformity of the dose to the target volumes [11]. On the other hand, IMRT leads to prolonged beam-on time which increases the stray dose to the healthy tissues of the patient. For treatments using high energy photon ($> 10\,\mathrm{MeV}$ nominal energy), proton or heavy ion beams, secondary neutrons are produced in the beam delivery system and the patient, adding another contribution to the dose outside the target volume [19]. The amount of absorbed dose to the patient from secondary neutrons is small compared to the primary dose to the target. However, neutron radiation has a high biological effectiveness related to cancer induction [26], therefore the resulting equivalent dose may be important in terms of the long term health of cancer patients. There are concerns about radiation induced malignancies using radiotherapy techniques that are subject to higher neutron doses compared to conventional radiotherapy treatment techniques. This is particularly important for young patients treated with radiotherapy, as they are more sensitive to ionising radiation regarding cancer induction.

In order to quantify the dose from secondary neutrons to a patient for contemporary treatment techniques using high energy photon, proton or heavy ion beams, measurements inside phantoms, representing a patient, are necessary. Depending on the treatment modality, a substantial amount of the secondary neutrons are produced in the patient [19, 38] and neutron fields in a treatment room are not homogeneous in general. There are several neutron measurements reported in the literature, but they cover measurements performed free in air or on the surface of phantoms and the doses are expressed in terms of personal dose equivalent or ambient dose equivalent [38–50]. A study by Kry et al. showed that measurements on the surface of phantoms can lead to substantial dosimetric errors when using the surface neutron dose measurements for estimating organ doses [51]. It is therefore important, to use a calibration procedure that considers the neutron spectrum of the used radiation quality and its changes with depth in matter. To quantify this spectral changes with depth, it is necessary to use an operational dose quantity based on the neutron quality factor, which allows a correction inside the phantom. This study focuses on a calibration method for measurements

of local neutron doses inside a radiotherapy phantom.

Like other neutron detectors, poly(allyl diglycol carbonate) (PADC) track etch detectors (Thermo Fisher Scientific, Waltham, MA, USA, trade name "PN3") have a different response for neutrons of different energies [52]. Therefore, the readout signal of neutron dose measurements using PADC detectors is dependent on the neutron spectrum. Firstly, the calibration of the detectors is dependent on the neutron spectrum used for determination of the sensitivity of the detector batch. Secondly, the neutron dose measurement depends on the spectrum present at the location of measurement. As a consequence, it has to be distinguished at which radiation therapy beam quality (photon, proton or heavy ion) the measurement is performed. In addition, the depth of measurement inside the phantom will also influence the readout of the detectors, as neutrons get moderated in matter and therefore the spectrum is altered.

The aim of this study was to derive calibration factors for local neutron dose equivalent measurements using PADC track etch detectors to account for the measurement geometry and the spectral changes due to treatment modality and depth inside the measurement phantom.

2.2 Materials and Methods

To assess the neutron dose for a patient in radiotherapy, it is necessary to perform local dose measurements. This is of particular importance for active proton and heavy ion therapy, where a substantial number of neutrons are produced inside the patient. As it is at the moment not possible to perform local measurements in-vivo, anthropomorphic phantoms usually replace the patient for measurements.

Neutron track etch detectors, with an appropriate calibration, allow to determine neutron dose equivalent in principle at all locations in the body. In this study, PADC detectors from the Radiation Metrology Section of the Division for Radiation Safety and Security at Paul Scherrer Institut in Villigen Switzerland were investigated for neutron dose measurements. The detectors were readout at the Paul Scherrer Institut (PSI) where PADC detectors are used for personal dosimetry and measurements. The readout of the detectors was done at PSI by optical counting of the tracks with a camera using an AUTOSCAN 60 reader [53].

In general, the determination of neutron equivalent dose requires the application of radiation weighting factors. For radiation protection purposes, it is recommended by the ICRP to use the neutron weighting factor

w_R as a function of energy to account for the dose deposition mechanisms of neutrons [25]. However, Kellerer has shown that for neutron energies below 1 MeV, w_R is suitable for small objects, but unduly large for man [54]. Although the neutron radiation weighting factor w_R has been adapted for energies below 1 MeV in the ICRP publication 103 to account for this problem [26], factors such as the size of the exposed person, the directional distribution, and spatial non-uniformity of the radiation field have been disregarded in the determination of w_R [55]. It was therefore decided to use the measurable quantity dose equivalent in this work. For the assessment of neutron dose equivalent, the effective quality factor q_E, which is the organ weighted average of the quality factor Q, as a function of neutron energy E_n was used. This quality factor was determined by Kellerer et al. [55].

The effective quality factor q_E is not only dependent on the type and energy of the incoming radiation, but also on the size of the exposed person. Equation (2.1) is a continuous approximation to the values of q_E for a sex averaged person for isotropic incidence of the radiation with energy E_n [55]

$$q_E(E_n) = 2 + 10 \cdot e^{-\frac{1}{4}(\ln(E_n))^2} + 2.5 \cdot e^{-\frac{1}{12}\left(\ln\left(\frac{E_n}{20}\right)\right)^2}. \tag{2.1}$$

Radiation equilibrium was assumed for the investigated irradiation situations, with the consequence that neutrons of constant energy produce everywhere in the phantom secondary particles with the same distribution in linear energy transfer (LET).

2.2.1 Calibration of number of tracks to neutron personal dose equivalent in water for ^{241}Am-Be

The calibration process of a batch of PADC detectors includes the irradiation of a subset of the batch (calibration detectors) with neutrons from the ^{241}Am-Be source at the PSI Calibration Laboratory [56–58]. The detectors are mounted on a reference phantom (ISO water slab phantom) defined by ISO [59–61]. The dose at the PADC detectors at the reference position was determined by using a neutron dose rate meter calibrated at the Physikalisch-Technische Bundesanstalt (PTB) in Braunschweig Germany, which is used in the laboratory as a secondary standard [56]. The measured neutron fluence at the centre of the front surface of the ISO slab phantom was converted into personal dose equivalent $H_p(10)$, using conversion coefficients for the neutron spectrum of the

^{241}Am-Be source specified by ISO [62], which include the scatter contribution of the phantom. The initial absolute calibration obtained by this procedure relates the number of tracks per area, the track density ρ_{track}, to personal neutron dose equivalent $H_{\text{p}}(10)$ per track.

This absolute calibration in terms of $H_{\text{p}}(10)$ leads to a substantial overestimation of neutron dose in an anthropomorphic phantom [54]. Therefore, the initial calibration was converted into neutron dose equivalent $H(10)$ by using the calibration factor $k_1^{\text{Am-Be}}$ for the neutron energy spectrum $\phi_{\text{Surface}}^{\text{Am-Be}}(E_{\text{n}})$ of the ^{241}Am-Be neutron source in air impinging on the phantom:

$$k_1^{\text{Am-Be}} = \frac{\int q_{\text{E}}(E_{\text{n}}) \cdot \phi_{\text{Surface}}^{\text{Am-Be}}(E_{\text{n}})\, \mathrm{d}E_{\text{n}}}{\int q_{\text{p}}(E_{\text{n}}) \cdot \phi_{\text{Surface}}^{\text{Am-Be}}(E_{\text{n}})\, \mathrm{d}E_{\text{n}}}. \tag{2.2}$$

In order to achieve this, the quality factor $q_{\text{p}}(E_{\text{n}})$ used for the determination of personal dose equivalent $H_{\text{p}}(10)$, was calculated by multiplication of the ambient quality factor $q^*(E_{\text{n}})$ (taken from a study by Kellerer [54]) with the energy dependent ratio of the conversion coefficients for personal dose equivalent and ambient dose equivalent taken from an IAEA technical report [63].

2.2.2 Spectrum specific calibration

The PADC response R, normalised to the ^{241}Am-Be spectrum, is energy dependent. Therefore, if the detector is used in a neutron beam with an energy spectrum different to that of the calibration source (here ^{241}Am-Be), the spectral dependence of R must be considered. The energy dependence of the detector response per personal dose equivalent $H_{\text{p}}(10)$ of the PADC detectors used in this study, has been investigated by PSI [52]. Mainly monoenergetic response measurements were used to determine the detector response as a continuous function of energy, except for the measurements with the highest energies, where neutron spectra from CERN and Los Alamos were used [52].

For this study, we are finally interested in neutron dose equivalent, thus the detector response curve determined by PSI relative to $H_{\text{p}}(10)$ was converted relative to $H(10)$.

To calculate the PADC response as a function of track density ρ_{track} per neutron dose equivalent, the above derived quality factors $q_{\text{p}}(E_{\text{n}})$ and $q_{\text{E}}(E_{\text{n}})$ are used in Equation (2.3) to scale the detector response determ-

ined at PSI:

$$R\left(E_{\mathrm{n}}\right)=\frac{1}{N}\cdot\frac{\rho_{\mathrm{track}}}{H\left(10\right)}=\frac{1}{N}\cdot\frac{\rho_{\mathrm{track}}}{H_{\mathrm{p}}\left(10\right)\cdot\frac{q_{\mathrm{E}}(E_{\mathrm{n}})}{q_{\mathrm{p}}(E_{\mathrm{n}})}}. \tag{2.3}$$

The PADC response function is normalised to the response of the neutron spectrum $\phi_{\mathrm{Surface}}^{\mathrm{Am-Be}}\left(E_{\mathrm{n}}\right)$ of the ^{241}Am-Be source with the normalisation factor given in Equation 2.4:

$$N=\int\frac{\rho_{\mathrm{track}}}{H_{\mathrm{p}}\left(10\right)\cdot\frac{q_{\mathrm{E}}(E_{\mathrm{n}})}{q_{\mathrm{p}}(E_{\mathrm{n}})}}\cdot\phi_{\mathrm{Surface}}^{\mathrm{Am-Be}}\left(E_{\mathrm{n}}\right)\,\mathrm{d}E_{\mathrm{n}}. \tag{2.4}$$

The normalised energy dependent PADC detector response function is depicted in Figure 2.1.

The response for a given neutron spectrum $\phi\left(E_{\mathrm{n}}\right)$ is then determined by:

$$R=\int R\left(E_{\mathrm{n}}\right)\cdot\phi\left(E_{\mathrm{n}}\right)\,\mathrm{d}E_{\mathrm{n}}=\frac{1}{N}\cdot\int\frac{\rho_{\mathrm{track}}}{H_{\mathrm{p}}\left(10\right)\cdot\frac{q_{\mathrm{E}}(E_{\mathrm{n}})}{q_{\mathrm{p}}(E_{\mathrm{n}})}}\cdot\phi\left(E_{\mathrm{n}}\right)\,\mathrm{d}E_{\mathrm{n}}. \tag{2.5}$$

The calibration factor for the spectral influence on the neutron dose equivalent for the spectrum of the investigated radiation quality at the surface of the phantom is then:

$$\begin{aligned}k_{2}^{\mathrm{Spectrum}}&=\frac{\int R\left(E_{\mathrm{n}}\right)\cdot\phi_{\mathrm{Surface}}^{\mathrm{Am-Be}}\left(E_{\mathrm{n}}\right)\,\mathrm{d}E_{\mathrm{n}}}{\int R\left(E_{\mathrm{n}}\right)\cdot\phi_{\mathrm{Surface}}^{\mathrm{Spectrum}}\left(E_{\mathrm{n}}\right)\,\mathrm{d}E_{\mathrm{n}}}\\&=\frac{1}{\int R\left(E_{\mathrm{n}}\right)\cdot\phi_{\mathrm{Surface}}^{\mathrm{Spectrum}}\left(E_{\mathrm{n}}\right)\,\mathrm{d}E_{\mathrm{n}}}.\end{aligned} \tag{2.6}$$

Radiotherapy treatments are performed using different radiation qualities. These different beams lead to different neutron spectra and therefore, as described above, to different readout signals of a measurement with PADC detectors. In this study, the resulting neutron spectra of treatments using photon, actively scanned proton, and double scattered proton beams were used to calculate the calibration factors. The Monte Carlo method with corresponding models of the beam delivery systems and geometric phantoms were used for the derivation of the neutron spectra in matter. The spectra were determined inside and outside of the treatment

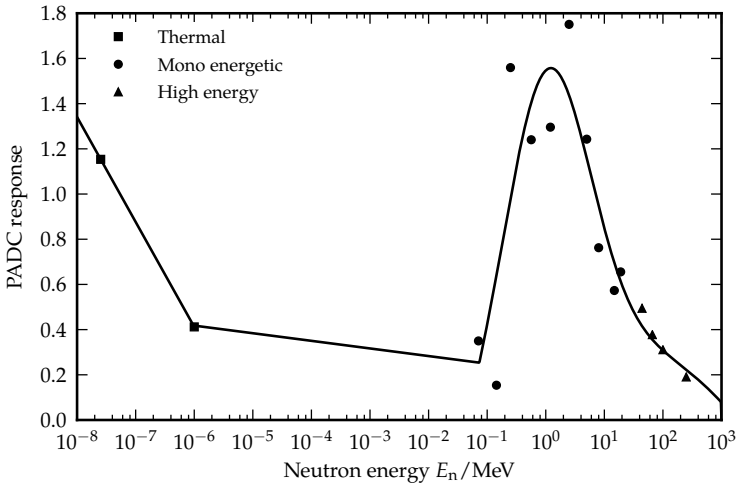

Figure 2.1: PADC detector response R as a function of neutron energy E_n. Adapted from measurements by PSI [52, 53, 64].

beam at different depths along the beam direction from 0 cm to 30 cm. Inside the treatment field, the spectra were determined on the central beam axis and outside on an axis laterally shifted by 25 cm from the central ray. All the spectra were normalised to the number of neutrons.

For the photon beam, a model of a Varian linear accelerator Clinac 2100 was used for the simulations [65]. The beam had a nominal energy of 18 MeV and a field size of 10 cm × 10 cm with the multileaf collimator retracted. A water tank of 100 cm × 100 cm × 30 cm was used as the phantom. The Monte Carlo simulation was performed using MCNPX. The resulting neutron spectra for two different depths are depicted in Figure 2.2.

A simplified geometrical model for the actively scanned proton beam was used for the simulation with the FLUKA Monte Carlo code [13–15]. As the number of neutrons produced in the gantry for actively scanned protons is small compared to the neutrons produced in the phantom, the influence of the beam delivery system was neglected. Therefore, an ideal proton beam with a field size of 10 cm × 10 cm was simulated impinging on a 90 cm × 30 cm × 30 cm phantom made of water. The beam energy was set to 160 MeV. In Figure 2.3, neutron spectra resulting from the simulation with the actively scanned proton beam are shown for two depths.

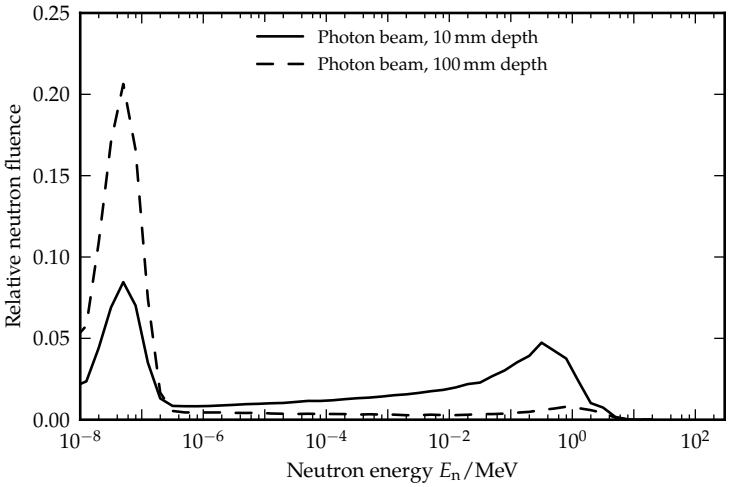

(a) In-field

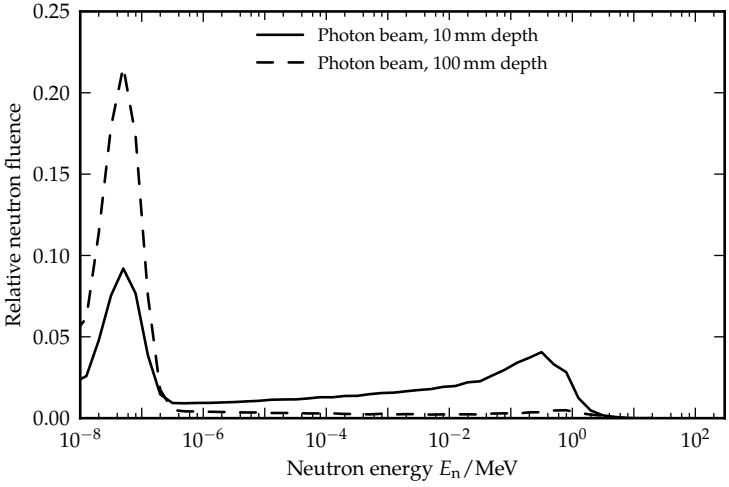

(b) Out-of-field

Figure 2.2: Neutron spectra for the photon beam in water at two different depths. (a) in-field, (b) out-of-field.

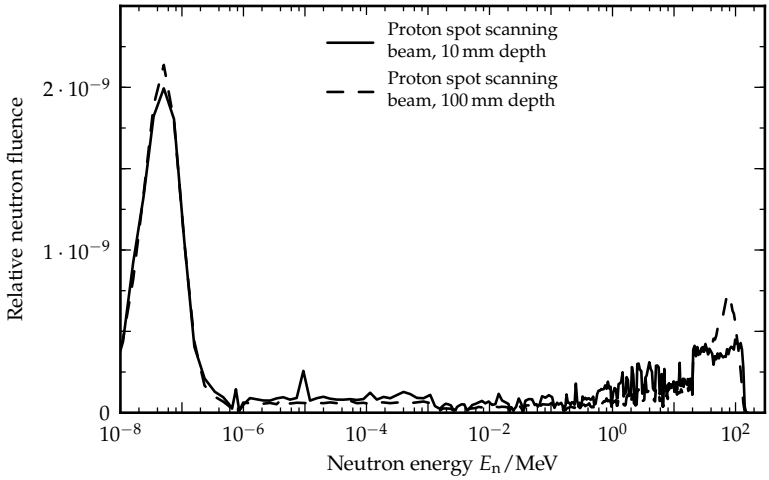

(a) In-field

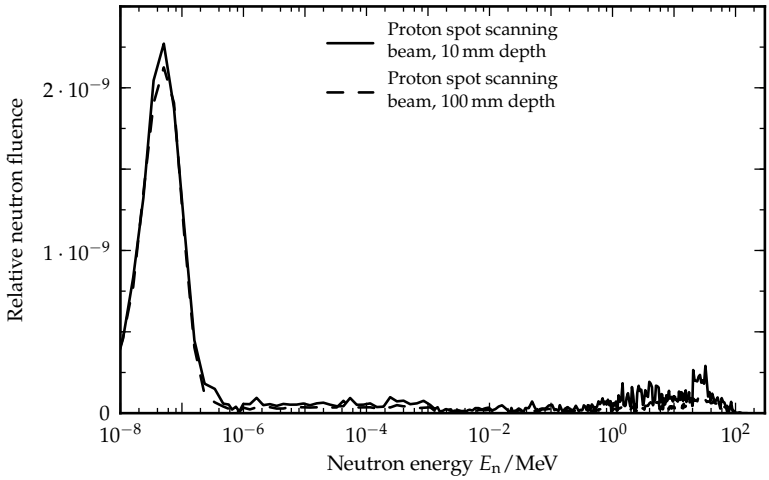

(b) Out-of-field

Figure 2.3: Neutron spectra for the active proton beam in water at two different depths. (a) in-field, (b) out-of-field.

The proton beam for passive beam delivery was simulated using a double scattering beam line with the GEANT4 Monte Carlo code [66]. The 90 % proton range was 25 cm and the used phantom material was Lucite, which corresponded to an energy of about 215 MeV. For this simulation, a treatment field from a prostate patient was applied instead of an open field. The neutron spectra for two different depths for the double scattering proton beam can be found in Figure 2.4.

2.2.3 Calibration of depth dependence of the spectra

Neutrons are continuously being moderated while passing through material. This means that the neutron spectrum is altered as a function of depth in the material and therefore the spectrum specific response of the detectors changes. The radiotherapy neutron spectra described in the last section, were simulated also at different depths in material. The PADC response for these neutron spectra was determined as a function of depth for all investigated radiation qualities. Usually radiotherapy patients are treated with an average number of irradiation fields larger than two. Thus, for a conservative estimate of the depth-calibration, the PADC response was calculated for two opposing treatment fields and then averaged. Consequently, the third calibration factor $\overline{k_3^{\text{depth}}}$ was defined in Equation (2.7) as the detector response for two opposing fields averaged over the depth d of $d_{\max} = 30\,\text{cm}$ in the phantom relative to the response at the surface:

$$\overline{k_3^{\text{depth}}} = \frac{\int R\left(E_\text{n}\right) \cdot \phi_{\text{Surface}}^{\text{Spectrum}}\left(E_\text{n}\right)\,\mathrm{d}E_\text{n}}{\frac{1}{d_{\max}} \int_0^{d_{\max}} \int R\left(E_\text{n}\right) \cdot \phi^{\text{Spectrum}}\left(d, E_\text{n}\right)\,\mathrm{d}E_\text{n}\,\mathrm{d}d}. \tag{2.7}$$

The uncertainty of $\overline{k_3^{\text{depth}}}$ is systematic and can be expressed by the minimal and maximal variation of the relative response with depth d.

In summary, several steps are needed to calculate neutron dose equivalent at a specific point given the readout of PADC detectors as measured tracks per square centimetre. Starting from the initial calibration in terms of neutron personal dose equivalent $H_\text{p}\left(10\right)$ per track, the calibration is expanded for the detector response to the neutron spectrum of the measurement beam and the depth dependence of the response in material, leading to an estimate of local neutron dose equivalent. The calculation of the neutron dose equivalent as a function of the track density ρ_{track} is finally done by using Equation (2.8):

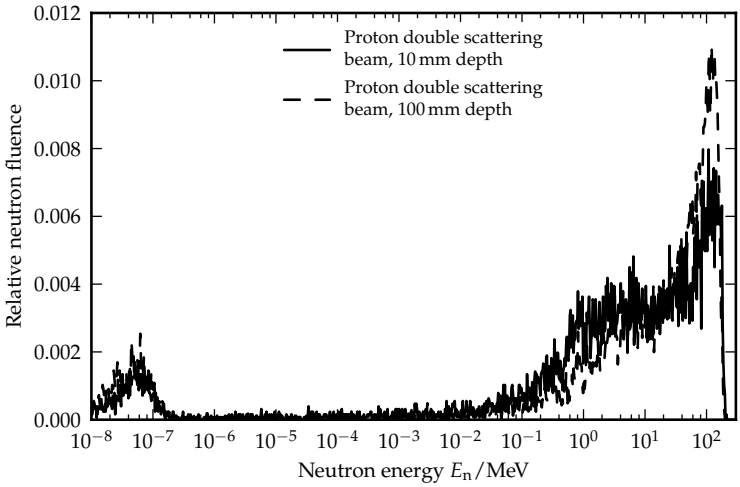

(a) In-field

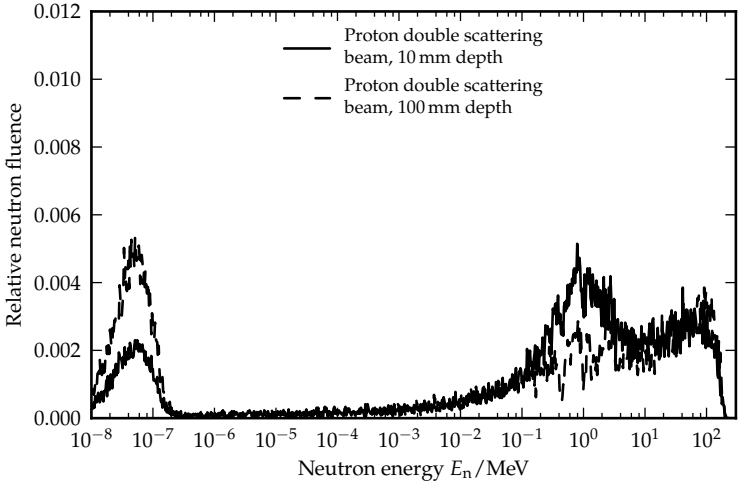

(b) Out-of-field

Figure 2.4: Neutron spectra for the double scattered proton beam in Lucite at two different depths. (a) in-field, (b) out-of-field.

$$H\,(10) = k_1^{\mathrm{Am-Be}} \cdot k_2^{\mathrm{Spectrum}} \cdot \overline{k_3^{\mathrm{depth}}} \cdot H_{\mathrm{p}}\,(10) =: k_{\mathrm{total}} \cdot H_{\mathrm{p}}\,(10)\,. \quad (2.8)$$

2.3 Results

For every batch of PADC detectors, the initial absolute calibration in terms of personal dose equivalent $H_{\mathrm{p}}\,(10)$ has to be determined at the ^{241}Am-Be source to account for the individual sensitivity of the specific batch and, for the detectors used in this work, varied between 9.90×10^{-3} mSv cm^2 ±21 % and 16.39×10^{-3} mSv cm^2 ±36 %. The uncertainty was determined by the standard deviation of the readouts of the subsets of calibration and background (not irradiated) detectors.

The conversion of the initial absolute calibration factor into neutron dose equivalent $H\,(10)$ for the ^{241}Am-Be spectrum was done by the use of the calibration factor $k_1^{\mathrm{Am-Be}}$. Its value was calculated to be 0.69.

To connect to the calibration factor for the conversion of tracks per area on the detector into neutron dose equivalent, the detector response was first calculated for the neutron spectra for every investigated radiation quality and the ^{241}Am-Be spectrum at the surface of the phantom. The second calibration factor k_2^{Spectrum} was the ratio of the detector response for the batch in the ^{241}Am-Be spectrum to the response of the specific neutron spectrum. The values were in the range of 1.09 to 1.46 for the different radiation qualities and are shown in Table 2.1.

The last step in the chain of calibration factors was the variation of the PADC response with depth in the phantom. This correlation is shown for a single beam impinging on the phantom for all the investigated radiation therapy beam qualities, inside and outside of the primary radiation field, in Figure 2.5. The values for the resulting depth calibration factor $\overline{k_3^{\mathrm{depth}}}$ (according to Equation (2.7)) were in the range of 0.79 to 1.33. In addition, the deviation to the maximum and minimum calibration factor over depth was determined. These values as well as the other calibration factors with the corresponding uncertainties (see Section 2.4) and the resulting total calibration factor k_{total} are listed in Table 2.1.

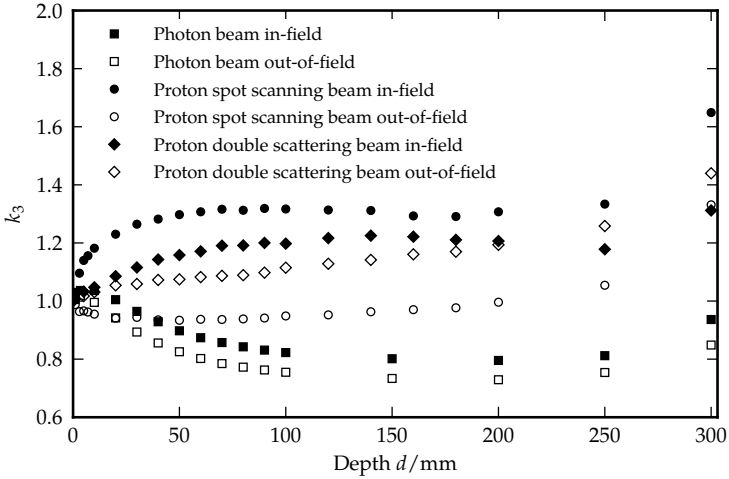

Figure 2.5: Variation of the PADC detector response with depth in the phantom using a single beam for all the investigated radiation qualities, in-field (closed symbols) and out-of-field (open symbols). The values are normalised to the response of the detectors at the surface of the phantom.

Radiation quality	$k_1^{\mathrm{Am-Be}}$	k_2^{Spectrum}	$\overline{k_3^{\mathrm{depth}}}$	k_{total}
Photons				
in-field	0.69 ±0.03	1.29 ±0.06	$0.85\ ^{+0.13}_{-0.05}$	$0.76\ ^{+0.14}_{-0.07}$
out-of-field	0.69 ±0.03	1.40 ±0.07	$0.79\ ^{+0.14}_{-0.06}$	$0.76\ ^{+0.15}_{-0.08}$
Active protons				
in-field	0.69 ±0.03	1.09 ±0.05	$1.33\ ^{+0.06}_{-0.03}$	$1.00\ ^{+0.09}_{-0.08}$
out-of-field	0.69 ±0.03	1.20 ±0.06	$1.01\ ^{+0.15}_{-0.04}$	$0.84\ ^{+0.16}_{-0.07}$
Passive protons				
in-field	0.69 ±0.03	1.28 ±0.06	$1.19\ ^{+0.03}_{-0.03}$	$1.05\ ^{+0.08}_{-0.08}$
out-of-field	0.69 ±0.03	1.13 ±0.06	$1.17\ ^{+0.05}_{-0.02}$	$0.91\ ^{+0.08}_{-0.07}$

Table 2.1: Resulting calibration factors $k_1^{\mathrm{Am-Be}}$, k_2^{Spectrum}, $\overline{k_3^{\mathrm{depth}}}$, and the total calibration factor k_{total} for the investigated radiation qualities together with the corresponding uncertainties.

2.4 Discussion

In the present study, a method of calibrating the readout of PADC track etch detectors in terms of neutron dose equivalent measured in man in radiation therapy has been presented. Unlike previous work with these, or similar detectors, the impact of radiation quality and variation of the neutron spectra with depth was considered.

In the determination of neutron dose equivalent using Equation (2.8), several uncertainties were involved. The energy dependence of the PADC detector response in terms of H_p (10) was investigated by PSI with uncertainties of the individual measurements in the order of 10 % to 20 % [53, 64]. In the region from thermal energies to about 0.07 MeV, measurements and a fit to neutron cross section data were used to estimate the detector response with corresponding higher uncertainties. The process of the readout of PADC detectors and the determination of the track density ρ_{track} had an uncertainty in the order of ±30 % [52].

The calculation of the first calibration factor k_1^{Am-Be} depended on the effective quality factor q_E, the quality factor q_p, and the ^{241}Am-Be neutron spectrum. The used formula for the quality factor q_E (Equation 2.1) is an approximation to the values for the male and the female phantom, as well as for anterior-posterior and isotropic irradiation [55]. The uncertainty was estimated by the differences of the values for the different cases to the averaged situation, which were about 10 % and changed k_1^{Am-Be} by about 1 %. The calculation of q_p had a maximal error of 4 %. A random variation of 50 % in the ^{241}Am-Be neutron spectrum lead to a change of k_1^{Am-Be} of less than 0.5 %. These uncertainties were smaller than the uncertainty of the readout of the detectors. The uncertainty of the second calibration factor $k_2^{Spectrum}$ was determined by the uncertainties in the detector response function and in the Monte Carlo calculated neutron spectra. The measurements to determine the response function of the detectors had an uncertainty of 10 % to 20 %, whereas the statistical uncertainty in the simulated spectra was in the order of a few percent. A random variation of 20 % in the response function $R(E_n)$ lead to a change of $k_2^{Spectrum}$ of about 5 %. The combination of these uncertainties lead to a general uncertainty of the calibration procedure of less than 40 %.

The calibration factor $\overline{k_3^{depth}}$ was related to a systematic uncertainty given as the variation around its mean value of the detector response with depth in matter. This systematic uncertainty had a maximum value for all the investigated radiation qualities of 18 % and was thus smaller than the

non-systematic uncertainties involved (40 %). Therefore it was appropriate to use a depth averaged calibration factor.

The neutron spectra for photon beams in this work were simulated for a Varian linear accelerator with a nominal energy of 18 MeV. It is therefore not a priori clear that the results can be used for other types and energies of linear accelerator. In a paper by Howell et al., neutron spectra of different manufacturers of electron linear accelerators for bremsstrahlung photon irradiations are compared [67]. They found that the neutron spectra are qualitatively comparable and only the absolute neutron fluences are considerably different. Therefore, the calibration presented here for the Varian photon beams could also be used for linear accelerators of other manufacturers. In the same study, photon beams of different nominal energies of a Varian linear accelerator were compared. Again the neutron spectra were found to be qualitatively comparable, which means that the calibration developed in this study is valid for different nominal photon beam energies as well. To investigate the dependence of the calibration factors on the primary proton energy, the neutron spectra were also simulated for the active proton beam of another energy in water. The differences of the calibration factors for this 200 MeV active proton beam, compared to the stated factors for 160 MeV, were less than 3 %, which was small compared to the combined uncertainty of the calibration procedure.

The spectrum specific calibration factors presented in this work, were calculated for neutron spectra in water (photons and active protons) or in Lucite (passive protons). For primary photons and active protons, the resulting neutron spectra were also simulated in Acrylic and Soft Tissue (ICRU Four-Component). The deviations to the stated calibration factors in water were smaller than 2 % for the photon beam and smaller than 4 % for the active proton beam (both inside and outside of the primary radiation field). Therefore the calibration factors obtained in this work are, within the overall error (40 %), independent of the materials used for the simulations.

For the application of the quality factors in this calibration, radiation equilibrium for the neutron radiation was assumed. For situations where equilibrium would not exist, for example at the edge of a phantom, uncertainties larger than those stated here apply.

2.5 Conclusion

PADC detectors are mainly used in personal neutron dosimetry based on a standard radionuclide neutron source calibration. The extended calibration procedure presented in this work showed that it is possible to use PADC detectors for measurements of local neutron dose equivalent inside phantoms. The field calibration included different radiation therapy beam qualities (photons, active and passive protons) and depths in material to account for spectral changes in the neutron fluence and the influence of the geometry.

Chapter 3

Measurements of Neutron Dose for Various Radiation Qualities, Treatment Machines, and Delivery Techniques in Radiation Therapy

Roger A. Hälg[1], Jürgen Besserer[1], Markus Boschung[2], Sabine Mayer[2], Antony J. Lomax[3] and Uwe Schneider[1,4]

[1] Institute for Radiotherapy, Radiotherapie Hirslanden AG, Aarau, Switzerland

[2] Division for Radiation Safety and Security, Paul Scherrer Institut, Villigen, Switzerland

[3] Center for Proton Therapy, Paul Scherrer Institut, Villigen, Switzerland

[4] Vetsuisse Faculty, University of Zurich, Zurich, Switzerland

Submitted to
Physics in Medicine and Biology
2012

3.1 Introduction

It is assumed that with the application of modern radiation treatment techniques, such as intensity-modulated radiotherapy, volumetric modulated arc therapy, and proton therapy, the cancer cure rates are increased and simultaneously unwanted side effects are reduced [34, 35]. There are obvious therapeutic advantages using these techniques, for example the improved conformity of the dose to the target volumes. But there are also concerns about a possible increase in radiation-induced malignancies with the application of these techniques [5, 6], in particular, for younger patients [7]. In the case of intensity modulation techniques using photons, there is an increase in the beam-on time to deliver the same dose to the target volume compared to conventional treatment techniques. In case of therapy modalities using high nominal photon energies (> 10 MV) or protons, neutrons are unintentionally produced. These secondary neutrons are produced in the beam delivery system and in the patient. The amount of neutron production in the patient is only of concern for the case of protons or other heavy particles, since most of the neutrons from high-energy photon beams are produced in the gantry head [68]. The absorbed dose from secondary neutrons is in small compared to the target dose, but due to their high biological effectiveness concerning cancer induction [26, 69], already small neutron doses can be important outside of the target volume in terms of long term health of radiotherapy patients. Therefore, the influence of the primary dose distribution, stray dose, and imaging dose as well as the secondary neutron radiation on secondary cancer incidence should be investigated further. A comprehensive list of studies evaluating neutron dose contributions for treatments using high energy photons, protons, and other techniques or radiation qualities can be found in a review article by Xu et al. [19]. In a more recent article, the current status of neutron dose studies for photon radiotherapy is reviewed by Takam et al. [22]. According to them, most of the reports in the literature used neutron dose measurements free in air, on the surface of phantoms or inside geometrical phantoms. Organ neutron doses were determined using combinations of measurements and calculations.

The aim of this study was to measure neutron dose inside an anthropomorphic phantom, associated with the irradiation of a radiotherapy patient during a typical treatment. The measured neutron (organ) doses were compared with respect to treatment technique, therapy machines, and radiation quality.

3.2 Materials and Methods

The clinical setup of the study was the curative irradiation of a rhabdomyosarcoma of the prostate for an adolescent patient, who was represented by an Alderson-Rando phantom. The planning CT of the phantom and the contouring of the target structures as well as of the radiation sensitive organs (done by a physician) were performed at one institution. The dose prescription for the irradiation was 26×2.0 Gy for the well established 3D-conformal treatment and 23×2.0 Gy for the other treatment modalities. For the proton treatments, the dose prescription is given in cobalt Gray equivalent and is hence already weighted with a relative biological effectiveness factor of 1.1, which is the standard procedure for proton irradiations world-wide [70]. The fractionation schemes have been matched to represent the same biological target dose using the linear-quadratic model and an α/β ratio of 2.8 [71]. This information was sent to all the institutions participating in this study along with a planning guideline containing the CT calibration curves, dose prescription, planning structures, dose constraints, and the location of the isocenter. All measurements and detector readouts were performed by the same persons. This procedure ensured the comparability of the treatment plans as well as of the irradiations and measurements at the different sites.

The series of measurements included photon and proton irradiations. The photon beams were delivered by treatment machines of the manufacturers Varian, Elekta, and Siemens. On the Varian linear accelerator the irradiation techniques 3D-conformal (3DCRT), volumetric modulated arc therapy (VMAT), and intensity modulation (IMRT) were measured. IMRT treatments were investigated for all three manufacturers of linear accelerators. The proton irradiations were performed using spot scanning and double scattering. Measurements were performed at Radiotherapie Hirslanden AG, Aarau Switzerland (Varian Clinac 21 iX), Canton Hospital St. Gallen, St. Gallen Switzerland (Elekta Synergy), Canton Hospital Aarau, Aarau Switzerland (Siemens Oncor Avant-Garde), Center for Proton Therapy, Paul Scherrer Institut (PSI), Villigen Switzerland (proton spot scanning, Gantry 1), and Francis H. Burr Proton Therapy Center, Massachusetts General Hospital, Boston USA (proton double scattering, Gantry 2). The different photon beams had nominal energies according to BJR-11 [72] of 15 MV (Varian), 15 MV (Elekta), and 18 MV (Siemens), which corresponded to measured tissue-phantom ratios $TPR_{20,10}$ of 0.760, 0.757, and 0.773, respectively. The energies of the spot scanned proton fields were 160 MeV and 177 MeV. For the double scattering beamline, en-

ergies in the range of 135 MeV to 140 MeV and 175 MeV to 180 MeV were used. A comparison of the used beam energies and monitor units (MU) per plan for the photon treatments is listed in Table 3.1.

	Elekta IMRT	Siemens IMRT	Varian 3DCRT	Varian IMRT	Varian VMAT
Nominal energy	15 MV	18 MV	15 MV	15 MV	15 MV
$TPR_{20,10}$	0.757	0.773	0.760	0.760	0.760
Monitor units	527 MU	436 MU	234 MU	498 MU	485 MU
Number of fields	5 fields	9 fields	4 fields	5 fields	1 arc
MLC	SMLC	SMLC	SMLC	DMLC	DMLC

Table 3.1: Comparison of the different treatment modalities. Listed are the beam energies used (nominal and $TPR_{20,10}$), monitor units (MU) per plan, number of fields, and the type of MLC, dynamic MLC (DMLC) or static MLC (SMLC).

Figure 3.1 shows the calculated primary dose distributions on a transversal CT slice for a 5 field IMRT plan and for a single arc VMAT plan for the Varian Clinac 21 iX linear accelerator.

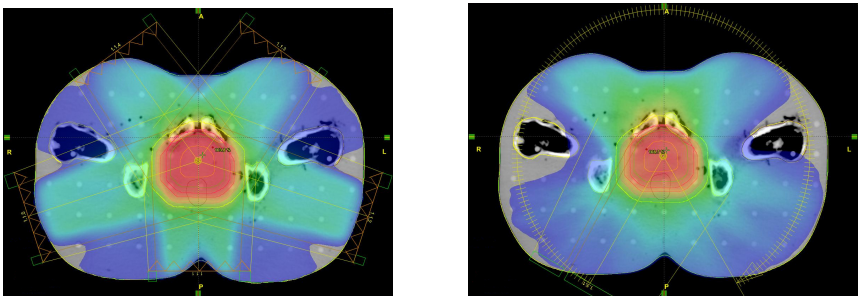

(a) Calculated dose distribution IMRT (b) Calculated dose distribution VMAT

Figure 3.1: Field setup and primary dose distribution on a transversal CT slice calculated in (a) for a 5 field IMRT plan and in (b) for a single arc VMAT plan for the Varian Clinac 21 iX.

In order to evaluate the neutron dose for a radiation oncology patient, an anthropomorphic Alderson-Rando phantom (RSD Long Beach, CA, USA) was used in this study to account for the patient anatomy. It is not a priori clear that neutron dose measurements inside a phantom represent the actual neutron dose in the patient, since neutron production cross

sections are dependent on the chemical composition of the material. However, Monte Carlo simulations by Hälg et al. [73] showed that the Alderson soft tissue material is suitable for neutron dosimetry within the achievable measurement accuracy. The dose measurements were performed using poly(allyl diglycol carbonate) (PADC) track etch detectors provided by the Radiation Metrology Section of the Division for Radiation Safety and Security at Paul Scherrer Institut in Villigen Switzerland [52, 74]. This detector material has virtually no photon sensitivity [75] and is thus suitable to measure neutron dose in a mixed field of photons and neutrons. Photon sensitivity measurements of the dosimeters used showed a photon sensitivity of about 0.05 % [76]. The dosimeters were placed inside and on the surface of the phantom, facilitating the determination of a three dimensional dose distribution and the evaluation of the dose to radiation sensitive organs according to the ICRP recommendations [26]. For the detector positions inside of the phantom, dedicated cavities were milled. An example of a PADC detector with two radiators inside the Alderson-Rando phantom is shown in Figure 3.2. A subset of the detectors was positioned on the medial patient axis. This allowed the determination of a one dimensional representation of the neutron dose equivalent from the target volume in the prostate to the head. For the neutron dose measurements at the proton facilities, the detector positions inside the treated volume were shifted dorsal outside of the target volume in order to minimise the influence of primary protons on the measured neutron dose. A total of 23 detector positions and two additional reference detectors were used per measurement. In Figure 3.3, the positions of the PADC detectors inside the phantom are shown in a frontal scout view of the Alderson-Rando phantom together with the isocenter in the prostate and the medial patient axis. All measurements were performed twice and the average readout of the two detectors per position was used to report the results. To determine organ neutron dose equivalent of the selected organs, the average of all the detectors assigned to the specific organ structure was calculated. Since the sensitivity of the PADC track etch detectors is best in a limited dose range, the detectors at the different positions were irradiated with different multiples of the treatment plans, according to the position of the detector relative to the primary radiation field, treatment modality, and radiation quality.

The readout of the PADC detectors was initially calibrated in personal dose equivalent $H_{\mathrm{p}}(10)$ using the radiation field of the ^{241}Am-Be neutron source at PSI and an ISO water slab phantom [56, 57, 59–61]. This was done for every batch of detectors used for the series of measurements, allowing

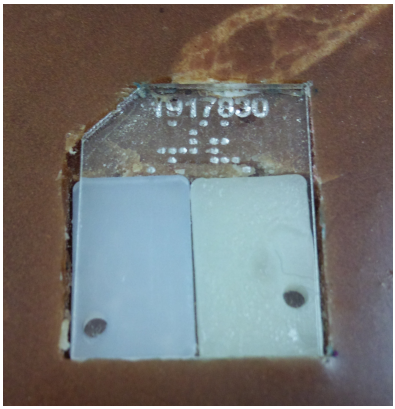

Figure 3.2: A dedicated cavity inside the Alderson-Rando phantom with a PADC detector and two radiators.

the individual sensitivity of the batches to be account for. In addition, subsets of background and transport detectors were used for each batch to subtract possible unwanted signal from the readout. A further calibration procedure was applied to account for the changes of the irradiation setup for the measurements compared to the calibration setup. This included calibration factors for the phantom geometry, the neutron spectrum of the used radiation treatment beam quality and the changes of the neutron fluence inside the phantom. A detailed description of this procedure can be found in a work by Hälg et al. [77] (chapter 2 of this thesis).

The neutron doses were determined in terms of neutron dose equivalent H per treatment Gray and for the whole course of treatment. In addition, the effective neutron dose was calculated using the sum of the organ specific weighted neutron dose equivalent according to the definition of effective dose in the ICRP recommendations [26].

3.3 Results

The neutron dose was measured on the medial patient axis with 13 detectors from the target in the prostate to the head. In Figure 3.4 the measured neutron dose equivalent along this axis is shown for the different treatment techniques on the Varian linear accelerator. The dose was scaled to neutron dose equivalent per total treatment dose of the whole course of

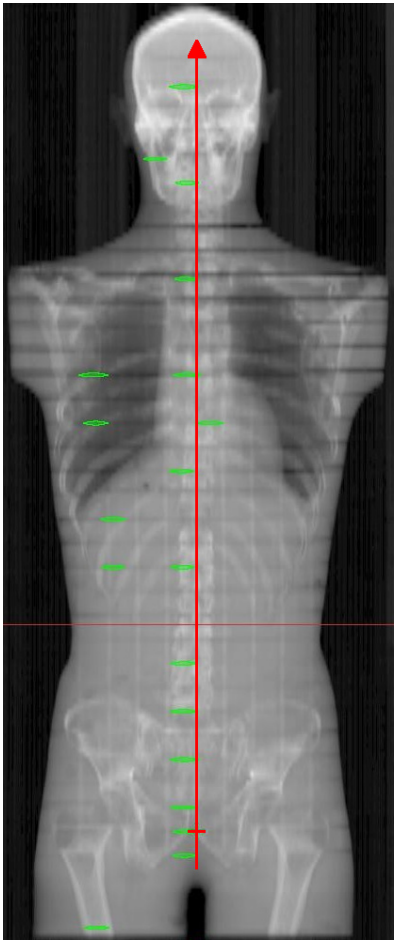

Figure 3.3: Frontal scout view of the Alderson-Rando phantom with the PADC detector positions inside the phantom and the medial patient axis with the isocenter in the prostate.

treatment to account for the different fractionation schemes of the different treatment techniques (26 × 2.0 Gy (3DCRT) or 23 × 2.0 Gy). A comparison of the neutron dose equivalent for IMRT treatments on the different linear accelerators along the medial patient axis per treatment Gray can be found in Figure 3.5. The same dose distribution for the proton treatments is depicted in Figure 3.6 and the dose from the IMRT treatment on the Varian linear accelerator is added for comparison. The distance 0 cm on the x-axis corresponds to the isocenter in the prostate and the vertical lines are the borders of the target volume along the selected direction ($x = -4.5$ cm and $x = 4.0$ cm).

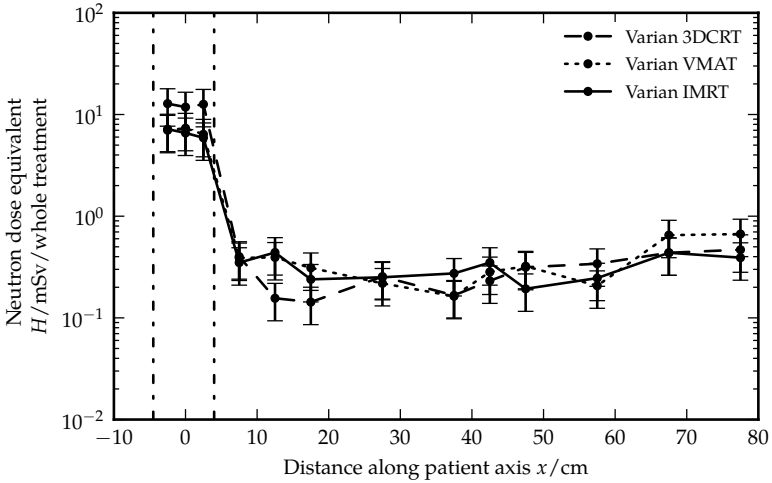

Figure 3.4: Neutron dose equivalent along the medial patient axis. The isocenter corresponds to $x = 0$ cm and the vertical lines represent the border of the target volume along this axis. Total course of treatment (26 × 2.0 Gy (3DCRT) or 23 × 2.0 Gy) for different techniques on the Varian linear accelerator.

The remaining PADC detectors were positioned inside and on the surface of the phantom to measure organ specific neutron doses. The resulting average neutron dose equivalent per treatment Gray for the selected organs is listed in Table 3.2.

The organ doses listed in Table 3.2 were used to calculate effective neutron doses. For the complete course of treatment they were calculated to be 2.9 mSv, 2.6 mSv, 2.3 mSv, 0.54 mSv, 1.9 mSv, 18 mSv, and 24 mSv for Varian 3DCRT, Varian VMAT, Varian IMRT, Elekta IMRT, Siemens IMRT,

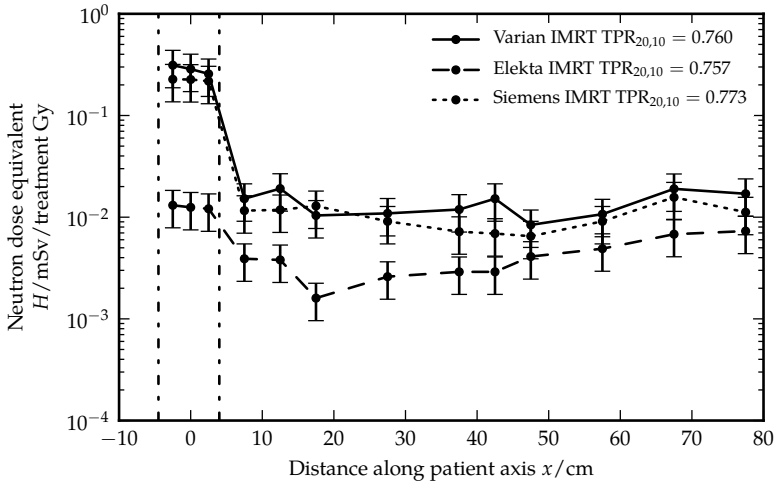

Figure 3.5: Neutron dose equivalent along the medial patient axis. The isocenter corresponds to $x = 0$ cm and the vertical lines represent the border of the target volume along this axis. IMRT treatments on different linear accelerators.

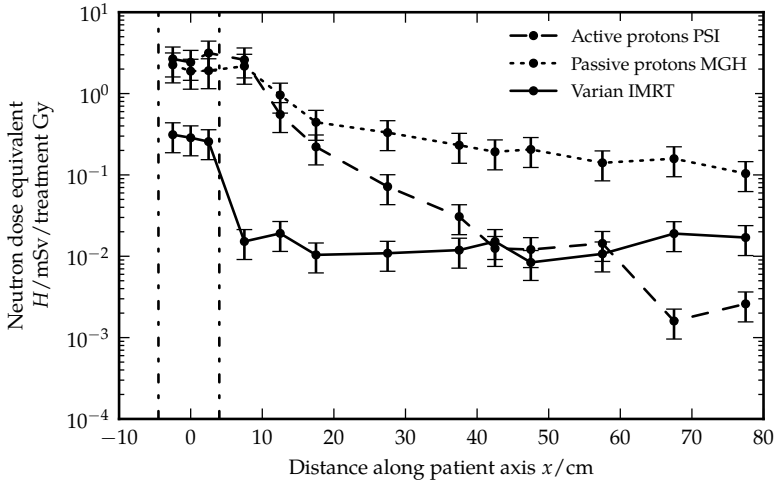

Figure 3.6: Neutron dose equivalent along the medial patient axis. The isocenter corresponds to $x = 0$ cm and the vertical lines represent the border of the target volume along this axis. Active and passive proton therapy compared to IMRT on the Varian linear accelerator.

ICRP organ	Elekta IMRT	Siemens IMRT	Varian 3DCRT	Varian IMRT	Varian VMAT	Active protons	Passive protons
			μSv / treatment Gy				
Bone marrow	6	15	17	21	21	183	423
Colon	3	11	9	14	14	861	851
Lung	16	34	41	43	56	17	346
Stomach	3	7	6	12	7	24	232
Breast	39	86	71	83	106	17	328
Remainder	6	64	127	83	87	701	785
Bladder	12	218	485	257	278	3152	1913
Oesophagus	4	8	11	10	10	17	199
Liver	5	17	13	17	25	61	485
Thyroid	5	9	13	11	9	14	141
Bone surface	6	15	17	21	21	183	423
Brain	7	11	18	17	29	3	104
Salivary glands	18	32	45	48	77	5	210
Skin	54	161	159	148	166	34	647

Table 3.2: Average organ neutron dose equivalents H in μSv per treatment Gy for various treatment modalities.

spot scanning protons, and passively scattered protons, respectively. A detailed listing of all the effective neutron doses, calculated for different primary doses, can be found in Table 3.3.

3.4 Discussion

The observed differences in neutron dose equivalent between the different treatment techniques on the Varian linear accelerator were within the measurement uncertainty for most of the measurement points. The 3D-conformal treatment tends to have a lower neutron dose outside of the primary field close to the field border but higher dose within the treatment field. This finding is consistent with another study by Hälg et al. where neutron dose from open and intensity-modulated fields in a geometrical phantom was compared [78] (chapter 4 of this thesis).

When comparing the IMRT treatment technique on different linear accelerators, it was found that Elekta treatment machines produce considerably lower neutron dose than Varian and Siemens machines. This was observed for all measurement positions. The neutron dose from the Siemens machine is slightly lower than that from the Varian machine in

Treatment	Effective neutron dose per treatment Gy	Effective neutron dose per whole treatment	Effective neutron dose outside target per whole treatment
Elekta IMRT	0.011	0.54	0.5
Siemens IMRT	0.037	1.9	1.2
Varian 3DCRT	0.056	2.9	1.2
Varian VMAT	0.051	2.6	1.6
Varian IMRT	0.045	2.3	1.3
Active protons	0.35	18	8.8
Passive protons	0.48	24	19

Table 3.3: Effective neutron doses of the different treatment modalities in mSv per treatment Gy, per whole course of treatment (52.0 Gy (3DCRT) or 50.6 Gy), and per whole course of treatment outside of the target volume.

general. No restriction was given in the planning guideline for the number of monitor units for the IMRT plans. Instead, dose constraints for the planning volumes were given and the institutions were asked to perform the treatment planning as they would do it for a regular patient. Therefore there were differences in the number of monitor units used, as shown in Table 3.1.

For proton treatments, neutron dose is higher in general compared to the investigated photon treatments and apparently higher for scattered compared to spot scanned protons. Inside and close to the primary radiation field, the measured dose was higher for active protons than for passive protons. For distances far away from the treatment field, the neutron dose from spot scanning protons is in the same order or even lower than that from the Varian IMRT irradiation.

In general, one can say that the measured neutron dose for the investigated treatments was at least one order of magnitude lower than the scatter dose from a corresponding treatment using photons with 6 MV [79].

The values of the effective neutron doses are dominated by the contribution of the neutron dose measured in the bladder. This dose value is the highest because of the partial overlap of the target volume with the bladder. The stated neutron dose has to be examined in relation to the much larger dose of the primary treatment field for organs in or close to the target volume. The dose deposition in the tumour volume can be viewed as "non-avoidable", therefore the effective neutron doses including only the organs outside of the treatment field were added in Table 3.3.

The initial absolute calibration factor for the PADC detectors in terms

of personal dose equivalent $H_p(10)$ for the dosimeters used in this work was determined at PSI and varied between 10.21×10^{-3} mSv cm^2 ±13 % and 12.55×10^{-3} mSv cm^2 ±7 %. The given uncertainty was determined by one standard deviation of the readouts of the subset of calibration and background detectors. For the whole calibration procedure including the calibration factors for the spectral changes in the neutron fluence, the uncertainty was determined to be 40 % [77] (see chapter 2). This uncertainty already includes the before mentioned uncertainty of the readout of the calibration detectors.

3.5 Conclusion

Measurements of neutron dose equivalent were performed to assess the neutron dose contribution from typical treatments in radiation therapy for different treatment techniques, therapy machines, and radiation quality. Only small differences in neutron dose equivalent were found when comparing 3D-conformal, intensity-modulated radiation therapy, and volumetric modulated arc therapy treatment techniques on the Varian linear accelerator. On the other hand, substantial differences in neutron dose were measured for different linear accelerator models using IMRT. Neutron dose from the investigated Elekta linear accelerator was much lower than that of the linear accelerators from Siemens and Varian. For proton therapy, the neutron dose was higher than for photon irradiation therapy in general and in particular higher for the double scattering proton beam compared to the spot scanning beam investigated in this study.

The overall dose additional to the therapeutic dose induced by secondary neutrons was of the same order of magnitude as the dose from a wide range of contemporary imaging modalities used for image-guided radiotherapy [80] (see chapter 6) and an order of magnitude lower than the stray dose of a corresponding treatment with a 6 MV photon beam [81] (see chapter 5). Considering this, the stray dose contributions from passive proton therapy (highest neutron stray dose in this study) were of the same order of magnitude as from photon therapy when the neutron and the photon stray dose was combined. On the other hand, active proton therapy corresponded to the lowest total out-of-field dose, when considering the stray dose from neutrons and photons. This suggests that secondary neutron dose may have been overestimated in the past. Therefore the usability of treatment techniques which produce secondary neutrons, in particular high energy photon IMRT, should be considered in the same

way as the usage of additional imaging modalities for the benefit of the patient.

Acknowledgements

This work was funded in part by the KIRO grant from the Federal Office of Public Health (FOPH), Switzerland.

The authors would like to express their gratitude to M. Gantert, S. Khan, and G. Lutters from Canton Hospital Aarau, to S. Peters and H. Schiefer from Canton Hospital St. Gallen, to P. Pemler from City Hospital Triemli, to M. Engelsman and J. Flanz from MGH Boston, and to A. Lehde and C. Algranati from Paul Scherrer Institut, for helping and giving the opportunity to perform the measurements at their institutions.

Chapter 4

Monitor Units Are Not Predictive of Neutron Dose for High-Energy IMRT

Roger A. Hälg[1], Jürgen Besserer[1], Markus Boschung[2], Sabine Mayer[2], and Uwe Schneider[1,3]

[1] Institute for Radiotherapy, Radiotherapie Hirslanden AG, Aarau, Switzerland

[2] Division for Radiation Safety and Security, Paul Scherrer Institut, Villigen, Switzerland

[3] Vetsuisse Faculty, University of Zurich, Zurich, Switzerland

Submitted to
Radiation Oncology
2012

4.1 Introduction

With the application of new radiation treatment modalities such as intensity-modulated radiotherapy (IMRT) or intensity-modulated arc-therapy, increased tumour control probabilities are anticipated. However, with the application of these treatment techniques also a larger number of secondary cancers is expected. Some scientists believe that we will see an increase in second malignancies due to the substantial increase in beam-on time of IMRT techniques to deliver the same target dose compared to conventional treatment techniques [5, 6]. A consequence of the extended beam-on time is an increased dose of stray radiation, including neutrons, which affects the whole patient. The neutrons could lead to a considerable contribution to the integral dose, in particular, since neutrons have a large quality factor and thus even a small physical dose can result in substantial biological effects.

Most measurements and estimates of neutron dose equivalent from radiotherapy treatments found in the literature are usually given in operational dose quantities, which represent effective dose and thus a person risk. A compilation of current literature is listed in the review article by Xu et al. [19]. It should be noted that the neutron dose is only one contribution to integral dose and person risk. Others are for example dose contributions from scattered photons, leakage radiation, products from inelastic nuclear reactions, and imaging modalities.

In this report neutron detectors were used, which were calibrated to measure local neutron dose equivalent, at different depths in a solid water phantom inside and outside of the primary radiation field for an open and intensity-modulated radiation field.

4.2 Materials and Methods

The neutron dose measurements were performed with a detector system consisting of a PADC (poly(allyl diglycol carbonate)) track etch detector (Thermo Fisher Scientific Inc., Waltham MA, USA) with 2 mm thick radiators (polyethylene and polyethylene with lithium) on both sides. The detectors were provided and read-out by the Division for Radiation Safety and Security of the Paul Scherrer Institut (PSI) [52, 53].

The detectors were immersed into a 30 cm × 30 cm × 30 cm large RW3 solid water phantom (PTW, Freiburg, Germany). A specifically manufactured holder (acrylic glass) was used to irradiate three detectors simultan-

eously in order to improve statistics. The experimental setup is depicted in Figure 1. Four measurement positions were chosen: in the radiation field at 0.2 cm depth (D1) as well as in 15 cm depth (D2) and in gun direction outside of the treatment field at 0.2 cm (D3) and 15 cm (D4) depth, respectively. The in-field detectors (D1, D2) were placed on the central ray of the radiation field, the out-of-field detectors (D3, D4) 20 cm away from the central ray.

A linear accelerator (Varian Medical System, Palo Alto, CA, USA) was used to produce a photon radiation beam with a nominal energy of 15 MV, having a tissue phantom ratio $TPR_{20,10}$ at 20 cm/10 cm depth of 0.760. Two irradiation techniques have been used. The first field was an open radiation field delivering 75 monitor units (MU) and a total dose of 0.592 Gy in 15 cm depth. The field size of 10 cm × 10 cm was defined by the jaws and the multileaf collimator (MLC) was retracted. The second radiation field was intensity-modulated, with a 2.32 cm sweeping MLC gap of 10 cm lateral dimension. With the IMRT field, the same dose was delivered as with the open field, but with 225 monitor units. The jaws were positioned to form a 10 cm × 10 cm field. The MU-ratio between the intensity-modulated and the open field was three. Since the sensitivity of the PADC detectors is optimal in a limited dose range, the detectors at the different positions were irradiated with different doses. For the measurement position D1, the radiation field was applied two times, for the positions D2 and D3 six times and for D4 120 times.

The detector output given in tracks per area was first calibrated into personal dose equivalent $H_p(10)$. For this purpose, a subset of the PADC detectors from the measurement batch was mounted on an ISO water slab phantom and irradiated with neutrons from an ^{241}Am-Be neutron source. The dose at the detector position was determined with a Berthold LB6411 neutron dose rate meter calibrated at the Physikalisch-Technische Bundesanstalt in Braunschweig, Germany [56], which is used as a secondary standard at PSI. The resulting calibration factor for the used batch of PADC detectors was 16.39×10^{-3} mSv cm^2 ±36 % (one standard deviation).

The radiation quality used in the experiment was a photon beam with a nominal energy of 15 MV, which produces neutrons with a different energy distribution than the ^{241}Am-Be calibration source. To account for this difference, Monte Carlo simulated neutron spectra in water of a therapeutic photon beam from a Varian linear accelerator were taken from Kry et al. [65, 77]. The detector response normalised to the ^{241}Am-Be neutron spectrum from a PSI technical report [64] was convolved with the

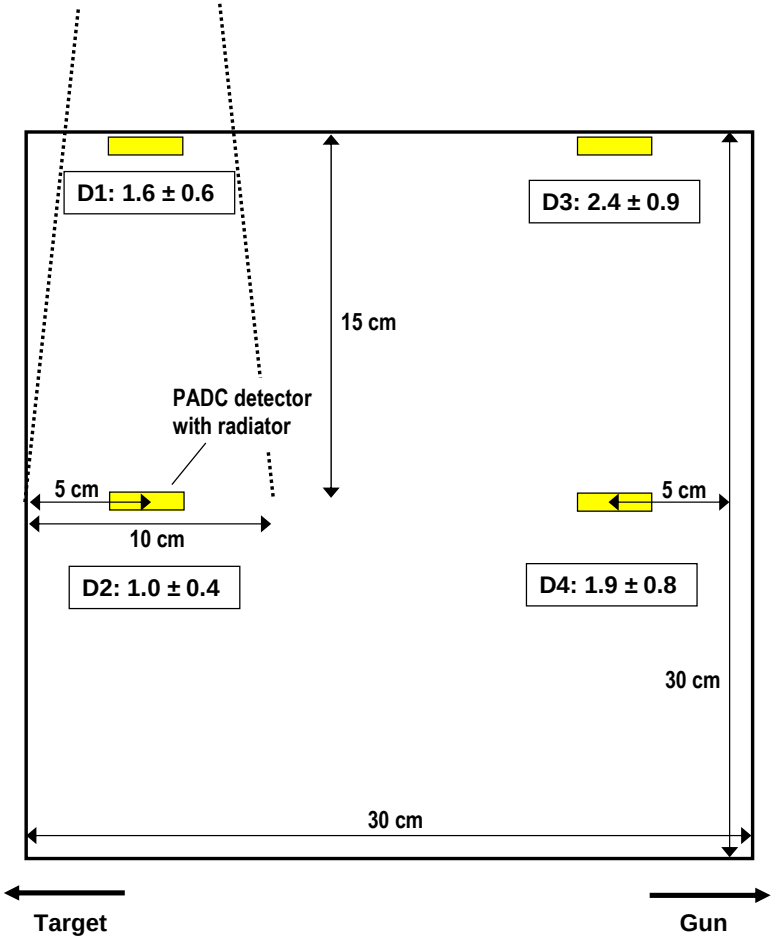

Figure 4.1: Experimental setup. A 30 centim × 30 centim × 30 centim RW3 solid water cube was irradiated with a 10 cm × 10 cm field with a nominal energy of 15 MV at a source surface distance of 85 cm. The radiation beam was placed such that the central ray was 5 cm from the phantom border (isocenter was located at 15 cm depth). The PADC detectors were placed horizontally 5 cm from the edge of the phantom. The numbers in the boxes indicate the ratio of neutron dose equivalent from the IMRT field relative to the open field for the same absorbed dose at position D2.

normalised neutron spectra simulated inside and outside of the radiation field, resulting in calibration coefficients for the neutron spectra at the four detector positions, which are listed in Table 4.1. The absolute calibration factor from tracks per square centimetre into neutron personal dose equivalent $H_p(10)$ in mSv cm^2 was determined in the neutron field of the ^{241}Am-Be source. The calibration factors from neutron personal dose equivalent into neutron dose equivalent, considering the spectral changes with depth, are given for the two depths inside and outside of the treatment field. This field calibration procedure is described by Hälg et al. [77] (chapter 2 of this thesis).

Depth in cm	Neutron personal dose equivalent $\frac{H_p(10)(\mathrm{Am-Be})}{\mathrm{tracks/cm^2}}$ in mSv cm^2	Neutron dose equivalent $\frac{H(15\,\mathrm{MV photons})}{H_p(10)(\mathrm{Am-Be})}$	
		in-field	out-of-field
0.2	$16.39 \cdot 10^{-3}$	0.91	0.96
15.0		0.71	0.71

Table 4.1: Calibration factors for converting tracks per square centimetre into neutron dose equivalent H in mSv for the different positions in the phantom. The second column represents the initial absolute calibration from tracks per square centimetre into neutron personal dose equivalent $H_p(10)$ in mSv cm^2, performed in the ^{241}Am-Be neutron field. The third column contains the calibration factors from neutron personal dose equivalent into neutron dose equivalent considering the spectral changes with depth.

4.3 Results

The measurement series were performed once for the open field and twice for the IMRT field, leading to three and six measurement values per location, respectively. The average value of the measurements at each location was used to report the results.

The measured neutron dose equivalents at the four locations for the two techniques are listed in Table 4.2. The ratio of the neutron dose equivalent from the IMRT treatment to the dose resulting from the open field irradiation is shown in the boxes of Figure 1 at the four positions. In the treatment field itself the ratio drops from 1.6 at the surface to 1.0 at 15 cm

depth. Outside the treatment field the ratio is 2.4 at the surface and 1.9 at 15 cm depth.

Depth in cm	Neutron dose equivalent in mSv Gy^{-1} for an open field		Neutron dose equivalent in mSv Gy^{-1} for an IMRT field	
	in-field	out-of-field	in-field	out-of-field
0.2	2.8	1.0	4.5	2.4
15.0	0.20	0.015	0.20	0.029

Table 4.2: Neutron dose equivalent in mSv per treatment Gy measured at different depths for an open field and an intensity-modulated field. The dose was prescribed to measurement point D2.

4.4 Discussion

The uncertainty of the calibration and readout of the PADC detectors was estimated by the standard deviation of the readout of two subsets of the detector batch which were used as background detectors or have been irradiated with neutrons from the ^{241}Am-Be source for the absolute calibration. It was calculated to be $\sigma = 36\,\%$. This was verified by the statistical deviations of the minimum or maximum readout to the mean value of the three repeated measurements at each measurement position, which were in the range of $-17\,\%$ to $30\,\%$ with an average of less than $10\,\%$. The error of the mean was calculated using the Student's t-distribution $\Delta D = t \cdot \sigma/\sqrt{n} = 27\,\%$ with $n = 3$ and a corresponding $t = 1.32$. The total uncertainty was then calculated by error propagation for the ratios of the open and the intensity-modulated field doses. The overall uncertainty of the dose ratios was 39 %. In addition to the detector batch variation of 36 % an uncertainty of 17 % comes from three sources. One source of around 5 % comes from the spectral difference of the calibration conditions (neutrons from an Am-Be source) and the open photon radiotherapy beam. Another source of around 15 % comes from the spectral change with depth in the phantom. Both of these uncertainties apply more or less in a similar way to the open and the MLC field and were therefore not considered for the error estimate of the dose ratios. The residual uncertainty of maximal 7 % comes from the differences in fluence between the open and the MLC field which was not accounted for, as it is much smaller than the 36 % batch uncertainty.

An IMRT treatment delivers more monitor units than a conventional irradiation due to the realisation of the intensity modulation. As a consequence, beam-on time is larger for the same delivered dose. Commonly it is assumed that neutron dose equivalent scales with the number of applied monitor units for a radiotherapy treatment irrespectively of the used treatment technique [5, 6]. The measurements presented in this report indicate that this may only be true for superficial tissues outside of the treatment field. Deeper lying tissues outside the treatment volume receive around 35 % less neutron dose equivalent than expected (three times expected and around two times observed). In the treated volume the dose reduction is even more pronounced with a 45 % reduction at the surface and a 65 % reduction in larger depth. However, it should be noted here that the irradiated volume is in general much smaller than the body volume which receives only stray dose. Therefore, if it is assumed that cancer induction is a function of dose and irradiated volume, the neutron dose reduction in the irradiated volume might not have a large impact. In addition the neutron dose equivalent must be viewed always in relation to the primary dose distribution, which is several orders of magnitude larger in the treated volume.

A possible explanation for the measured difference in scaling of the neutron dose with applied monitor units for open and intensity-modulated fields could be the interplay between neutron production and neutron shielding of the multileaf collimator when used in IMRT. Kry et al. [82] found in Monte Carlo simulations of neutron production in a Varian linear accelerator head that the MLC can act as a neutron absorber where the primary photon beam is shielded by the jaws. Zanini et al. [68] did a Monte Carlo study on the photoneutron fields of a Varian linear accelerator operating at a nominal energy of 18 MV. They determined neutron spectra at different locations (inside and outside of the primary field) for different collimation settings. The spectra simulated in that study at 3 cm (as in-field) and 15 cm (as out-of-field) laterally from the isocenter were used to estimate the expected readout of the PADC detectors used in this work. For this purpose the spectra were convolved with the energy dependent detector response function of the PADC detectors determined by PSI [52, 53, 64]. The absolute neutron fluence per square centimetre per Gray obtained by Zanini et al. for the static MLC field was multiplied by a factor of three to account for the elongated beam-on time for intensity modulation. The calculated PADC response includes not only the spectral change, but also effects like for example the absorption of neutrons by the MLC. The simulated detector response yielded a neutron dose ratio of 2.4

for the in-field spectrum and 2.0 for the out-of-field spectrum at the surface. These values are in agreement with the measurements of this study. In the work by Zanini et al. it was also shown that for equal field sizes the amount of neutron production in the MLC is smaller than in the jaws.

The neutron spectra simulated in the study by Zanini et al. show a slight shift towards lower energies for the field using the MLC when compared to the open field. This shift lowers also the mean energy, which could be responsible for the change of the ratio between the open field and the intensity-modulated field with depth in the phantom seen in this study, as the moderation of neutrons is energy dependent. Dedicated Monte Carlo simulations would be necessary to assess this in detail.

4.5 Conclusion

The findings of this study indicate that the number of applied monitor units during a radiotherapy treatment alone is not predictive for the neutron dose equivalent the patient receives. Outside the treatment volume in larger depth 35 % less neutron dose equivalent was delivered than expected for a MU scaling of a factor of three to deliver the same dose to the target for IMRT compared to the open field. As a consequence, the predicted increase of second cancer induction rates because of neutrons from intensity-modulated treatment techniques at large photon beam energies might have been overestimated. The neutron dose to the patient is dependent on several parameters, such as the type and material of the multileaf collimator and the photon energy, which were not investigated in this work and should be included in further studies.

Chapter 5

Systematic Measurements of Whole-Body Dose Distributions for Various Treatment Machines and Delivery Techniques in Radiation Therapy

Roger A. Hälg[1], Jürgen Besserer[1], and Uwe Schneider[1,2]

[1] Institute for Radiotherapy, Radiotherapie Hirslanden AG, Aarau, Switzerland

[2] Vetsuisse Faculty, University of Zurich, Zurich, Switzerland

Submitted to
Medical Physics
2012

5.1 Introduction

Continuous efforts in research and development in radiation therapy led to new treatment modalities and further optimised delivery techniques. Two examples are the introduction and application of intensity-modulated radiation therapy [11] (IMRT) and volumetric modulated arc therapy [83] (VMAT). These modern radiotherapy treatment techniques suggest an increase in cancer cure rates, while simultaneously unwanted side effects can be reduced [84]. There are clear therapeutic advantages using these techniques, for instance, the improved conformity of the dose to the target volumes and larger dose gradients in the healthy tissue. But there are also disadvantages, such as an increase in the beam-on time required to deliver the same dose to the target volume in intensity-modulated techniques compared to conventional techniques. Concerns have been raised that there could be an increase in radiation-induced malignancies with the application of these techniques, in particular, in younger patients [5, 85]. These concerns are mainly based on the increased number of monitor units needed for the same dose to the target, the larger number of beam entrance ports and consequently, the large volume irradiated with low doses and the impact on the integral dose of the patient [5]. It is, therefore, important to assess the complete dose distribution received by a radiotherapy patient, including the primary dose distribution, dose from stray radiation, and imaging dose as well as possible secondary neutron dose contributions, when comparing different delivery techniques. Advances in cancer therapy over the last few decades have resulted in longer survival times after treatment, which necessitates an investigation into the influence of the dose distribution on the long term health of cancer patients [7]. This includes investigations into secondary cancer incidence.

Contemporary treatment planning systems can calculate precisely and efficiently the distribution of absorbed dose inside the primary field and close to the treatment field. But to assess the dose to organs further away from the primary radiation field, measurements or Monte Carlo simulations are necessary. There are numerous studies in the literature where out-of-field doses were measured and simulated. A comprehensive list of such studies examining dose contributions for different treatment machines and delivery techniques can be found in a review paper by Xu et al. [19]. Early dosimetry studies focused mainly on occupational radiation safety for medical personnel, whereas later studies determined out-of-field dose and effective dose for patient safety, including modern treatment techniques. Comparative measurements were usually performed on

the same treatment machine to investigate differences in dose distribution for various treatment plans, delivery techniques, and nominal beam energies. Only a small number of studies included different linear accelerators for comparison of out-of-field dose. Direct comparisons between different dosimetry studies are difficult, because the measurement conditions and irradiation intentions differ substantially.

The aim of this study was to measure in- and out-of-field absorbed dose in an anthropomorphic phantom using the same measurement setup and irradiation intention. The doses from typical radiotherapy patient plans were measured using different treatment techniques and therapy machines. The doses were examined with respect to geometrical and anatomical considerations.

5.2 Materials and Methods

5.2.1 Treatment Intention and Planning

The clinical treatment intention of this study was the curative irradiation of a rhabdomyosarcoma of the prostate for an adolescent patient, represented by an anthropomorphic phantom. The planning CT of the phantom and the contouring of the target structures and organs for the phantom (done by a physician) were performed at one institution. The dose prescription for the irradiation was $26 \times 2.0\,\mathrm{Gy}$ for the 3D-conformal treatment (with and without hard wedges) and $23 \times 2.2\,\mathrm{Gy}$ for the treatment modalities using intensity modulation. For the stereotactic irradiation of the rhabdomyosarcoma, a dose prescription of $5 \times 5.8\,\mathrm{Gy}$ was chosen. The fractionation schemes were matched to represent the same biological target dose using the linear-quadratic model and an α/β ratio of 2.8 [71]. The dose constraints for organs at risk were adapted accordingly, using α/β values for the corresponding organs. This information was sent to all the participating institutions along with a planning guideline (see Appendix 5.B) containing the CT calibration curves, dose prescription, planning structures, dose constraints, and the location of the isocenter. The treatment planning of the simulated treatment of the anthropomorphic phantom was performed at every hospital using the specified dose constraints to targets and organs at risk.

5.2.2 Therapy Modalities

The series of measurements consisted of several photon therapy irradiations. All measurements and detector readouts were performed by the same person. This procedure ensured the consistency of the irradiations and measurements at the different sites. The photon beams were delivered by treatment machines from the manufacturers Accuray (Accuray, Sunnyvale, CA, USA), Elekta (Elekta AB, Stockholm, Sweden), Siemens (Siemens AG, Healthcare Sector, Erlangen, Germany), and Varian (Varian Medical Systems, Palo Alto, CA, USA). The treatment irradiation techniques included in this study were 3D-conformal (3DCRT), 3D-conformal using hard wedges (3DCRT hard wedge), volumetric modulated arc therapy (VMAT), flattening filter free (FFF) volumetric modulated arc therapy, intensity-modulated radiotherapy (IMRT), helical TomoTherapy, and stereotactic irradiation (CyberKnife). The measurements were performed at Canton Hospital Aarau, Aarau, Switzerland (Siemens Oncor Avant-Garde), Canton Hospital St. Gallen, St. Gallen, Switzerland (Elekta Synergy), Centre Hospitalier Universitaire Vaudois, Lausanne, Switzerland (Accuray TomoTherapy Hi-Art 2, Siemens Mevatron Primus), Radiotherapie Hirslanden AG, Aarau, Switzerland (Varian Clinac 21 iX), Radiotherapie Hirslanden AG, Zurich, Switzerland (Accuray CyberKnife), and University Hospital Zurich, Zurich, Switzerland (Varian TrueBeam).

All the photon beams for this work had a nominal energy of 6 MV according to BJR-11 [72]. The treatment machines and their corresponding $TPR_{20,10}$ values, as well as the treatment planning system (TPS) used and the applied irradiation techniques are listed in Table 5.1.

An overview of the fractionation scheme for the different treatment modalities, the type of multileaf collimator (MLC, static: SMLC or dynamic: DMLC), the number of fields, and the resulting total number of monitor units for the whole course of treatment can be found in Table 5.2.

5.2.3 Phantom and Detectors

In order to evaluate the therapeutic dose and the dose from stray radiation and to account for the patient anatomy, an adult anthropomorphic Alderson-Rando phantom (RSD Radiology Support Devices, Long Beach, CA, USA) was used. The phantom consisted of 35 transversal slabs, made of material that was tissue equivalent for photon beams and every slab contained holes for detectors. The dose measurements were performed using thermoluminescent dosimeters (TLDs) placed inside the Alderson-

Treatment machine	$TPR_{20,10}$	TPS	Technique
Accuray CyberKnife	0.626	MultiPlan 3.5.0 Raytrace	Stereotactic
Accuray TomoTherapy Hi-Art 2	0.614	TomoTherapy TPS 4.0 Convolution/superposition	Helical IMRT
Elekta Synergy	0.680	Eclipse AAA 8.6.14	IMRT
Siemens Mevatron Primus	0.673	XiO 4.64 Convolution/superposition	3DCRT hard wedge
Siemens Oncor Avant-Garde	0.673	Pinnacle v8.0m Collapsed cone convolution	IMRT
Varian Clinac 21 iX	0.665	Eclipse AAA 8.6.14	3DCRT, IMRT, VMAT
Varian TrueBeam	0.631	Eclipse AAA 8.9	VMAT FFF

Table 5.1: Treatment machines used in this study, the corresponding $TPR_{20,10}$ values, treatment planning system, and the treatment techniques. The photon beams had a nominal energy of 6 MV.

Treatment plan	Number of fractions	Dose per fraction	Type of MLC	Number of fields	Total MU
Accuray CyberKnife	5	5.8 Gy	SMLC	415 beams	34850
Accuray TomoTherapy	23	2.2 Gy	DMLC	—	77303
Elekta IMRT	23	2.2 Gy	SMLC	5 fields	14283
Siemens hard wedge	26	2.0 Gy	SMLC	5 fields	16536
Siemens IMRT	23	2.2 Gy	SMLC	9 fields	11615
Varian 3DCRT	26	2.0 Gy	DMLC	4 fields	7384
Varian IMRT	23	2.2 Gy	DMLC	5 fields	15732
Varian VMAT	23	2.2 Gy	DMLC	1 arc	11109
Varian VMAT FFF	23	2.2 Gy	DMLC	2 arcs	13984

Table 5.2: Measured treatment plans, applied dose per fraction, type of MLC, number of fields, and corresponding number of monitor units (MU). The photon beams had a nominal energy of 6 MV.

Rando phantom. The dosimeters had the form of disks with a diameter of 4.50 mm and a thickness of 0.60 mm. This geometry allowed to position the detectors directly in the phantom slabs without casing. The trading name of the detectors was TLD-100H (Thermo Fisher Scientific, Waltham, MA, USA) and they were made of lithium fluoride ($\sim 7.5\,\%$ ^{6}Li) and doped with magnesium, copper, and phosphorus (LiF:Mg,Cu,P). The useful dose range of the dosimeters was 1 µGy to 20 Gy according to the manufacturer. The positions of the detectors were chosen to determine the dose profile along the medial patient axis and to assess the dose in different organs. The radiation sensitive organs were determined according to the ICRP recommendations [26]. A total of 184 measurement positions were selected in the phantom, facilitating the determination of a three-dimensional dose distribution. Each dosimeter used for measurements was assigned to an organ structure defined in the CT data of the Alderson-Rando phantom. This organ assignment was used to calculate mean organ doses. The dose along the medial patient axis was determined using 34 detectors spaced by 2.5 cm from the target (in the prostate) to the head. All the doses were determined in terms of absorbed dose to water.

5.2.4 Detector Calibration

The dosimeters were calibrated using the 6 MV beam of a Varian Clinac 21 iX and a RW3 solid water slab phantom (PTW, Freiburg, Germany). Measurements in a water tank were used to find a combination of field size and depth in the phantom which gave a dose profile as flat as possible (field size: 25 cm × 25 cm, depth: 14.7 cm, dose variation: ±0.5 %). The measurement TLDs were irradiated inside the primary field in batches of 50 detectors with a dose of about 100 mGy. The batches were placed in the solid water phantom inside a PMMA casing. The calibration dose was determined by ionisation chamber measurements (Farmer Ionization Chamber, PTW, Freiburg, Germany) at the position of the PMMA casing. Two batches of 16 TLDs were used for the evaluation of the background/transport signal. They were calibrated in the same way as the measurement dosimeters, but were not irradiated intentionally during a treatment measurement. Each detector batch contained four reference dosimeters, which were irradiated with a reference dose ($\sim$ 100 mGy) for each measurement.

For each TLD, a calibration factor in terms of dose per reader count was determined by performing a calibration measurement two to three days

before every measurement. These dose calibration factors (DCF) were determined using Equation (5.1),

$$k^i_{\mathrm{cal,raw}} = \frac{d_{\mathrm{cal}}}{C^i_{\mathrm{cal,raw}}}, \tag{5.1}$$

where $k^i_{\mathrm{cal,raw}}$ was the raw DCF of the i^{th} TLD, d_{cal} was the calibration dose determined by the ionisation chamber measurement, and $C^i_{\mathrm{cal,raw}}$ were the raw number counts from the detector readout.

The reader counts were then corrected for the background signal according to Equation (5.2) considering the sensitivity variation between the background dosimeters and the dosimeter of interest

$$C^i_{\mathrm{cal}} = C^i_{\mathrm{cal,raw}} - \frac{k^i_{\mathrm{cal,raw}}}{k^{\mathrm{B}}_{\mathrm{cal,raw}}} \cdot C_{\mathrm{B}}, \tag{5.2}$$

where C^i_{cal} were the corrected reader counts of the i^{th} TLD for the calibration measurement, $k^{\mathrm{B}}_{\mathrm{cal,raw}}$ was the mean raw dose calibration factor of all the background dosimeters, and C_{B} were the mean reader counts of all the background dosimeters from the corresponding measurement irradiation.

These corrected counts C^i_{cal} were used in Equation (5.1) instead of the raw reader counts $C^i_{\mathrm{cal,raw}}$ to determine the final dose calibration factor (k^i_{cal}) for each dosimeter and calibration.

A microprocessor-controlled annealing procedure in a dedicated oven (Fimel ETT Annealing Oven, PTW, Freiburg, Germany) was applied to all the TLDs after each readout. They were placed in a metallic container, in the same batches as for calibration. A linear heating ramp ($\sim 35\,^{\circ}\mathrm{C\,min^{-1}}$) up to 240 °C was used. The TLDs were kept at this maximum temperature for 10 min before they were cooled down in the oven to 50 °C with a constant cooling rate ($\sim 5\,^{\circ}\mathrm{C\,min^{-1}}$).

5.2.5 Detector Readout

For the readout of the dosimeters, a Fimel PCL3 isothermal TLD reader (PTW, Freiburg, Germany) was used. This reader had two isothermal heating zones, one for preheating and one for the actual readout of the dosimeters. The preheating and readout temperatures were 100 °C and 240 °C, respectively. Each TLD was placed in a metallic cupel for the

automated readout procedure. The same batches for the calibration were used to load the stack of the reader. The signal of the dosimeters was determined in terms of collected photomultiplier charge for 30 s during the readout of the TLDs.

Manufacturer recommended optical filters were available for the TLD reader to adapt the dynamic range of the photomultiplier to the light signal of the TLDs and, therefore, to the measured dose. A grey filter was applied to the two batches of detectors used for the dose measurements inside and close to the treatment fields, where the expected dose was higher. A blue filter (smallest available light absorption) was used for the other two batches for the measurement locations further away from the isocenter towards the head of the phantom. Each optical filter was assigned a batch of background dosimeters to correct the corresponding measurement TLDs for background signal.

The reference dosimeters of each batch were used to correct for the daily variation in the output of the TLD reader and to account for a possible drift in the output during one readout cycle. Therefore, two of the four reference dosimeters were read out at the beginning of the batch and two at the end. The values of the dose per count from the reference irradiation relative to the values from the corresponding calibration were used to calculate the sensitivity of the readout at the beginning and at the end of the readout cycle. A linear interpolation between these two values (k_{drift}) was used to correct the readout of the TLDs used for measurement in that batch. The mean correction factor for the daily variation was 1.00 and the maximum correction was 8 %. The drift correction k_{drift} during the readout of one batch had a mean value of 2 % and a maximum of 6 % over all measurements.

5.2.6 Dose Determination

The measured dose of each dosimeter was calculated by means of Equation (5.3), where the above mentioned calibration and correction factors were applied and the background signal was subtracted

$$D^i = \left(k^i_{\mathrm{cal}} \cdot C^i - k^{\mathrm{B}}_{\mathrm{cal}} \cdot C_{\mathrm{B}}\right) \cdot k^i_{\mathrm{drift}}, \tag{5.3}$$

where D^i was the determined absorbed dose to water of the i^{th} TLD, k^i_{cal} and $k^{\mathrm{B}}_{\mathrm{cal}}$ were the background corrected DCF from the corresponding calibration, C^i were the reader counts from the measurement, and k^i_{drift} was the linear interpolation of the drift correction for the i^{th} readout position

in the cycle.

5.2.7 Energy Correction

The readout signal of thermoluminescent dosimeters depends on the energy of the impinging photons. Therefore, the measured dose depends on the photon spectrum at the measurement position. For measurements of photon dose from radiotherapy, this could lead to differences in the measured dose depending on the position in the phantom, especially for measurements comparing doses inside and outside of the primary beam. The energy dependent response of the thermoluminescent material used in this study (LiF:Mg,Cu,P) was investigated by several groups [86–89]. Monte Carlo simulations of photon spectra for 6 MV photon beams inside and outside of the primary beam were performed by Edwards and Mountford [90] and by Scarboro et al. [91]. They showed that the mean energy of the photons was shifted from about 1.5 MeV on the central axis down to about 0.3 MeV outside of the primary beam, close to the field edge.

In order to analyse if this energy shift had an impact on the dose measurements in this study, the estimated detector response relative to the infield response was calculated using the spectra simulated by Scarboro et al. for a depth of 1.6 cm and distances of 15 cm and 50 cm from the central axis. According to the analytical response function determined by Duggan et al. [87] for LiF:Mg,Cu,P thermoluminescent material, a reduction of the response by 7 % and 6 % relative to the infield response was calculated for the distances 15 cm and 50 cm from the central axis, respectively. The response curve measured by Davis et al. [86] led to a reduction of the response by 18 % and 17 % for the same spectra. To verify this, a randomly selected subset of the TLDs was used. The measurement setup was chosen to measure the dose at the positions of the simulated spectra mentioned above. The dose was measured at each position with TLDs and a Farmer ionisation chamber. The measured correction factors for the TLDs readout with the grey filter were 1.15 and 1.12 for the positions 15 cm and 50 cm from the central axis, respectively. For the same positions, the correction factors were 1.12 and 1.05 for the TLDs readout using the blue filter. The correction factor was determined for two more positions, namely, in 10 cm depth at 15 cm and 30 cm from the central axis. The values were 1.11 and 1.12 for the grey filter, whereas they were 1.08 and 1.08 for the blue filter. Finally, a general energy correction factor of 1.1 was chosen for all the out-of-field measurements.

5.2.8 Dose Linearity

The linearity of the dose response of the TLD readout signal was checked with a randomly selected subset of the dosimeters within the primary beam of the Varian Clinac 21 iX. A least-squares fit to the measured doses over the whole dose range of this study (250 µGy–3.4 Gy) showed a slope of 0.97 ionisation chamber dose/TLD dose and an intercept of 4.2 mGy ionisation chamber dose, with a corresponding R^2 of 0.9998. The quality of the fit indicated a linear behaviour of the TLD signal with dose and, therefore, no correction for non-linearity was applied.

5.2.9 Measurement Reproducibility

In order to investigate the long term stability of the TLD readout and to estimate the reproducibility of the dose measurements, the readout signal per applied dose of the reference TLDs was analysed for all the calibration and reference irradiations. The standard deviation was calculated for each of the 20 reference TLDs for a total of 35 irradiations. The reproducibility of a complete treatment was checked by repeating the measurement for two treatment techniques (3D-conformal and intensity-modulated radiation therapy on the Varian Clinac 21 iX) and comparing the determined dose for every measurement position.

5.3 Results

The reproducibility of the dose measurements was determined by the mean standard deviation of all the reference TLDs for a total of 35 irradiations and was 4 % with minimum and maximum of 2 % and 5 %, respectively. In Figure 5.1, the distribution of the readout signal per applied dose normalised to the mean value of each TLD, is shown in a box-and-whisker plot for the 20 reference TLDs.

The mean values of the relative doses and the standard deviation for the reproducibility of the measurements of a complete treatment irradiation were 0.99 ±0.05 and 0.98 ±0.07 for the 3DCRT and the IMRT irradiations, respectively.

The following figures show the dose profile along the medial patient axis from the isocenter in the prostate ($x = 0$ cm) to the head ($x = 82.5$ cm) for different treatments.

Figure 5.2 shows a semi-logarithmic comparison of the dose along the medial patient axis for the treatment techniques 3DCRT, IMRT, and VMAT

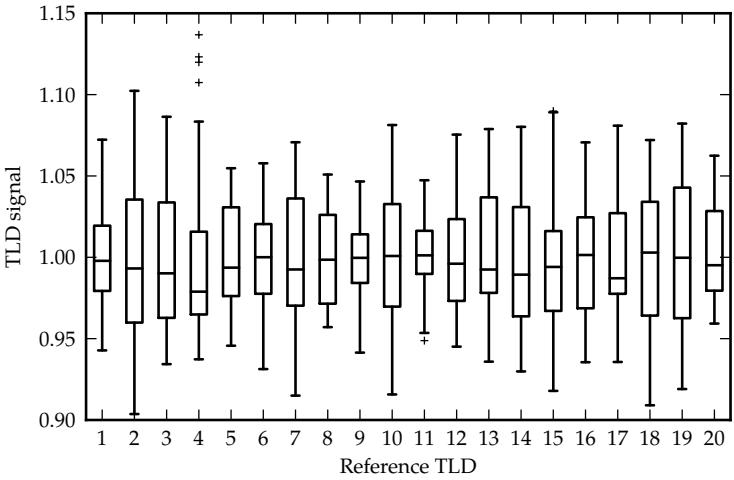

Figure 5.1: Reproducibility of the 20 reference TLDs for all the calibration and reference irradiations (35 in total). The TLD signal per dose normalised to the mean value of each TLD is shown in a box-and-whisker plot.

with and without flattening filter on the Varian Clinac 21 iX and Varian TrueBeam (VMAT FFF) linear accelerators. On the left, the absorbed dose is shown for the total treatment dose of the complete course of treatment, as the 3D-conformal treatment used a different fractionation scheme than the intensity-modulated treatments ($26 \times 2.0\,\mathrm{Gy}$ versus $23 \times 2.2\,\mathrm{Gy}$). On the right, the dose is plotted relative to the dose of the 3D-conformal irradiation.

The dose on the medial patient axis from different intensity-modulated radiotherapy treatments using linear accelerators from the manufacturers Elekta, Siemens, and Varian, and a TomoTherapy unit are shown in Figure 5.3. On the left-hand side, the dose is plotted for the complete course of treatment for comparison with the other figures, although all IMRT treatments had the same fractionation scheme. To correct for a systematic misalignment of the isocenter on the Elekta linear accelerator during the measurement, this curve was shifted by $-0.5\,\mathrm{cm}$. The relative dose distribution compared to the 3D-conformal irradiation on the Varian linear accelerator is plotted on the right-hand side.

A comparison of different treatment techniques and machines is depicted in Figure 5.4. The hypo-fractionated CyberKnife irradiation, the

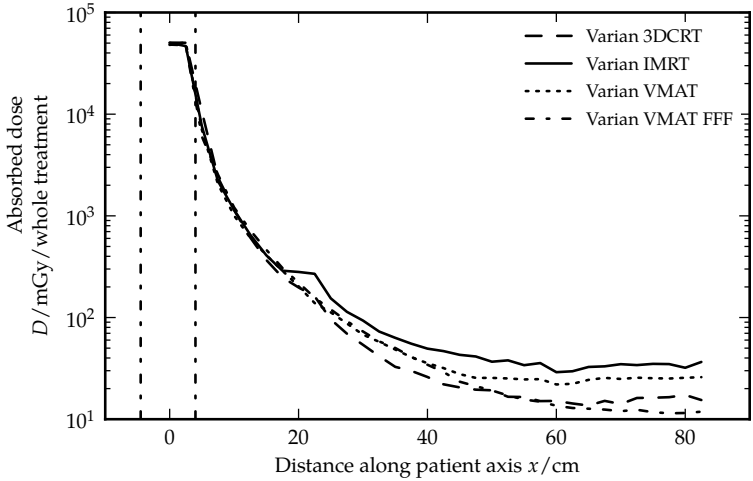

(a) Varian treatments

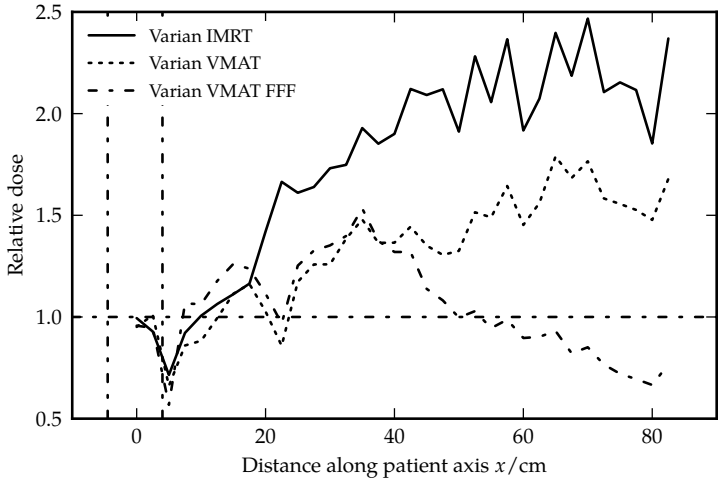

(b) Varian treatments relative

Figure 5.2: Dose distribution along the medial patient axis. The isocenter corresponds to $x = 0\,\text{cm}$ and the vertical lines represent the border of the target volume along this axis. The photon beams had a nominal energy of 6 MV. (a) Total course of treatment ($26 \times 2.0\,\text{Gy}$ (3DCRT) or $23 \times 2.2\,\text{Gy}$) for different techniques on the Varian Clinac 21 iX and TrueBeam (VMAT FFF) linear accelerators with dynamic MLC. (b) Dose relative to the 3DCRT irradiation.

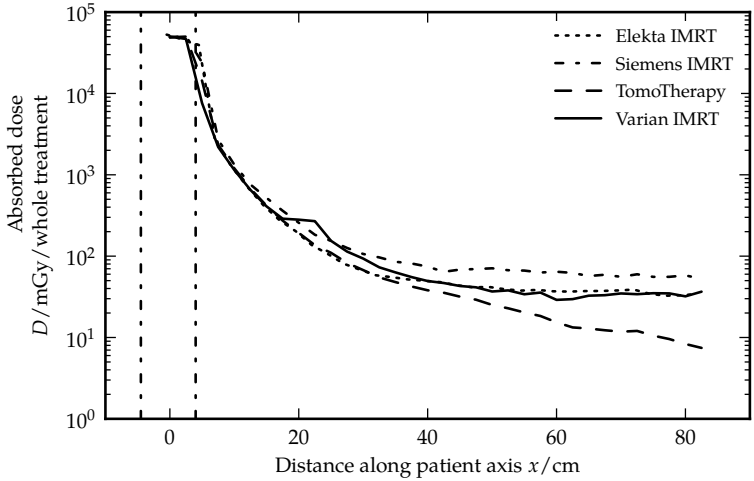

(a) IMRT treatments

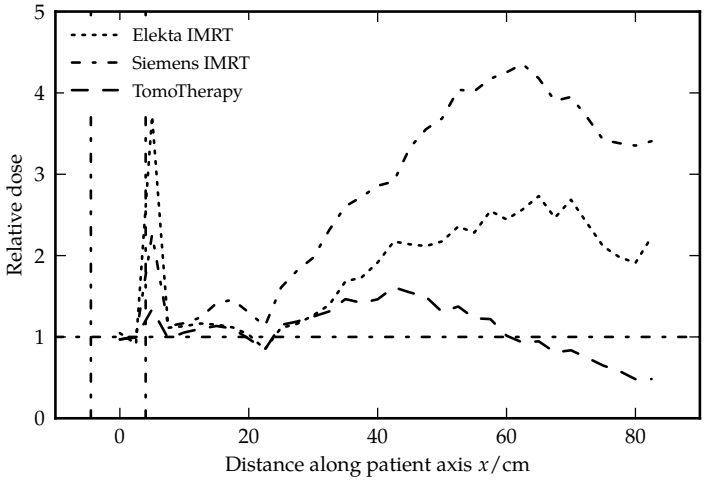

(b) IMRT treatments relative

Figure 5.3: Dose distribution along the medial patient axis. The isocenter corresponds to $x = 0$ cm and the vertical lines represent the border of the target volume along this axis. The photon beams had a nominal energy of 6 MV. (a) Total course of treatment (23×2.2 Gy) for IMRT treatments on different treatment machines with static MLC (Elekta and Siemens) and dynamic MLC (TomoTherapy and Varian). (b) Dose relative to the Varian 3DCRT treatment.

3D-conformal treatments with and without hard wedges, and the helical TomoTherapy technique are plotted. The left graph shows the dose per total treatment dose of the whole course of treatment to account for the different fractionation schemes. On the right-hand side, the dose is plotted relative to the dose of the 3DCRT irradiation without hard wedges.

A comparison of the resulting organ doses for the intensity-modulated treatments is listed in Table 5.4. The mean organ doses of the treatment technique 3D-conformal with and without hard wedges are presented in Table 5.5. In Table 5.6, the volumetric modulated arc therapies and the stereotactic CyberKnife irradiation are compared in terms of the mean organ doses. In addition to the mean organ doses, the effective doses outside the treated volume were calculated according to ICRP [26] and are listed in Table 5.7.

5.4 Discussion

Currently 3D-conformal therapy is a well-established technique in clinical routine against which new innovations and adaptations of techniques or protocols are usually compared. The measurements for this study allowed a comparison of different treatment techniques on the same linear accelerator (3DCRT vs IMRT and VMAT on the Varian Clinac 21 iX, see Figure 5.2) and different treatment machines compared to each other (Figures 5.3 and 5.4).

Along the medial patient axis a dose spike was visible for the IMRT treatment on the Varian Clinac 21 iX shown in Figure 5.2 (around $x = 22.5\,\text{cm}$). This is consistent with the findings of Ruben et al. and has been reported before [92]. Ruben et al. explain this spike by leakage radiation penetrating through the Y-jaw of the secondary collimator before passing through a gap between the lateral edge of the MLC and the primary collimator. This spike in the dose profile of the Varian IMRT irradiation leads to a local relative dose reduction for the other intensity-modulated treatments. This local spiking effect is present for the 3D-conformal irradiation too, but to a lesser extent.

For the discussion of the stray dose from different treatment modalities, the dose along the medial patient axis was separated into three regions, a high dose region with doses larger than 5 Gy (0 cm–7.5 cm from the isocenter), a medium dose region from 0.5 Gy to 5 Gy (7.5 cm–15 cm), and a low dose region with doses up to 0.5 Gy (15 cm–82.5 cm). This classification was chosen to represent the regions corresponding to different

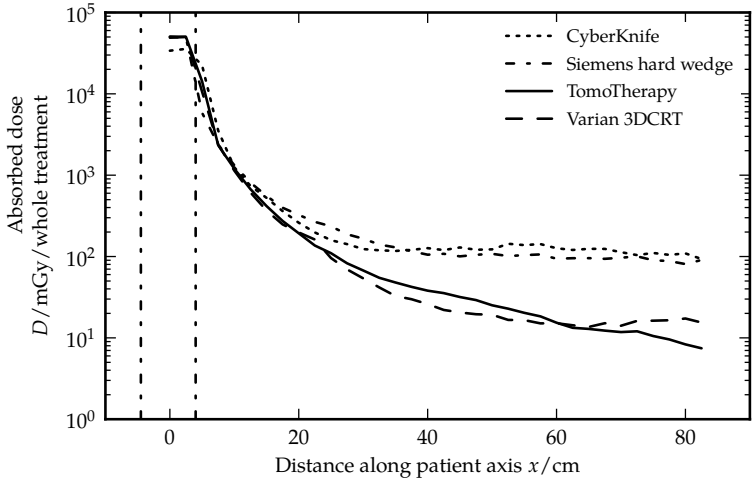

(a) Various treatments

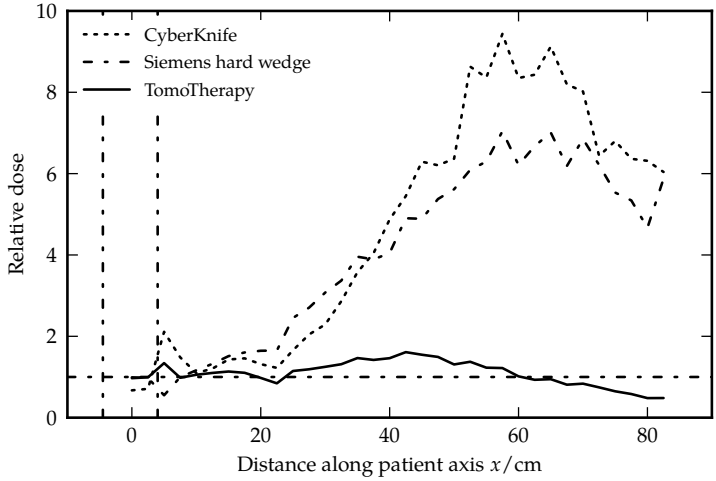

(b) Various treatments relative

Figure 5.4: Dose distribution along the medial patient axis. The isocenter corresponds to $x = 0$ cm and the vertical lines represent the border of the target volume along this axis. The photon beams had a nominal energy of 6 MV. Static MLCs were used except for the TomoTherapy. (a) Total course of treatment (26×2.0 Gy 3DCRT with and without hard wedges, 23×2.2 Gy TomoTherapy or 5×5.8 Gy CyberKnife) for different techniques and treatment machines. (b) Dose relative to the 3DCRT irradiation on the Varian linear accelerator.

risks for cancer induction. According to Travis et al.[93], the highest incidence of secondary cancer in patients treated for Hodgkin's disease was found in the intermediate dose region, followed by the high and low dose regions, respectively. It should be noted that the quantification of cancer risk as a function of dose is not trivial for the medium and high dose regions. In the low dose region, however, the linear model of cancer risk can be applied and thus risk is proportional to the mean dose.

5.4.1 High dose region (> 5 Gy)

The high dose region contains the therapeutic dose from the primary radiation, which is the main contributor to dose. Beside this, the main contributors of stray dose in the high dose region are phantom and collimator scatter. These are mainly dependent on the dose to the target and the collimator geometry; therefore, the stray dose in this region does not scale with the monitor units of the specific plan. It is difficult to compare the measured doses in this region, as several factors influence the dose which can lead to large differences in this region of large dose gradients. Misalignment in the positioning of the phantom can change the measured dose. Another source of uncertainty is the quality of treatment planning, which has an impact on the conformity of the dose distribution. Although all treatment plans were calculated on the same planning CT with the same target structures and dose prescription, the quality of a treatment plan depends on the experience of the treatment planner and finding an optimal plan is an iterative process. Since the treatment plans for the measurements with the Varian treatment machines were performed with the same treatment planning system and for the Clinac 21 iX by the same treatment planner, the dose distributions can be more reliably compared, even in the high dose region. A direct comparison of the dose in the region of large dose gradients between the Varian treatments and the IMRT treatments at the Siemens and Elekta linear accelerators must be performed with care. To illustrate this, the dose calculated by the treatment planning systems for different linear accelerators and delivery techniques was plotted for the high dose region in Figure 5.5. It can be clearly seen that in the region of the dose gradient, the different treatment plans result in different dose gradients.

The dose along the medial patient axis measured in this study for the high dose region is shown in Figure 5.6. Intensity-modulated treatments are expected to produce larger dose gradients at the field borders. This is due to lower phantom and collimator scatter for intensity-modulated

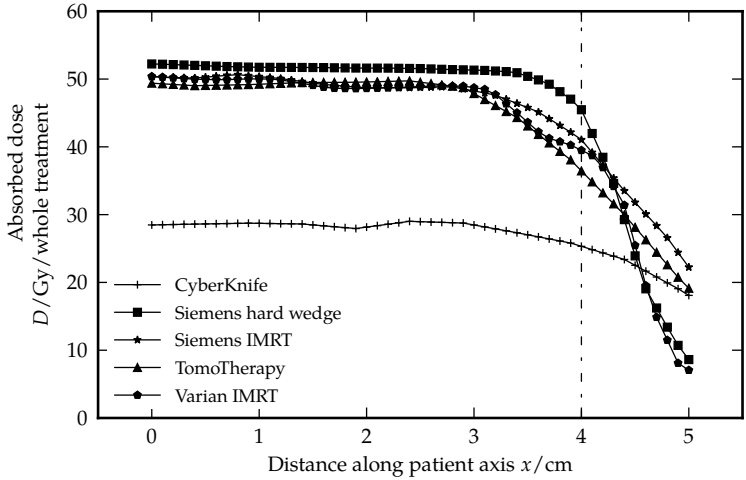

Figure 5.5: Dose distribution along the medial patient axis calculated by the corresponding treatment planning system at the institution where the measurement was performed. The photon beams had a nominal energy of 6 MV and static MLCs were used for the CyberKnife and the Siemens linear accelerators, whereas dynamic MLCs were used for the TomoTherapy and the Varian linear accelerator.

treatments, as the treatment field sizes are generally smaller. When the doses at the first measurement point outside of the field were compared, this reduced dose was qualitatively visible for Varian IMRT and VMAT treatments, although the differences were within the measurement uncertainty. The Siemens and Elekta IMRT irradiations showed smaller dose gradients compared to the other IMRT and VMAT treatments. For the Siemens IMRT measurement, this was expected from Figure 5.5. The dose measured for all the treatments at Varian linear accelerators, the irradiation of the 3D-conformal plan with hard wedges at the Siemens linear accelerator, and at the TomoTherapy, were comparable in the high dose region. The dose of the CyberKnife irradiation was higher by a factor of two, compared to the 3D-conformal irradiation. This was expected, since the CyberKnife treatment was the only non-coplanar treatment, resulting in additional dose to volumes in the cranio-caudal direction. The dose of the Elekta IMRT irradiation close to the field edge was not directly comparable to the other measurements, because of the misalignment of the isocenter. This effect was most pronounced in the high dose region.

The minimal dose values, which can be viewed as an approximate

quantitative measure of cancer-risk in this region, are given in Table 5.3.

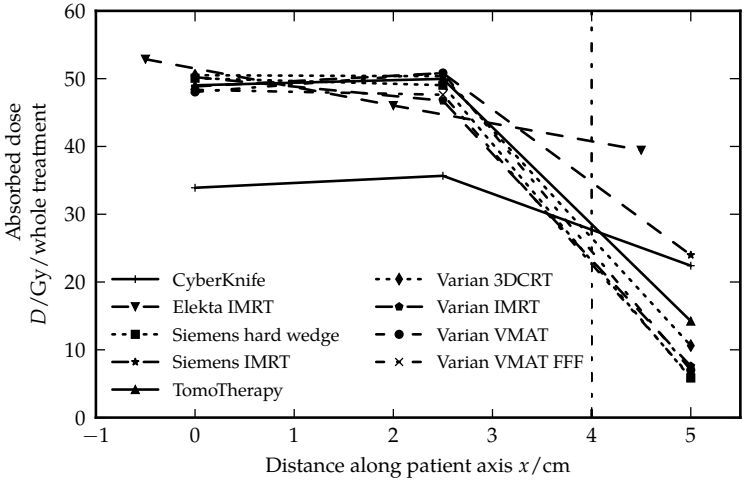

Figure 5.6: Comparison of the dose distributions of all the investigated treatment techniques and machines in the high dose region. The photon beams had a nominal energy of 6 MV and static MLCs were used for the CyberKnife and the Elekta and Siemens linear accelerators, whereas dynamic MLCs were used for the TomoTherapy and the Varian linear accelerators (except for the 3DCRT irradiation).

5.4.2 Medium dose region (0.5 Gy–5 Gy)

In the intermediate dose region, the dose is mainly deposited by phantom and collimator scatter radiation. Compared to the high dose region, collimator scatter is decreased and the phantom scatter becomes more dominant. The amount of stray dose is, as in the high dose region, mainly determined by the dose to the target volume and the collimator geometry and not by the number of monitor units applied. In general, the dose fall off was shallower compared to the high dose region, and the differences between the treatment techniques and machines were reduced as can be seen in Figure 5.7. To quantify the dose in the intermediate dose region, a logarithmically weighted mean dose was calculated, which accounts for the nearly exponential dose fall off and is listed in Table 5.3. Approximately, the same dose from the Varian 3DCRT, Varian IMRT, and the TomoTherapy irradiations was measured in the medium dose range.

The IMRT treatments using the Elekta and the Siemens linear accelerators showed a 15 % larger dose than the Varian IMRT. This could be explained by the shifted dose gradients of these plans. The measurement of the Varian VMAT plan showed the lowest intermediate doses. This can be explained by the reduced phantom scatter compared to the other treatments, since VMAT usually has the smallest possible field sizes. The dose from the flattening filter-free VMAT irradiation was 20 % higher. This difference could be due to the reduced beam energy of an unflattened beam, leading to an increased cross section of Compton scattering. The highest dose in this region was measured for the CyberKnife irradiation, as a direct consequence of the non-coplanar primary beams. The measurement of the treatment at the Siemens Mevatron linear accelerator using the hard wedges, showed a clear increase in dose compared to the 3D-conformal irradiation without hard wedges. Already at distances about 10 cm from the treatment field, the additional stray radiation from the hard wedges can clearly be observed in the dose measurement.

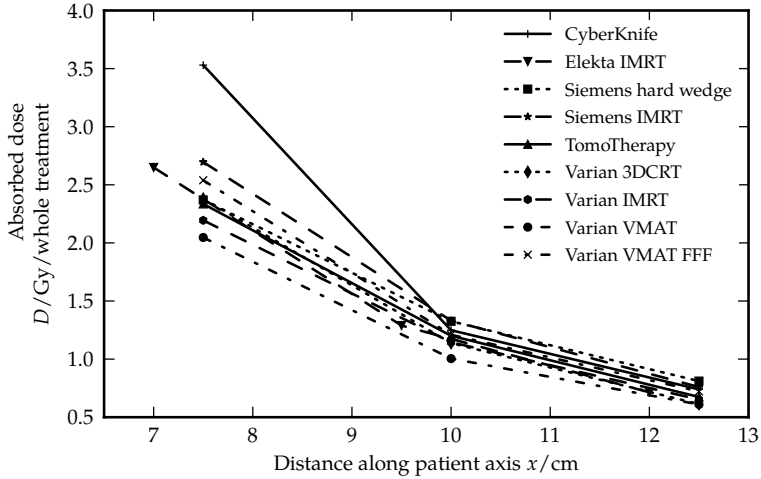

Figure 5.7: Dose distribution along the medial patient axis in the medium dose region for all measured treatment techniques and machines. The photon beams had a nominal energy of 6 MV and static MLCs were used for the CyberKnife and the Elekta and Siemens linear accelerators, whereas dynamic MLCs were used for the TomoTherapy and the Varian linear accelerators (except for the 3DCRT irradiation).

5.4.3 Low dose region (< 0.5 Gy)

For volumes in the low dose region, head leakage, and phantom scatter contribute to the dose to the patient. For distances far away from the isocenter, the dose to the patient is mostly determined by the amount of head leakage. This is illustrated in Figure 5.8 where the dose remained nearly constant for distances larger than 40 cm from the central axis. The dose was higher for intensity-modulated treatments (with flattening filter) far away from the isocenter, since the dose from head leakage is proportional to the number of applied monitor units. However, as head leakage is only a part of the dose from stray radiation in the low dose region, the mean dose increase is not directly proportional to the monitor units. One exception was the IMRT administered with the Siemens linear accelerator, which showed a much larger stray dose to monitor units ratio. The CyberKnife treatment was applied with nearly 5 times the monitor units of the 3D-conformal irradiation, resulting in 2.7 times the dose. When intensity modulation was applied with flattening filter-free linear accelerators, head scatter, and leakage was obviously lower. The stray dose was in these cases comparable to a static treatment, because the higher number of monitor units required for the intensity modulation was balanced by the removal of the flattening filter. When hard wedges were used, the number of monitor units was also larger when compared to an open field irradiation (a factor of 2.2) and therefore the dose from stray radiation was increased. In summary, static and flattening filter-free treatments delivered the lowest dose to the regions far away from the treatment field. The investigated IMRT treatments resulted in a dose which scaled approximately with the applied monitor units when compared to each other. On the other hand, the stray dose from IMRT did not scale with monitor units when compared to static treatments. Since CyberKnife treatments require large amounts of monitor units, the resulting dose from stray radiation was highest together with the static hard wedge treatment. The mean stray dose values for this region are given in Table 5.3.

In clinical practise, a usual way to compare different treatment plans in terms of stray dose is to compare the number of monitor units applied. However, the presented measurements showed that depending on the position where the stray dose was determined, the influence of the number of monitor units of the individual plan is not necessarily observable. As discussed above for the three dose regions, the specific processes which add together to the total stray dose have different sources depending on the distance to the field edge. The dependence of collimator and phantom

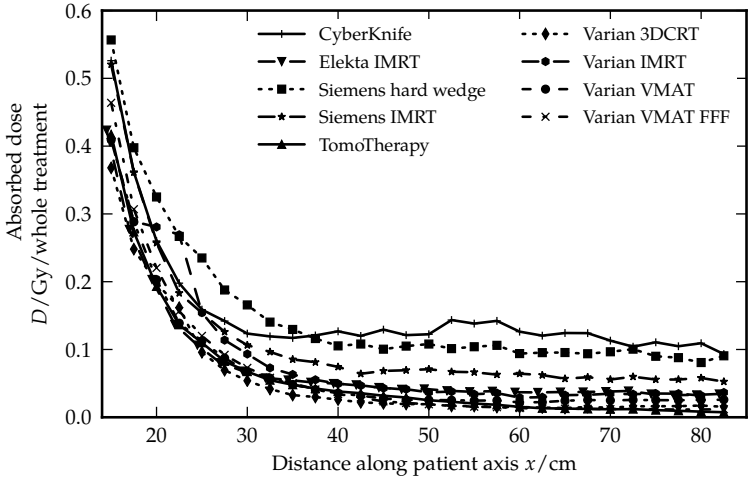

Figure 5.8: Stray doses far away from the treatment field for all treatment techniques and machines measured in this study. The photon beams had a nominal energy of 6 MV and static MLCs were used for the CyberKnife and the Elekta and Siemens linear accelerators, whereas dynamic MLCs were used for the TomoTherapy and the Varian linear accelerators (except for the 3DCRT irradiation).

Treatment plan	"High dose" minimum dose	"Medium dose" logarithmic averaged dose	"Low dose" mean dose
	Gy	Gy	Gy
Accuray CyberKnife	22.4	1.48	0.154
Accuray TomoTherapy	14.2	1.24	0.063
Elekta IMRT	39.4	1.35	0.077
Siemens hard wedge	5.8	1.37	0.153
Siemens IMRT	24	1.4	0.111
Varian 3DCRT	10.6	1.18	0.057
Varian IMRT	7.6	1.18	0.088
Varian VMAT	7	1.08	0.069
Varian VMAT FFF	6	1.3	0.067

Table 5.3: Measured treatment plans and corresponding dose values in the different dose regions. The stray dose is given per whole course of treatment. The photon beams had a nominal energy of 6 MV and static MLCs were used for the CyberKnife and the Elekta and Siemens linear accelerators, whereas dynamic MLCs were used for the TomoTherapy and the Varian linear accelerators (except for the 3DCRT irradiation).

scatter on the number of monitor units is less pronounced compared to the head leakage. Therefore, the effect of the number of monitor units of a treatment is most obvious in the low dose region. The ratio of the stray dose to the number of monitor units is mainly determined by the amount of head leakage per monitor unit, which is machine dependent and thus different for the linear accelerators investigated. In the region where the collimator and phantom scatter are the main components of the stray dose, the dose differences are bigger and the machine design is more important than the monitor units applied. Since intensity-modulated treatments produce less phantom scatter than static treatments, the impact of the number of monitor units on stray dose is more pronounced for IMRT. The amount of intensity modulation will determine the location, relative to the field edge, where the influence of the number of monitor units becomes relevant for the stray dose. This is presumably closer to the treatment field for intensity-modulated treatments compared to static irradiations.

Although the application of effective dose must be viewed with care when applied to radiotherapy dose distributions, the net effect when combining the three dose regions was also expressed in terms of effective dose calculated outside the treated volume (Table 5.7). It can be seen that the effective dose for IMRT treatments increases by 10 % to 30 % when compared to 3D-conformal therapy, which is much lower than the monitor unit scaled effective dose.

5.4.4 Comparison to neutron stray dose

The total stray dose to a patient can be divided into different contributions. For instance Ruben et al. [92] analysed the amount of stray dose from internal scatter (phantom or patient), collimator scatter, and leakage contributions of photon irradiations using 3DCRT and IMRT techniques on a Varian linear accelerator. For high energy photon (> 10 MV) and proton treatments, neutrons are produced in addition which contribute to the total stray dose. In another study, the neutron dose equivalent for various radiation qualities, treatment machines, and delivery techniques was evaluated using the same treatment intention and phantom as in this study [94] (chapter 3 of this thesis). This allowed a direct comparison of the stray dose from neutrons and from 6 MV photons. The photon dose from the 3D-conformal irradiations with and without hard wedges were compared to the neutron dose equivalent from a photon irradiation using a 3D-conformal plan with a nominal energy of 15 MV and from a treatment with double scattered protons. The comparison of these doses along

the medial patient axis is shown in Figure 5.9. It is clearly shown that the neutron dose is well below the photon dose even far away from the treatment field. When comparing the photon stray dose from the 6 MV 3DCRT irradiation to the neutron dose from the 15 MV 3DCRT irradiation, the neutron dose was everywhere at least one order of magnitude lower than the photon dose. Even the treatment with the highest neutron dose in that study, the double scattered proton irradiation, resulted in a lower neutron dose than the photon stray dose from the 3DCRT irradiation. Unfortunately, it was not possible to measure the photon stray dose for the corresponding irradiations with the high energy photon beams. The detector system used in this study was not capable of measuring the photon stray dose in high energy photon beams, as the photo neutrons in these mixed fields perform nuclear interactions with the ^{6}Li present in the TLD material, which would give an unpredictable contribution to the measurement signal. This effect was reported before for TLD-100, which consist of the same material but with a different doping than TLD-100H [95]. Comparisons of photon stray dose for different photon beam energies showed that the stray dose for 6 MV and 15 MV was of the same order of magnitude [79]. The neutron stray dose for a 15 MV photon beam, which is plotted in Figure 5.9, was at least one order of magnitude lower than the photon stray dose. This shows that the photon stray dose is the main contribution to the total stray dose even far away from the field edge.

The investigation on the reproducibility showed a variation for dose measurements of the reference TLDs with a maximum standard deviation of 5 %. The maximum standard deviation was taken as the dose measurement uncertainty which is a typical value for TLD-100H measurements. The ratio of two repeated measurements of a complete treatment showed a maximum deviation of 7 % (standard deviation of all TLDs), which is consistent with the error of the ratio of two measurements with an uncertainty of 5 % each. In addition to the statistical uncertainty, the reproducibility measurement of a treatment plan includes also uncertainties in the positioning of the phantom and the variation of the linear accelerator output.

5.5 Conclusion

In this study, dose measurements using thermoluminescent dosimeters were performed to assess the stray dose from typical treatments in radiation therapy. The same treatment intention and measurement setup were

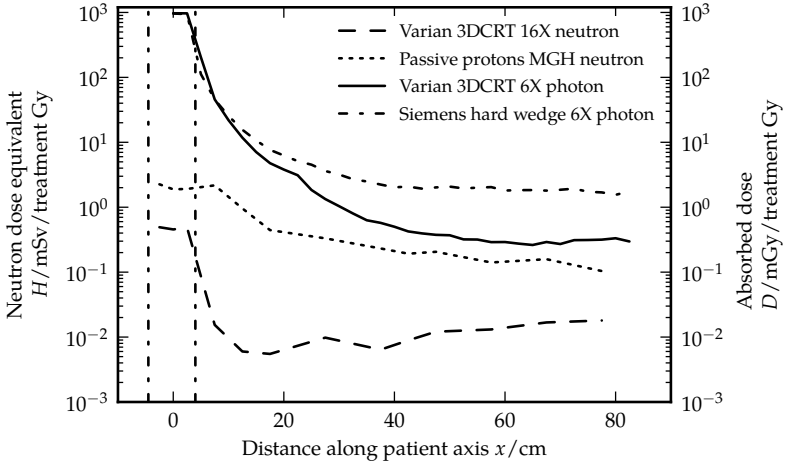

Figure 5.9: Comparison of the stray dose along the medial patient axis measured in this study (3DCRT technique with and without hard wedges) to the neutron dose equivalent from irradiations with high energy photons (3DCRT on a Varian Clinac 21 iX with 15 MV photons) and with protons (double scattered proton irradiation at Massachusetts General Hospital) for the same treatment intention and using the same phantom. The axis on the left hand side shows the neutron dose equivalent, the axis on the right hand side the photon stray dose. The neutron doses were taken from a study by Hälg et al. [94] (chapter 3 of this thesis).

used to perform a comparison of dose distributions for different treatment techniques and therapy machines. To our knowledge, this is the most comprehensive comparison in the literature. This study shows that modern techniques in radiation therapy can lead to doses from stray radiation far away from the treatment field, which are comparable to the dose from the well-established 3D-conformal radiotherapy technique. In particular, flattening filter-free techniques showed the lowest amount of stray dose (Varian TrueBeam VMAT and helical TomoTherapy). The investigated IMRT treatments resulted in doses which scaled approximately with the applied monitor units when compared to each other. Whereas the stray dose from IMRT did not scale with monitor units when compared to static treatments. The use of hard wedges to modulate the photon fluence leads to a considerable increase in dose from stray radiation (up to a factor of 6). The stereotactic treatment with the CyberKnife showed the highest amount of stray dose, although the prescribed dose for the whole course

of treatment was less than for the other techniques.

It was also shown in this work that photon stray dose dominates out-of-field dose for 15 MV irradiations. The neutron stray dose is an order of magnitude lower than the out-of-field dose from photons.

The analysis of the measured dose outside the treatment field showed considerable differences in the dose fall-off at the border of the field. The observed differences were consistent with the dose distributions calculated by treatment planning systems and it can be concluded that plan optimisation techniques can have a larger influence on the resulting dose than differences due to particular treatment machines and delivery techniques used. Considering that the intermediate and high dose regions are of highest concern for the risk of induction of second cancers, this aspect should be kept in mind when contemporary delivery techniques are applied.

Acknowledgements

This work was funded in part by the KIRO grant from the Federal Office of Public Health (FOPH), Switzerland.

The authors would like to express their gratitude to M. Gantert, S. Khan, and G. Lutters from Canton Hospital Aarau, to S. Peters and H. Schiefer from Canton Hospital St. Gallen, to A. Joosten and R. Moeckli from Centre Hospitalier Universitaire Vaudois, Lausanne, to D. Klass and P. Pemler from City Hospital Triemli, Zurich, to A. M. MacArtain from Radiotherapie Hirslanden AG, Aarau, to A. Mack and P. Nobis from Radiotherapie Hirslanden AG, Zurich, and to S. Lang and J. Hrbacek from University Hospital, Zurich, for helping and giving the opportunity to perform the measurements at their institutions.

5.A Organ and Effective Doses

Lists of average organ doses and effective doses for the whole course of treatment. The effective doses were calculated according to ICRP Report No. 103 [26] without the dose from measurement points inside the beam ports. The doses measured inside the beam ports were outside of the scope of the linear no threshold model. The photon beams had a nominal energy of 6 MV and static MLCs were used for the CyberKnife and the Elekta and Siemens linear accelerators, whereas dynamic MLCs were used for the TomoTherapy and the Varian linear accelerators (except for the 3DCRT irradiation) (see Tables 5.4–5.7).

Organ	Accuray TomoTherapy mGy	Elekta IMRT mGy	Siemens IMRT mGy	Varian IMRT mGy
Bladder	49600	46900	48200	47300
Bone	3200	3940	3390	2950
Brain and CNS	27	48.9	74.7	55.5
Colon	2850	3890	3660	1470
Female breast	37.5	49.1	82.9	47.5
Heart	38.6	48.9	72.6	49.7
Kidney	93.7	95.1	134	136
Liver	72.8	75.1	116	103
Lung	36.1	48.3	78.4	47.1
Mouth and pharynx	12.7	37.3	61.2	33.4
Oesophagus	30.7	44.7	71.4	43.3
Rectum	39800	32000	35500	39100
Remainder	13900	14900	13300	13600
Salivary gland	13	37.4	63	32.7
Skin	2130	4380	1000	4080
Small intestine	3140	6860	4420	1790
Stomach	50.7	57.7	87.2	67.8
Thyroid	17.5	38.6	62.7	34.6

Table 5.4: Intensity-modulated radiation therapy: Mean organ doses in mGy for the total treatment dose of the complete course of treatment (50.6 Gy).

Organ	Siemens hard wedge mGy	Varian 3DCRT mGy
Bladder	50800	49500
Bone	3240	3720
Brain and CNS	117	29.5
Colon	1300	2190
Female breast	113	22.7
Heart	109	24.1
Kidney	220	79.1
Liver	179	58.5
Lung	120	22.6
Mouth and pharynx	94.7	15.9
Oesophagus	110	21.9
Rectum	43600	41100
Remainder	14300	15300
Salivary gland	92.2	16.2
Skin	3590	4850
Small intestine	1640	2240
Stomach	138	34.4
Thyroid	105	14.8

Table 5.5: 3D-conformal treatment technique, with and without hard wedges: Mean organ doses in mGy for the total treatment dose of the complete course of treatment (52.0 Gy).

Organ	Accuray CyberKnife mGy	Varian VMAT mGy	Varian VMAT FFF mGy
Bladder	17100	46900	47500
Bone	1300	2910	2770
Brain and CNS	59.3	38.8	29.7
Colon	1200	1150	1260
Female breast	85.6	33.4	27.4
Heart	68.1	35.7	33.2
Kidney	68.7	94.2	106
Liver	70.7	76.6	83.1
Lung	66.9	32.9	29.7
Mouth and pharynx	73.2	27.4	12.3
Oesophagus	58.8	30	26.4
Rectum	13600	34200	40900
Remainder	4800	13000	12700
Salivary gland	72	27.4	12.6
Skin	1300	1990	939
Small intestine	3700	1590	1680
Stomach	62.3	50	53.5
Thyroid	73.6	25.1	14.4

Table 5.6: Volumetric modulated arc therapies with and without flattening filter and stereotactic CyberKnife: Mean organ doses in mGy for the total treatment dose of the complete course of treatment (VMAT: 50.6 Gy, CyberKnife: 29.0 Gy).

Treatment technique	Effective dose mSv
Accuray CyberKnife	180
Accuray TomoTherapy	116
Elekta IMRT	134
Siemens hard wedge	207
Siemens IMRT	163
Varian 3DCRT	101
Varian IMRT	133
Varian VMAT	110
Varian VMAT FFF	122

Table 5.7: Effective doses for the whole course of treatment, calculated without the dose from measurement points inside the beam ports for all therapy modalities investigated, given in mSv.

5.B Planning Guideline

Project:	Impact of IGRT/neutron radiation on secondary cancer incidence
Project Team:	Roger A. Hälg, Contact: rhaelg@phys.ethz.ch Jürgen Besserer and Professor Dr. Uwe Schneider
Participating Institutes:	Canton Hospital Aarau Canton Hospital St. Gallen Centre Hospitalier Universitaire Vaudois, Lausanne City Hospital Triemli, Zurich Massachusetts General Hospital, Boston Paul Scherrer Institut, Villigen Radiotherapie Hirslanden AG University Hospital Zurich

Alderson Phantom Irradiation: Simulation of rhabdomyosarcoma of the prostate

IMRT-treatment planning: prepare two plans with "low" and "high" (> 10 MV) photon energy (TomoTherapy only one plan) or one plan with protons, respectively. Number of fields variable. No planning-CT scan is performed prior to the delivery of the plan.

5.B.1 Basic Planning Data for Import in Your TPS

Alderson CT-data set is provided in DICOM format on CD, including structures (needed for planning). Please import data into your TPS.

5.B.2 Volumes

Volumes are already defined in the structure set. Planning-volumes are:

PTV2	PTV1_IMRT	Bladder
Femoral head l	Femoral head r	Rectum

Please do not consider other drawn volumes for optimisation.

5.B.3 Dose Constraints for Target and Critical Structures

IMRT dose optimisation should be performed considering the following dose constraints. An integrated boost concept is used.

Dose prescription:

Boost volume:	$D_2 = 23 \cdot 2.2\,\text{Gy} = 50.6\,\text{Gy}$ (TPS dose specification)
Low dose volume:	$D_1 = 23 \cdot 1.7\,\text{Gy} = 39.1\,\text{Gy}$

Target volumes:

PTV2:	98 % of volume should receive 95 % of D_2 (48.1 Gy)
	Maximum dose $< 54.1\,\text{Gy}$
PTV1_IMRT:	98 % of volume should receive 95 % of D_1 (37.1 Gy)

Risk volumes:

Bladder:	2 % of volume should receive no more than 50 Gy
Femoral head l:	50 % of volume should receive no more than 10 Gy
	2 % of volume should receive no more than 25 Gy
Femoral head r:	50 % of volume should receive no more than 10 Gy
	2 % of volume should receive no more than 25 Gy
Rectum:	50 % of volume should receive no more than 40 Gy
	20 % of volume should receive no more than 50 Gy

5.B.4 Imaging

IGRT imaging should be planned for the Alderson phantom:

Plan "low"-energy:	two setup fields (kV or MV images)
Plan "high"-energy:	CBCT (kV or MV)
TomoTherapy:	MV-CT

5.B.5 Beam Delivery

The Alderson phantom is brought to your institution. The irradiation is performed by a person of your institution (machine handling) and a member of the project team. Two separate appointments (one for each energy) are needed (only one appointment for TomoTherapy).

The Alderson phantom is irradiated twice for the "low"-energy treatment plan and three times for the "high"-energy treatment plan. Imaging dose, therapy dose, and neutron dose (twice) is measured separately. Between two measurements, approximately one hour is needed in order to prepare the phantom (new set of TLDs/PADC detectors must be placed in the Alderson phantom). The phantom is positioned relative to the laser system in the treatment room. The timetable for TomoTherapy is the same as for the "low"-energy plan.

First appointment Plan "low"-energy	**Second appointment** Plan "high"-energy
Imaging: TLD-Set 1	Imaging: TLD-Set 1
Phantom preparation	Phantom preparation
Therapy: TLD-Set 2	Neutrons: PADC Set 1
	Phantom preparation
	Neutrons: PADC Set 2

5.B.6 CT-Calibration Curve

We would like to inform you that you can use the default CT-calibration of your planning system, since the dose error which is introduced by a different calibration curve is negligible in the context of the KIRO project measurements. However, if you would like to consider the right calibration curve from CT-Hounsfield-values to electron density and mass density, you can find the calibrations for electron-density in Figure 5.10) and mass-density in Figure 5.11.

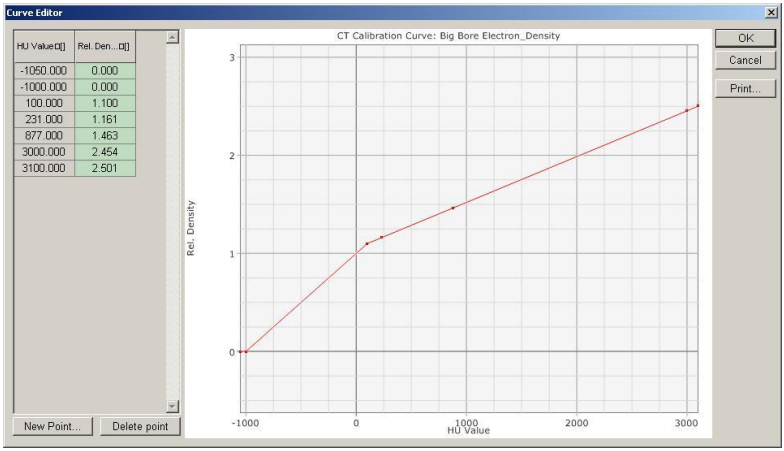

Figure 5.10: CT-calibration curve: electron density.

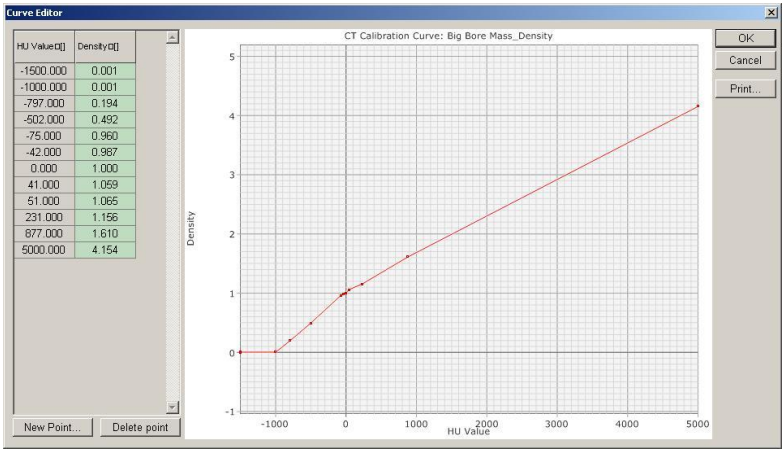

Figure 5.11: CT-calibration curve: mass density.

5.B.7 Origin of the CT Data-Set

The Alderson phantom is optically marked on it's surface (white markers on phantom highlighted by red circles on Fig. 5.12) to adjust it relatively to your laser system (no fiducial markers which are visible in the CT were used). The origin of the CT-system corresponds to this marking. Unfortunately, the CT-data-origin is probably not correctly imported during the DICOM-RT import procedure into your system. It is important that you set the CT-origin according to the images in Figures 5.13 and 5.14. The green cross marks the CT-origin in the screen shots.

If for any reason for future measurements the Alderson phantom cannot be positioned using a Laser system, please get in touch with us.

Figure 5.12: Markers for the laser system on the Alderson phantom.

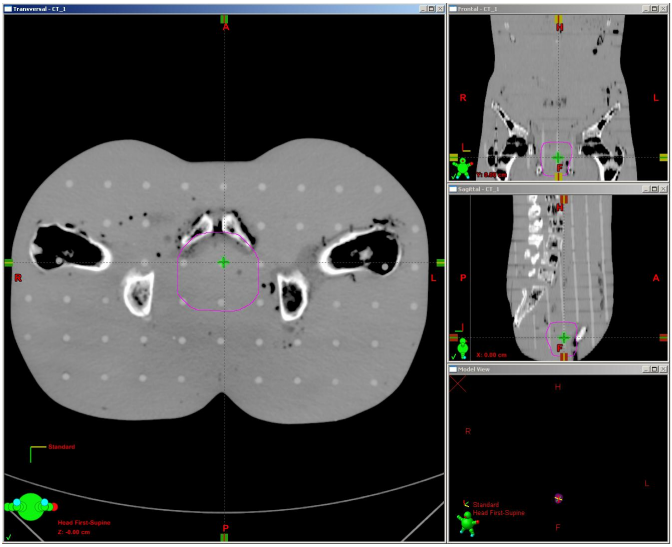

Figure 5.13: Screen shot for the position of the isocenter in the CT data-set.

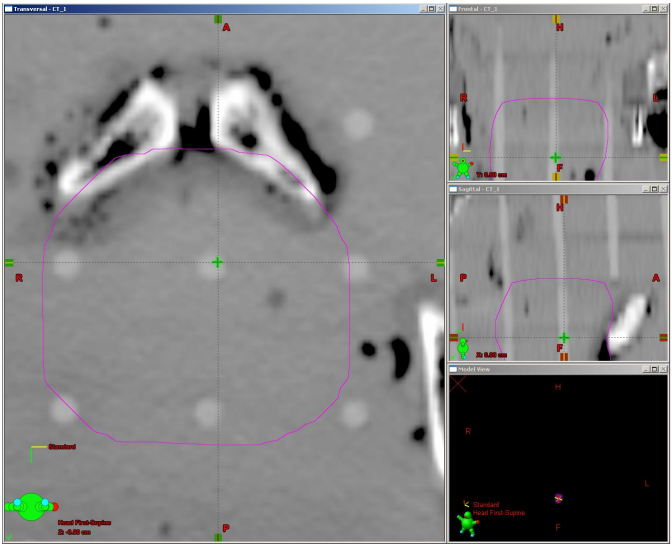

Figure 5.14: Zoomed in screen shot for the position of the isocenter in the CT data-set.

Chapter 6

Systematic Measurements of Whole-Body Imaging Dose Distributions in Image-Guided Radiation Therapy

Roger A. Hälg[1], Jürgen Besserer[1], and Uwe Schneider[1,2]

[1] Institute for Radiotherapy, Radiotherapie Hirslanden AG, Aarau, Switzerland

[2] Vetsuisse Faculty, University of Zurich, Zurich, Switzerland

Submitted to
Medical Physics
2012

6.1 Introduction

New treatment modalities and further optimised delivery techniques in radiation therapy are increasing the precision at which the radiation dose can be applied to a cancer patient. Two examples are the introduction and application of intensity-modulated radiation therapy (IMRT) and volumetric modulated arc therapy (VMAT). These modern radiotherapy treatment techniques suggest an increase in cancer cure rates while simultaneously unwanted side effects can be reduced [84]. However, the full benefit of these improvements can only be exploited if the accuracy of the positioning of the target volume is guaranteed and the magnitude of external and internal motion of the patient is minimised. Therefore, more and more imaging modalities are used in the process of the patient setup to verify the correct position of the target structures before and eventually during the treatment. Additional imaging devices are mounted on the gantry or installed in the treatment room for these purposes. Image-guided radiation therapy (IGRT) is defined as the combination of imaging procedures in the treatment room and contemporary irradiation techniques. Common imaging procedures for IGRT are cone beam computed tomography (CBCT), kilovoltage planar imaging, stereoscopic imaging, and portal imaging. An extensive list of imaging modalities used in IGRT can be found in the report of the AAPM Task Group 75 [96]. The improved accuracy in patient positioning, however, results in additional dose contributions to the integral patient dose. Like the concomitant dose produced by linear accelerator head leakage and stray dose, imaging dose contributes to the dose burden inside and outside the treatment area [97]. It has been shown that more imaging procedures have been introduced to the treatment process over the past years [37] and as a direct consequence, the concomitant dose has been increasing steadily. It is expected that the usage of imaging procedures will grow further, as modern delivery techniques like IMRT are introduced to clinical routine. In addition, the concept of adaptive radiotherapy (ART) [98] is discussed, as the availability of precise imaging modalities and deformable image registration is continuously increasing and the time needed by treatment planning systems to calculate the dose distribution of a treatment plan is decreasing [99]. The amount of exposure from imaging techniques to a patient during the whole course of treatment in radiotherapy can include multiple CT scans for treatment planning and replanning, fluoroscopic procedures to estimate organ motion, and a series of inter- and intrafraction images or CT scans using gantry-mounted devices for target verification. These

additional doses from imaging procedures are in most cases only qualitatively monitored, if at all. This raises concerns for two reasons. Firstly any additional dose to the patient increases the risk of radiation-induced stochastic effects, in particular for younger patients. Secondly in the context of dose escalation, the dose from imaging procedures could cause or increase the severity of side effects from the cancer therapy treatment. It is therefore essential to have tools to assess the cost and benefit of all doses involved in image-guided radiation therapy, as the assumption that the cumulative imaging dose is negligible compared to the therapeutic dose, is not true anymore in general with the application of IGRT. To perform risk analysis of radiation induced malignancies, it is important to assess the complete dose distribution received by a radiotherapy patient, such as the primary dose distribution, stray dose, and imaging dose as well as possible secondary neutron dose contributions. Advances in cancer therapy over the last few decades have resulted in longer survival times after treatment, which gives the necessity to investigate the influence of the integral dose in terms of the long term health of cancer patients [7]. This includes investigations on secondary cancer incidence.

To determine the imaging dose to organs at risk, measurements or Monte Carlo simulations are necessary. There are several studies in the literature, where imaging doses were measured and simulated [97, 100–102]. Most studies focus on the imaging dose from CBCT procedures. Comparative measurements were usually performed on single devices or for devices installed at a specific linear accelerator. Direct comparisons between different dosimetry studies are difficult, because the measurement conditions and imaging intentions differ substantially.

The aim of this study was to measure absorbed dose from various imaging modalities in an anthropomorphic phantom using the same measurement setup and imaging intention. The doses from typical imaging procedures involved in an IGRT treatment of a cancer patient were measured. The doses were determined with respect to geometrical and anatomical considerations. The experimental setup, including the locations of the measurement positions, was exactly the same as in a preceding study of radiotherapy stray dose measurements. This allows a direct combination of imaging dose distributions with the therapy dose distribution.

6.2 Materials and Methods

6.2.1 Treatment and Imaging Intention

The clinical treatment intention of this study was the curative irradiation of a rhabdomyosarcoma of the prostate for an adolescent patient, represented by an anthropomorphic phantom. Therefore all imaging procedures were configured to reproduce the pelvic region of the phantom. The participating institutions were advised to choose the imaging protocol and the device parameters as they would for a real patient with the same treatment intention at their institution. The planning CT and the contouring of the target structures and organs were performed at one institution. All measurements and detector readouts were performed by the same person. This procedure ensured the consistency of the measurements at the different sites.

6.2.2 Imaging Modalities

The series of measurements in this study consisted of several imaging irradiations. The imaging modalities in conjunction with treatment machines from the manufacturers Accuray (Accuray, Sunnyvale, CA, USA), Elekta (Elekta AB, Stockholm, Sweden), Siemens (Siemens AG, Healthcare Sector, Erlangen, Germany), and Varian (Varian Medical Systems, Palo Alto, CA, USA) were investigated. The gantry- or room-mounted devices used for imaging were the Target Locating System from Accuray, the X-ray Volume Imager (XVI) from Elekta, the On-Board Imager (OBI), and the TrueBeam X-Ray Imaging System (XI) from Varian. The imaging techniques investigated on these treatment machines were kilo- and megavoltage cone beam computed tomography, megavoltage fan beam computed tomography, kilovoltage planar imaging, stereoscopic kilovoltage imaging, and megavoltage portal imaging. Further measurements were performed using a GE LightSpeed RT 16 CT scanner (GE Healthcare, Little Chalfont, UK), including dose measurements of a 3D planning CT (3DCT) and a time-resolved planning CT (4DCT) for respiratory gating. On another CT scanner (GE HiSpeed DX/i CT Scanner), the imaging dose resulting from kilovoltage scout views was determined. The different measurements were performed at the Canton Hospital Aarau, Aarau, Switzerland (Siemens Oncor Avant-Garde), Canton Hospital St. Gallen, St. Gallen, Switzerland (Elekta Synergy with XVI), Centre Hospitalier Universitaire Vaudois, Lausanne, Switzerland (Accuray TomoTherapy), Paul Scherrer

Imaging device	Investigated imaging technique
Accuray CyberKnife	Stereoscopic kV planar images
Accuray TomoTherapy	MV fan beam CT
Elekta Synergy	MV portal images
Elekta XVI	kV CBCT
GE LightSpeed RT 16	kV fan beam CT, 3D and 4D
GE HiSpeed DX/i	CT scout views
Siemens Oncor Avant-Garde	MV CBCT and portal images
Varian Clinac 21 iX	MV portal images
Varian OBI	kV CBCT and planar images
Varian TrueBeam XI	kV CBCT

Table 6.1: Imaging devices used and the corresponding imaging techniques measured in this study. The machine parameters and settings for each imaging modality can be found in Appendix 6.B.

Institut, Villigen, Switzerland (GE HiSpeed DX/i CT Scanner), Radiotherapie Hirslanden AG, Aarau, Switzerland (GE LightSpeed RT 16 CT scanner and Varian Clinac 21 iX with OBI), Radiotherapie Hirslanden AG, Zurich, Switzerland (Accuray CyberKnife with Target Locating System), and University Hospital Zurich, Zurich, Switzerland (Varian TrueBeam with XI). An overview of all imaging devices involved and the corresponding investigated imaging techniques is given in Table 6.1.

6.2.3 Phantom and Detectors

In order to asses and evaluate the imaging dose and to account for the patient anatomy, an anthropomorphic Alderson-Rando phantom (RSD Radiology Support Devices, Long Beach, CA, USA) was used. The phantom consisted of 35 transversal slabs, made of material that was tissue equivalent for photon beams and every slab contained holes for detectors. The dose measurements were performed using thermoluminescent dosimeters (TLDs) placed inside the Alderson-Rando phantom. The dosimeters had the form of disks with a diameter of 4.50 mm and a thickness of 0.60 mm. This geometry allowed to position the detectors directly in the phantom slabs without casing. The trading name of the detectors was TLD-100H (Thermo Fisher Scientific, Waltham, MA, USA) and they were made of lithium fluoride ($\sim 7.5\,\%$ ^{6}Li) and doped with magnesium, copper, and phosphorus (LiF:Mg,Cu,P). The useful dose range of the dosimeters was 1 µGy to 20 Gy according to the manufacturer. The positions of the detectors were chosen to determine the dose profile along the medial patient axis from the target (in the prostate) to the head and to assess the

dose in different organs. The radiation sensitive organs were determined according to the ICRP recommendations [26]. A total of 184 measurement positions were selected in the phantom, facilitating the determination of a three-dimensional dose distribution. The doses were determined in terms of absorbed dose to water.

6.2.4 Detector Calibration

The dosimeters were calibrated using the 6 MV beam of a Varian Clinac 21 iX and a RW3 solid water slab phantom (PTW, Freiburg, Germany). Measurements in a water tank were used to find a combination of field size and depth in the phantom which gave a dose profile as flat as possible (field size: $25 \times 25\,\mathrm{cm}^2$, depth: 14.7 cm, dose variation: ±0.5 %). The measurement TLDs were irradiated inside the primary field in batches of 50 detectors with a dose of about 22 mGy. The batches were placed in the solid water phantom inside a PMMA casing. The calibration dose was determined by ionisation chamber measurements (Farmer Ionization Chamber, PTW, Freiburg, Germany) at the position of the PMMA casing. One batch of 16 TLDs was used for the evaluation of the background/transport signal. They were calibrated in the same way as the measurement dosimeters, but were not irradiated intentionally during an imaging measurement. Each detector batch contained four reference dosimeters, which were irradiated with a reference dose (∼ 22 mGy) for each measurement.

For each TLD, a calibration factor in terms of dose per reader count was determined by performing a calibration measurement two to three days before every measurement. These dose calibration factors (DCF) were determined using Equation (6.1),

$$k^i_{\mathrm{cal,raw}} = \frac{d_{\mathrm{cal}}}{C^i_{\mathrm{cal,raw}}}, \tag{6.1}$$

where $k^i_{\mathrm{cal,raw}}$ was the raw DCF of the i^{th} TLD, d_{cal} was the calibration dose determined by the ionisation chamber measurement, and $C^i_{\mathrm{cal,raw}}$ was the raw number of counts from the detector readout.

The reader counts were then corrected for the background signal according to Equation (6.2) considering the sensitivity variation between the background dosimeters and the dosimeter of interest

$$C^i_{\mathrm{cal}} = C^i_{\mathrm{cal,raw}} - \frac{k^i_{\mathrm{cal,raw}}}{k^{\mathrm{B}}_{\mathrm{cal,raw}}} \cdot C_{\mathrm{B}}, \tag{6.2}$$

where C^{i}_{cal} were the corrected reader counts of the i^{th} TLD for the calibration measurement, $k^{\mathrm{B}}_{\mathrm{cal,raw}}$ was the mean raw dose calibration factor of all the background dosimeters, and C_{B} were the mean reader counts of all the background dosimeters from the corresponding measurement irradiation.

These corrected counts C^{i}_{cal} were used in Equation (6.1) instead of the raw reader counts $C^{i}_{\mathrm{cal,raw}}$ to determine the final dose calibration factor (k^{i}_{cal}) for each dosimeter and calibration.

A microprocessor-controlled annealing procedure in a dedicated oven (Fimel ETT Annealing Oven, PTW, Freiburg, Germany) was applied to all the TLDs after each readout. They were placed in a metallic container, in the same batches as for calibration. A linear heating ramp ($\sim 35\,^{\circ}\mathrm{C\,min^{-1}}$) up to 240 °C was used. The TLDs were kept at this maximum temperature for 10 min before they were cooled down in the oven to 50 °C with a constant cooling rate ($\sim 5\,^{\circ}\mathrm{C\,min^{-1}}$).

6.2.5 Detector Readout

For the readout of the dosimeters, a Fimel PCL3 isothermal TLD reader (PTW, Freiburg, Germany) was used. This reader had two isothermal heating zones, one for preheating and one for the actual readout of the dosimeters. The preheating and readout temperatures were 100 °C and 240 °C, respectively. Each TLD was placed in a metallic cupel for the automated readout procedure. The same batches for the calibration were used to load the stack of the reader. The signal of the dosimeters was determined in terms of collected photomultiplier charge for 30 s during the readout of the TLDs.

Manufacturer recommended optical filters were available for the TLD reader to adapt the dynamic range of the photomultiplier to the light signal of the TLDs and, therefore, to the measured dose. A blue filter with the smallest available light absorption was applied to the readout of all the TLD batches to maximise the lowest measurable dose.

The reference dosimeters of each batch were used to correct for the daily variation in the output of the TLD reader and to account for a possible drift in the output during one readout cycle. Therefore, two of the four reference dosimeters were read out at the beginning of the batch and two at the end. The values of the dose per count from the reference irradiation relative to the values from the corresponding calibration were used to calculate the sensitivity of the readout at the beginning and at the end of the readout cycle. A linear interpolation between these two values

(k_{drift}) was used to correct the readout of the TLDs used for measurement in that batch. The mean correction factor for the daily variation was 1.00 and the maximum correction was 4 %. The drift correction k_{drift} during the readout of one batch had a mean value of 2 % and a maximum of 7 % over all measurements.

6.2.6 Dose Determination

The measured dose of each dosimeter was calculated by means of Equation (6.3), where the above mentioned calibration and correction factors were applied and the background signal was subtracted

$$D^i = \left(k^i_{\text{cal}} \cdot C^i - k^{\text{B}}_{\text{cal}} \cdot C_{\text{B}}\right) \cdot k^i_{\text{drift}}, \tag{6.3}$$

where D^i was the determined absorbed dose to water of the i^{th} TLD, k^i_{cal} and $k^{\text{B}}_{\text{cal}}$ were the background corrected DCF from the corresponding calibration, C^i were the reader counts from the measurement, and k^i_{drift} was the linear interpolation of the drift correction for the i^{th} readout position in the cycle.

6.2.7 Energy Correction

The readout signal of thermoluminescent dosimeters depends on the energy of the impinging photons. Therefore, the measured dose depends on the photon spectrum at the measurement position. For measurements of photon dose from radiotherapy or imaging procedures, this could lead to differences in the measured dose depending on the position of the measurement in the phantom and of the radiation source. The energy dependent response of the thermoluminescent material used in this study (LiF:Mg,Cu,P) was investigated by several groups [86–89]. Monte Carlo simulations of photon spectra for kilovoltage photon beams produced by gantry-mounted imaging devices were performed by Ding et al. [103] and Ding and Coffey [104] for the Varian OBI and by Downes et al. [105] for the Elekta XVI.

In order to analyse the impact of the difference of the energy spectrum used for calibration and the spectra of the imaging modality on the dose measurements in this study, the estimated detector response relative to the calibration response was calculated. The photon spectra simulated by Ding et al. [103] for different peak energies were used. The energy response curve of LiF:Mg,Cu,P thermoluminescent material measured by

Edwards et al. [88] in quasi monoenergetic low energy photon beams was convolved with these photon spectra. A reduction of the TLD response by 1 %, 5 %, 9 %, 9 %, 12 %, and 11 % relative to the calibration response in the 6 MV photon beam was calculated for spectra with peak energies of 80 kV, 100 kV, 120 kV, 125 kV, 125 kV with half bow tie filter, and 125 kV with full bow tie filter, respectively. It was therefore decided to use a correction factor for the energy dependent response of the TLDs of 1.0 for the imaging procedure using a peak energy of 75 kV (Varian kV planar AP), a correction factor of 1.05 for the peak energies 100 kV and 110 kV (Varian CBCT high-quality head and Varian CBCT low-dose thorax), and a correction factor of 1.1 for the higher beam energies in the kV range. The energy dependent response correction factor for MV photon beams was determined in another study by Hälg et al. [81] (chapter 5 of this thesis) where the stray dose from radiation therapy treatments was measured using the same thermoluminescent material. For the in-field measurements, no correction was needed and for the measurement positions outside of the treated volume, a correction factor of 1.1 was determined. The obtained correction was adapted in this study for the imaging measurements using megavoltage photon beams and for the calibration of the detectors.

6.2.8 Angle Correction

The angular dependency of the TLD readout signal was investigated by Dong et al. [106] for photon beams in the imaging energy regime. They found a maximal reduction of about 10 % in the response for an irradiation angle of 90°. For angles below 60°, the reduction in the response was below 5 %. It was therefore decided to use a correction factor of 1.1 for all the imaging modalities using kilovoltage photon beams inside the treated volume, where the irradiation source has an angle of about 90° towards the orientation of the TLDs in the phantom. No correction was applied for the measurement positions outside of the treated volume, as the main contribution to the dose was from phantom scatter, which had a clearly smaller angle of incidence than 60° relative to the TLD orientation. For the imaging procedures using megavoltage beams, no correction for the angular dependency of the TLD response was applied.

6.2.9 Dose Linearity

The linearity of the dose response of the TLD readout signal was checked with a randomly selected subset of the dosimeters within the primary

beam of the Varian Clinac 21 iX. A least-squares fit to the measured doses over the whole dose range of this study (250 µGy–0.5 Gy) showed a slope of 1.04 ionisation chamber dose/TLD dose and an intercept of −0.21 mGy ionisation chamber dose, with a corresponding R^2 of 0.9999. The quality of the fit indicated a linear behaviour of the TLD signal with dose and, therefore, no correction for non-linearity was applied.

6.2.10 Measurement Reproducibility

In order to investigate the long term stability of the TLD readout and to estimate the reproducibility of the dose measurements, the readout signal per applied dose of the reference TLDs was analysed for all the calibration and reference irradiations. The reproducibility of a complete imaging measurement was checked by repeating the measurement of the CBCT pelvis spot light protocol using the Varian OBI and by comparing the determined dose for every measurement position.

6.3 Results

The reproducibility of the dose measurement was determined from repeated measurements with the reference dosimeters. The readout signal per applied dose was determined for all the calibration and reference irradiations. The standard deviation was calculated for each of the 20 reference TLDs for a total of 47 irradiations. The mean standard deviation of all the reference TLDs was 5 % with minimum and maximum of 2 % and 9 %, respectively. In Figure 6.1, the distribution of the readout signal per applied dose normalised to the mean value of each TLD, is shown in a box-and-whisker plot for the 20 reference TLDs.

To investigate the reproducibility of a complete imaging measurement, the measurement for the CBCT using the pelvis spot light protocol on the Varian OBI was repeated. The mean value of the relative doses and the standard deviation were 0.97 ±0.05.

The dose from the different imaging modalities was measured on the medial patient axis with 34 detectors spaced by 2.5 cm. The following figures show this dose profile from the isocenter in the prostate ($x = 0$ cm) up to the head ($x = 82.5$ cm) for different imaging procedures.

Figure 6.2 shows a semi-logarithmic comparison of the imaging dose per scan along the medial patient axis for different CBCT protocols on the Varian OBI device. The protocols pelvis, pelvis spot light, low-dose

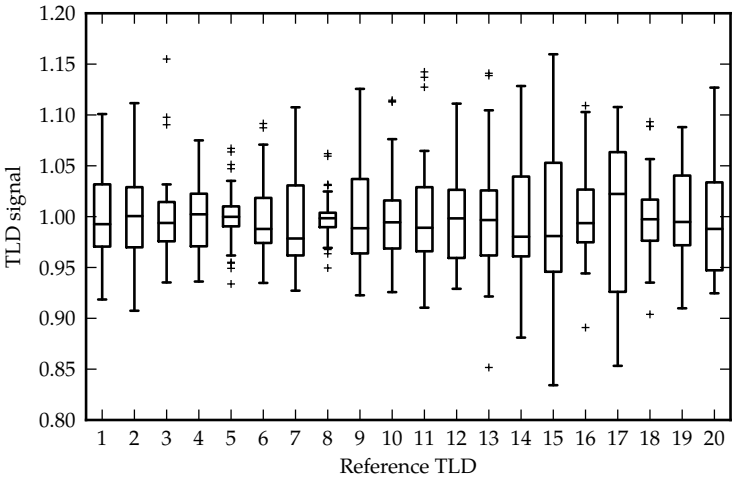

Figure 6.1: Reproducibility of the 20 reference TLDs for all the calibration and reference irradiations (47 in total). The TLD signal per dose normalised to the mean value of each TLD is shown in a box-and-whisker plot.

thorax, and high-quality head were measured, respectively. Although these protocols were intended to image different anatomical regions, the scans were applied to the target structure in the prostate to compare the dose for the different settings. On the left, the absorbed dose is shown per CBCT scan. On the right, the dose is plotted relative to the dose of the pelvis protocol.

The dose on the medial patient axis from different computed tomography imaging devices from the linear accelerator manufacturers Elekta, Siemens, and Varian and from a TomoTherapy unit are shown in Figure 6.3. On the left-hand side, the absorbed dose is plotted per scan for the pelvis protocols. For the Elekta and Varian (Clinac 21 iX and TrueBeam) linear accelerators, the beams for the scan were produced by additional imaging devices mounted on the gantry and used kilovoltage photon beams. The Siemens linear accelerator used the 6 MV therapy beam to acquire the CBCT, whereas the TomoTherapy unit used the megavoltage therapy photon beam with reduced energy for the fan beam imaging procedure. To correct for a systematic misalignment of the isocenter on the Elekta linear accelerator during the measurement, this curve was shifted by -0.5 cm. The relative dose distribution compared to the Varian

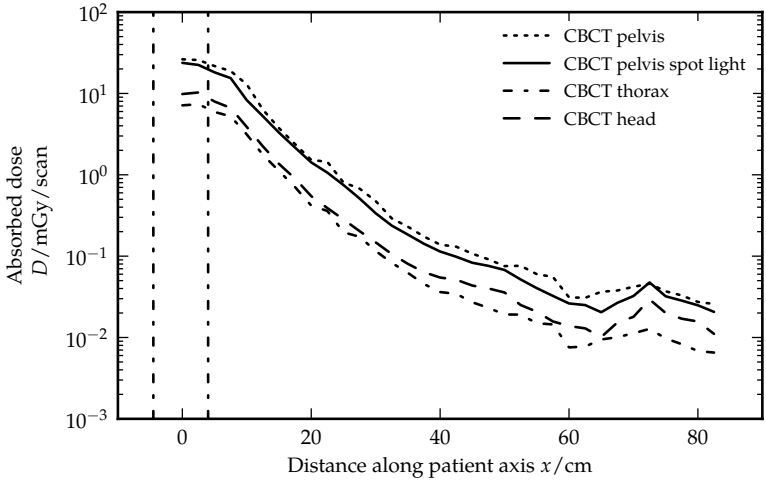

(a) Varian CBCT protocols

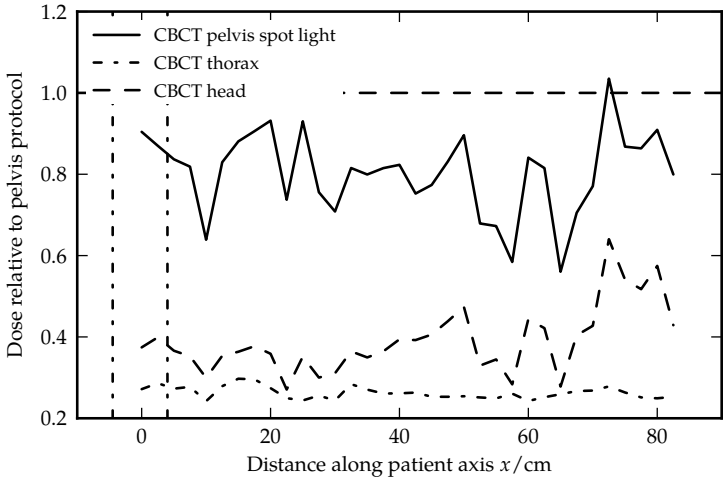

(b) Varian CBCT protocols relative

Figure 6.2: Dose distribution along the medial patient axis. The isocenter corresponds to $x = 0$ cm and the vertical lines represent the border of the target volume along this axis. (a) Imaging dose per scan for the CBCT protocols pelvis, pelvis spot light, low-dose thorax, and high-quality head on the Varian OBI applied to the same anatomical region. (b) Dose relative to the pelvis protocol.

CBCT is plotted on the right-hand side.

Two planning CT procedures and for comparison a CBCT procedure using a gantry-mounted device is depicted in Figure 6.4. In addition to the conventional 3D computed tomography acquisition for treatment planning purposes, a 4DCT protocol with respiratory gating was measured. The left graph shows the dose per scan and on the right-hand side, the dose is plotted relative to the dose of the CBCT procedure.

Dose measurements of planar images for patient setup are depicted in Figure 6.5. Imaging doses from the Varian On-Board Imager are shown for anterior-posterior and lateral planar acquisitions, as well as from stereoscopic images ("Live Image") used at the CyberKnife and from a combination of a frontal and a sagittal scout view of the GE HiSpeed CT scanner are given. The shown procedures all used photon beams in the kilovoltage energy range (see Appendix 6.B). For the stereoscopic Live Images at the CyberKnife, the dose is given per acquisition, which corresponds to two images.

The measured dose from treatment beam verification imaging procedures is given in Figure 6.6. The verification images were acquired using portal vision detectors mounted on the gantry and the dose to the patient was measured at linear accelerators of the manufacturers Elekta, Siemens, and Varian. For the Elekta linear accelerator, images in anterior-posterior and lateral direction using both a double exposure technique were measured together. Two images at the Siemens linear accelerator in anterior-posterior and lateral direction were combined for the measurement of the imaging dose. Only one image in anterior-posterior direction was measured at the Varian treatment machine.

Each of the 184 dosimeters used for the determination of imaging dose was assigned to an organ structure in the Alderson-Rando phantom. This organ assignment was used to calculate mean organ doses. A comparison of the resulting organ doses for gantry-mounted CBCT procedures using the Varian OBI is listed in Table 6.5 of Appendix 6.A. The mean organ doses of the devices used for computed tomography for different manufacturers of treatment machines are presented in Table 6.6. In Table 6.7, the imaging doses from the planning CTs are compared in terms of the mean organ doses. The mean organ doses from planar imaging procedures using kilovoltage and megavoltage photon beams are summarised in Tables 6.8 and 6.9 of Appendix 6.A.

The effective dose resulting from all imaging procedures was calculated according to the ICRP Report No. 103 [26] and are listed as effective dose per scan or image in Table 6.2.

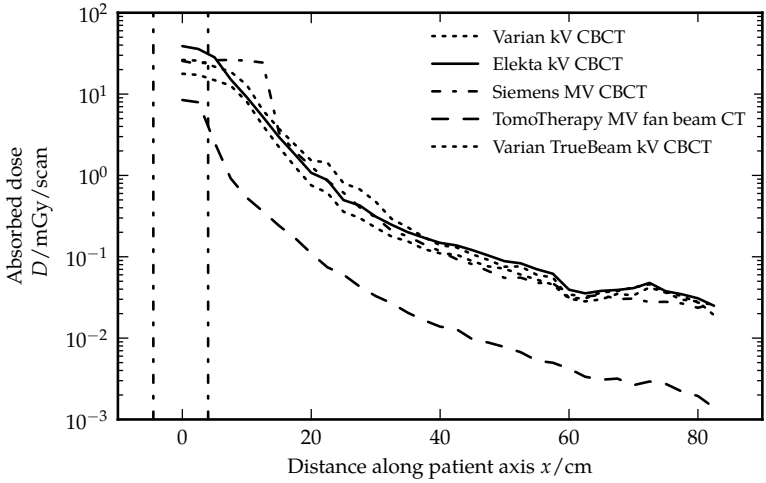

(a) Gantry-mounted CT

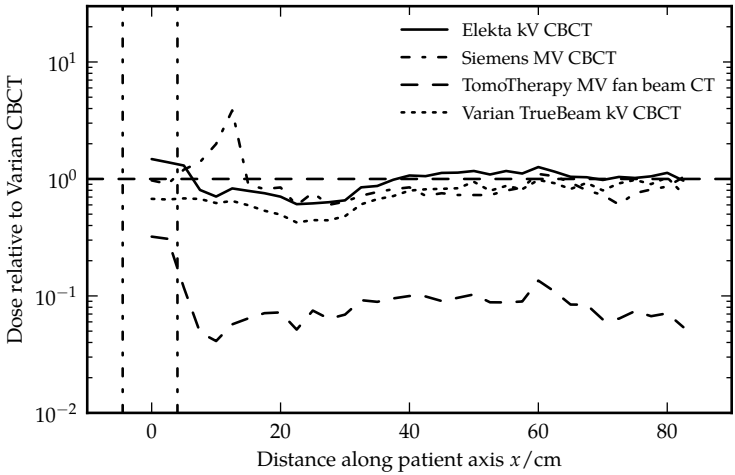

(b) Gantry-mounted CT relative

Figure 6.3: Dose distribution along the medial patient axis. The isocenter corresponds to $x = 0\,\text{cm}$ and the vertical lines represent the border of the target volume along this axis. (a) Imaging dose for different computed tomography imaging devices installed on linear accelerators using the pelvis protocols. (b)Dose relative to the Varian CBCT measurement.

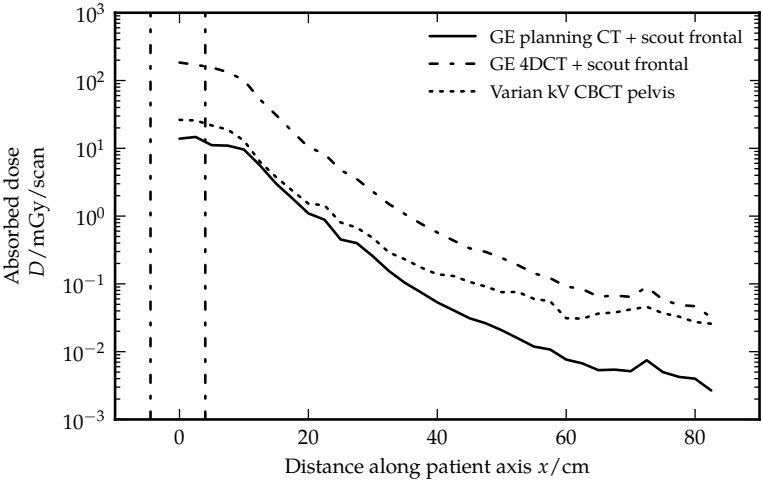

(a) Planning CT

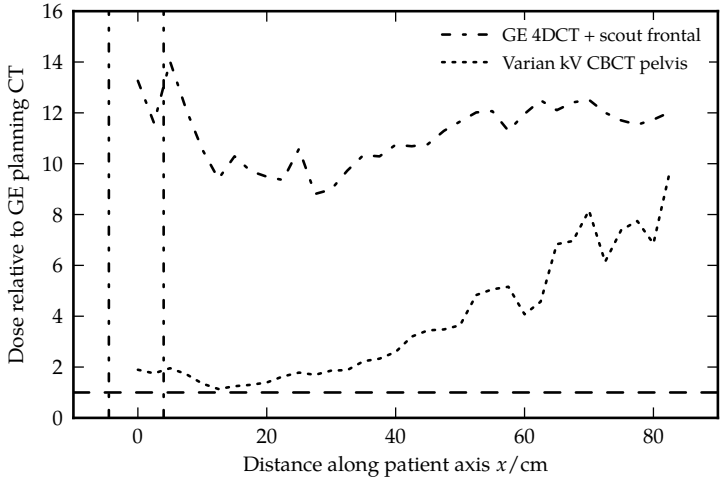

(b) Planning CT relative

Figure 6.4: Dose distribution along the medial patient axis. The isocenter corresponds to $x = 0\,\mathrm{cm}$ and the vertical lines represent the border of the target volume along this axis. (a) Imaging dose per scan of a planning CT, a time-resolved planning CT, and a Varian CBCT procedure using the pelvis protocols. (b) Imaging dose relative to the Varian CBCT dose.

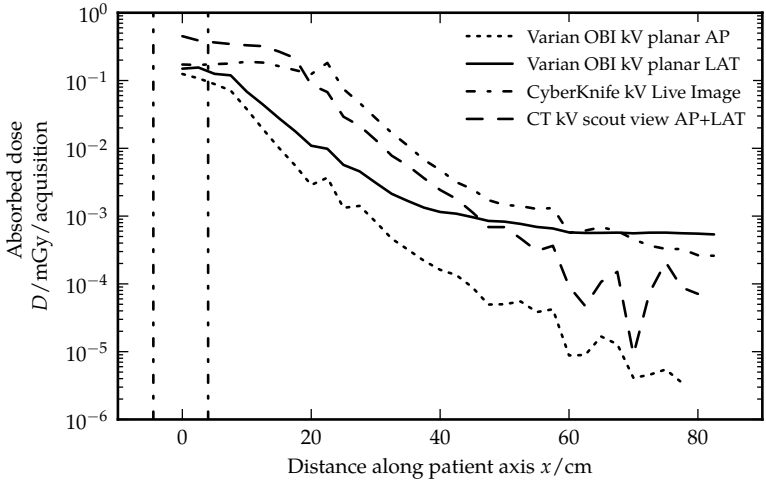

(a) Planar kV imaging

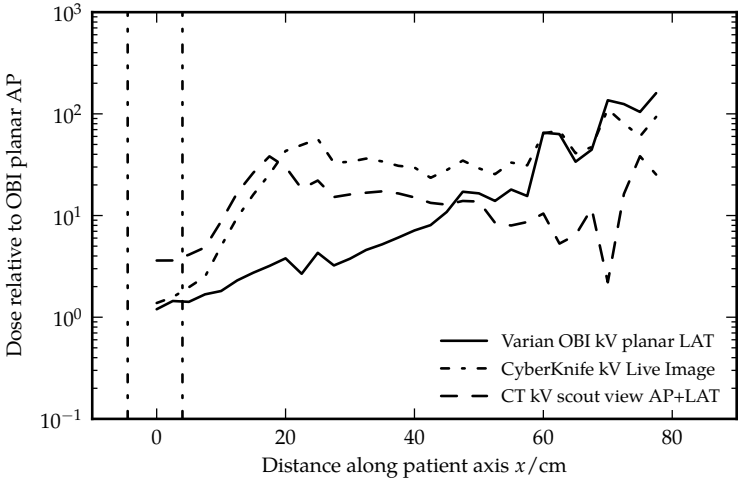

(b) Planar kV imaging relative

Figure 6.5: Dose distribution along the medial patient axis. The isocenter corresponds to $x = 0$ cm and the vertical lines represent the border of the target volume along this axis. (a) Imaging dose per image acquisition for different planar imaging devices using kV photon beams. (b) Imaging dose relative to the Varian OBI planar AP dose.

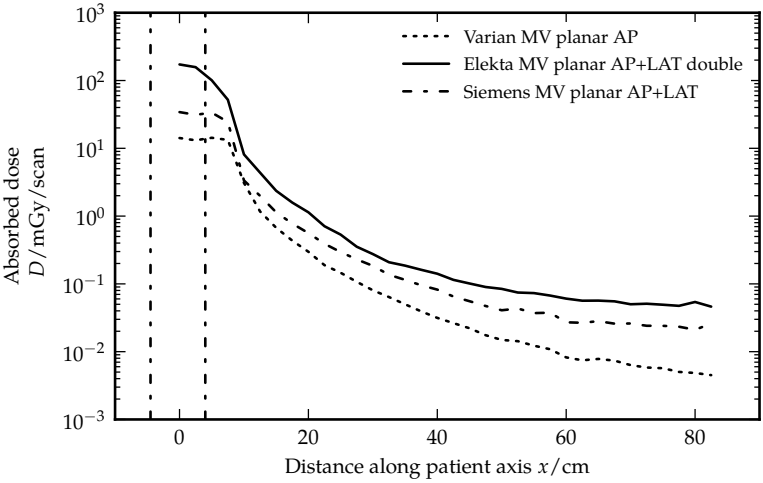

(a) Planar MV imaging

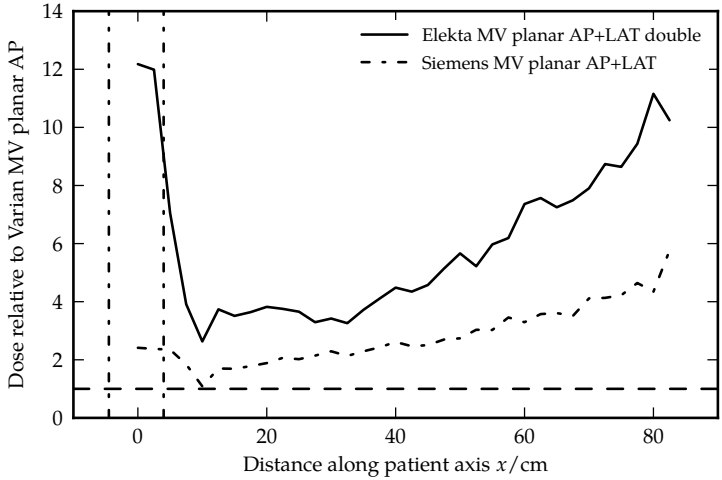

(b) Planar MV imaging relative

Figure 6.6: Dose distribution along the medial patient axis. The isocenter corresponds to $x = 0$ cm and the vertical lines represent the border of the target volume along this axis. (a) Imaging dose per image for different portal imaging devices using MV therapy photon beams. (b) Imaging dose relative to the dose of a Varian portal AP image.

Imaging procedure	Effective dose total mSv	Effective dose outside mSv
Varian kV CBCT pelvis	4.05	1.24
Varian kV CBCT pelvis spot light	4.22	1.09
Varian kV CBCT low-dose thorax	1.11	0.338
Varian kV CBCT high-quality head	1.71	0.419
Varian TrueBeam kV CBCT pelvis	2.42	0.681
Elekta kV CBCT pelvis	4.95	0.85
Siemens MV CBCT pelvis	4.63	1.98
TomoTherapy MV CT pelvis	0.801	0.0591
GE LightSpeed planning 3DCT	2.38	0.946
GE LightSpeed planning 4DCT	29.5	9.95
GE HiSpeed Scout view	0.0819	0.0481
CyberKnife kV Life Image	0.0596	0.0481
Varian kV planar AP	0.0137	0.00408
Varian kV planar LAT	0.0366	0.00922
Elekta MV portal	16.4	1.26
Siemens MV portal	4.35	0.556
Varian MV portal	1.88	0.44

Table 6.2: Effective doses per scan or image for all imaging modalities investigated, given in mSv. Second column lists the effective dose for all measurement positions and the third column the effective dose only for the measurement positions outside of the treated volume.

6.4 Discussion

The investigation on the reproducibility using the reference TLDs showed a variation for dose measurements with a mean standard deviation of 5 %. The ratio of two repeated measurements of a complete imaging procedure showed also a deviation of 5 % (standard deviation of all TLDs), which is lower than the error of the ratio of two measurements with an uncertainty of 5 % each. In addition to the statistical uncertainty, the reproducibility measurement of an imaging procedure, included also uncertainties in the positioning of the phantom. Therefore, the mean standard deviation was taken as the dose measurement uncertainty.

One of the most important questions in the discussion of IGRT is the dose induced by the applied imaging modalities. Usually the effective dose from the imaging modalities is determined and the resulting risk for the patient is estimated. In our opinion, the imaging dose should be also viewed in relation to the stray dose from therapy, which is an unavoidable consequence of the patient treatment. Therefore, the effective dose was also determined without the dose from measurement points inside the beam ports from therapy (<5 Gy), which is listed as the third column

in Table 6.2. This effective dose from imaging procedures can now be compared directly to the effective dose from the therapeutic stray dose, which was measured in another study by Hälg et al. [81] (chapter 5 of this thesis). Whole-body dose distributions for various treatment machines and delivery techniques were measured using the same treatment intention and phantom as in this study. As an example, the dose of an IMRT irradiation was compared in Figure 6.7 to a cone beam computed tomography using a pelvis protocol, a megavoltage portal AP image, and a kilovoltage planar AP image at the Varian Clinac 21 iX. The dose is plotted on the left-hand side for one scan or image of each imaging modality together with the dose of one fraction of the treatment irradiation. It is obvious that all the imaging procedures deposited in the phantom at least an order of magnitude less dose than the treatment itself. The kilovoltage cone beam computed tomography had the highest dose contribution from the imaging procedures, followed by the megavoltage portal image. The kilovoltage planar imaging procedure contributed the smallest amount of dose. The field-of-view of imaging modalities were larger than the target volume. Therefore, the additional dose relative to the therapeutic stray dose was largest close to the target volume for all imaging procedures.

The resulting effective dose from radiotherapy treatment irradiations and imaging procedures determined outside of the treated volume is listed in Tables 6.3 and 6.4. For a given treatment machine and irradiation technique, typical imaging modalities are shown with the corresponding effective dose. The effective dose for the therapeutic stray dose is given for the complete treatment course (3D-conformal treatment with and without hard wedges: $26 \times 2.0\,\mathrm{Gy}$, IMRT and VMAT: $23 \times 2.2\,\mathrm{Gy}$, CyberKnife: $5 \times 5.8\,\mathrm{Gy}$). The planning CT dose is listed for one scan per treatment course, the setup imaging dose is given for daily application and the verification imaging was assumed to be applied once per week in double exposure mode for a typical four field treatment plan. In the third column of Tables 6.3 and 6.4, the imaging dose is given in percentage of the therapeutic stray dose for a complete IGRT treatment course.

A conventional 3D planning CT resulted in an additional effective dose of less than 1 % outside of the treated volume. In our opinion, this increase in the total dose to the patient is negligible in terms of additional cancer risk. The situation was different, if gating methods were used for obtaining a CT scan. A 4D planning CT resulted in a 10 times larger dose than a 3D planning CT and thus increased the effective dose to the patient outside of the treated volume by 10 % compared to the therapeutic stray dose.

For the patient setup, several imaging modalities can be used. A daily

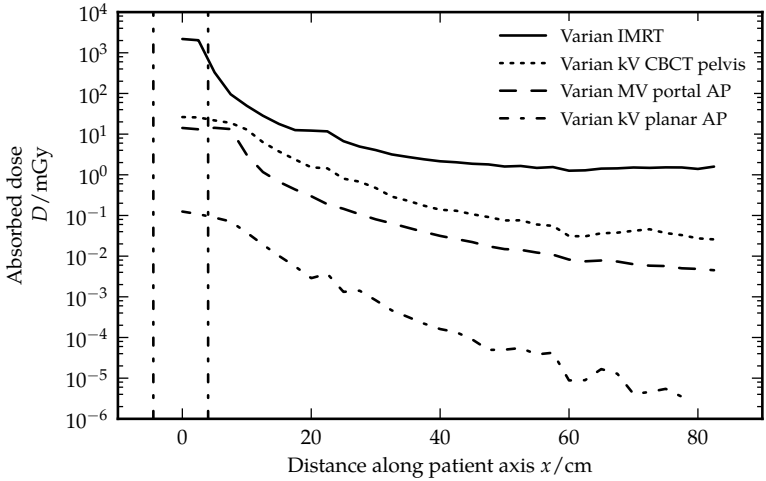

(a) Stray dose comparison therapy vs imaging

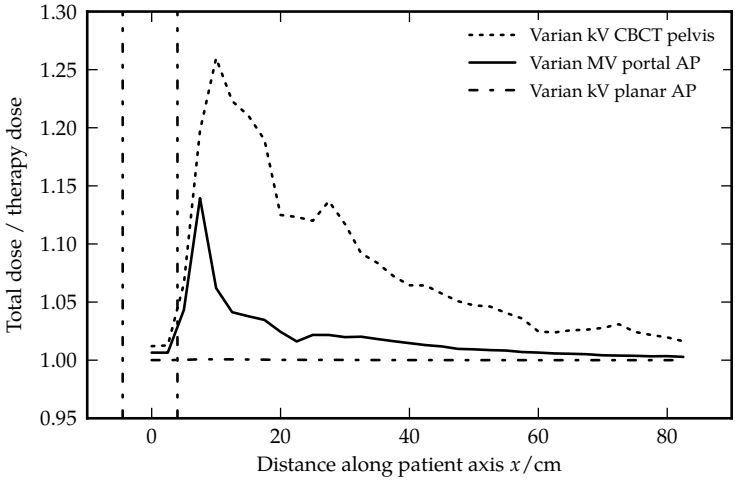

(b) Stray dose comparison therapy vs imaging relative

Figure 6.7: Comparison of the dose along the medial patient axis deposited by one scan or image of the imaging procedures CBCT pelvis protocol, megavoltage portal AP images, and kilovoltage planar AP images at the Varian Clinac 21 iX relative to the dose from one fraction of an IMRT irradiation. In (a), the absolute dose is plotted, whereas in (b), the additional relative dose from the imaging procedure compared to the therapeutic stray dose is shown.

Treatment technique Imaging procedure	Effective dose mSv	Additional dose %
Varian 3DCRT	101	
Varian kV CBCT pelvis	32.2	32
Varian kV CBCT pelvis spot light	28.3	28.1
Varian kV CBCT low-dose thorax	8.79	8.72
Varian kV CBCT high-quality head	10.9	10.8
Varian kV planar setup	0.346	0.343
Varian MV portal verification	17.6	17.5
GE LightSpeed planning 3DCT	0.946	0.938
Varian IMRT	133	
Varian kV CBCT pelvis	28.5	21.4
Varian kV CBCT pelvis spot light	25	18.8
Varian kV CBCT low-dose thorax	7.77	5.84
Varian kV CBCT high-quality head	9.63	7.23
Varian kV planar setup	0.306	0.23
GE LightSpeed planning 3DCT	0.946	0.71
GE LightSpeed planning 4DCT	9.95	7.47
Varian VMAT	110	
Varian kV CBCT pelvis	28.5	25.9
Varian kV CBCT pelvis spot light	25	22.8
Varian kV CBCT low-dose thorax	7.77	7.07
Varian kV CBCT high-quality head	9.63	8.76
Varian kV planar setup	0.306	0.278
GE LightSpeed planning 3DCT	0.946	0.86
GE LightSpeed planning 4DCT	9.95	9.05
Varian TrueBeam VMAT FFF	122	
Varian TrueBeam kV CBCT pelvis	15.7	12.9
GE LightSpeed planning 3DCT	0.946	0.778
GE LightSpeed planning 4DCT	9.95	8.18

Table 6.3: Effective doses per total course of treatment, calculated without the dose from measurement points inside the beam ports for Varian treatment machines and imaging modalities, given in mSv. The effective doses for the treatments were taken from another study using the same measurement setup as in this work [81] (see chapter 5). The additional dose from the specific imaging modality to the therapy dose is given in percentage. The listed imaging procedures were applied once per fraction, except for the planning CT scans (once per series) and the portal verification images (once per week, four fields, double exposure).

setup of the patient with two planar kilovoltage images resulted in an additional dose of less than 0.5 %. When megavoltage radiation was used instead of kilovoltage radiation for planar setup images, the dose was about 10 times larger. A fan beam CT at a TomoTherapy unit for daily positioning, resulted in only about 1 % additional dose. On the other hand, a megavoltage CBCT can result in a 30 times larger dose when compared to a fan beam megavoltage CT. This difference can be explained by the

Treatment technique Imaging procedure	Effective dose mSv	Additional dose %
CyberKnife	180	
CyberKnife kV Life Image	13.7	7.62
GE LightSpeed planning 3DCT	0.946	0.526
GE LightSpeed planning 4DCT	9.95	5.54
Elekta IMRT	134	
Elekta kV CBCT pelvis	19.5	14.6
GE LightSpeed planning 3DCT	0.946	0.707
GE LightSpeed planning 4DCT	9.95	7.44
Siemens hard wedge	207	
Siemens MV portal verification	11.1	5.38
GE LightSpeed planning 3DCT	0.946	0.458
Siemens IMRT	163	
Siemens MV CBCT pelvis	45.5	27.9
Siemens MV portal setup	12.8	7.83
GE LightSpeed planning 3DCT	0.946	0.58
GE LightSpeed planning 4DCT	9.95	6.1
TomoTherapy	116	
TomoTherapy MV CT pelvis	1.36	1.17
GE LightSpeed planning 3DCT	0.946	0.817

Table 6.4: Effective doses per total course of treatment, calculated without the dose from measurement points inside the beam ports for different treatment machines and imaging modalities, given in mSv. The effective doses for the treatments were taken from another study using the same measurement setup as in this work [81] (see chapter 5). The additional dose from the specific imaging modality to the therapy dose is given in percentage. The listed imaging procedures were applied once per fraction, except for the planning CT scans (once per series), the stereoscopic images at the CyberKnife (57 images per fraction), and the portal verification images (once per week, four fields, double exposure).

shorter scan length which is possible with a fan beam CT compared to the cone beam geometry and the excellent shielding of the TomoTherapy unit [107]. Using kilovoltage radiation to obtain CBCT scans resulted in a slightly lower dose in the range of 5 % to 30 % additional dose. For a typical CyberKnife treatment without tracking, about 50 kilovoltage images are applied during one fraction of the treatment, leading to a dose deposition of an additional 10 % to the therapeutic stray dose. If tracking techniques are used for a CyberKnife treatment, the number of images can be as large as 400 and therefore the imaging dose can contribute 50 % in addition to the treatment stray dose. In summary, setup imaging using daily kilovoltage planar or TomoTherapy megavoltage fan beam CT imaging only slightly increases the dose to the patient and can be used as a standard procedure in clinical routine. Daily kilovoltage and megavoltage CBCT setup imaging should be applied on an individual or indication based protocol.

If a treatment verification is performed for a typical 3D-conformal four field treatment plan once per week using double exposure technique, an additional dose of up to 20 % is deposited in the patient. It is interesting to note that the dose deposited by such a non-IGRT treatment is comparable to the dose from an IGRT treatment with daily CBCT setup. The reason for this is that the daily CBCT dose is balanced by the dose from the weekly verification images.

The comparison of effective dose presented in this discussion are based on the measurements performed for the curative irradiation of a rhabdomyosarcoma of the prostate. For other treatment intentions and anatomical regions, the influence of the different imaging modalities on the additional dose could be different.

6.5 Conclusion

In this study, dose measurements using thermoluminescent dosimeters were performed to assess and evaluate whole-body imaging dose distributions from typical imaging procedures in image-guided radiation therapy. From these measurements, average organ doses were determined and the corresponding effective dose was calculated according to ICRP Report No. 103 [26]. The effective dose from imaging was compared to the effective dose resulting from therapeutic stray radiation outside of the treatment volume, taken from a study by Hälg et al. [81] (chapter 5 of this thesis) where the same treatment intention and measurement setup were used. It was found that daily kilovoltage planar imaging and TomoTherapy megavoltage fan beam CT for patient setup results in very low additional dose to the patient. The dose from cone beam computed tomography (kilovoltage or megavoltage beams) varies between 5 % (8 mSv) and 30 % (46 mSv) of imaging dose additionally to the treatment stray dose. The dose burden from typical planning CT scans is small (about 1 mSv or 1 % of the therapeutic stray dose), however, when gating methods are employed to obtain the CT scan, the dose can be 10 times larger and the dose increase is in the order of 10 % (10 mSv) compared to the therapeutic stray dose. A complete VMAT treatment course including a planning CT and daily kilovoltage planar setup imaging, reduces the effective dose by around 7 % (8 mSv) when compared to a non-IGRT treatment using four fields, a planning CT, and weekly treatment verification images. If the same VMAT treatment is administered with daily cone beam computed tomography instead of planar images, the effective dose is increased

by 17 % (20 mSv) compared to the non-IGRT treatment. It can be therefore concluded that the additional dose burden for patients treated with IGRT is lower than usually assumed, when the contributions to the dose outside of the treatment volume from all sources are included.

Acknowledgements

This work was funded in part by the KIRO grant from the Federal Office of Public Health (FOPH), Switzerland.

The authors would like to express their gratitude to M. Gantert, S. Khan, and G. Lutters from Canton Hospital Aarau, to S. Peters and H. Schiefer from Canton Hospital St. Gallen, to A. Joosten and R. Moeckli from Centre Hospitalier Universitaire Vaudois, Lausanne, to D. Klass and P. Pemler from City Hospital Triemli, Zurich, to A. Lehde and C. Algranati from Paul Scherrer Institut, Villigen, to A. M. MacArtain from Radiotherapie Hirslanden AG, Aarau, to A. Mack and P. Nobis from Radiotherapie Hirslanden AG, Zurich, and to S. Lang and J. Hrbacek from University Hospital, Zurich, for helping and giving the opportunity to perform the measurements at their institutions.

6.A Organ doses

Lists of average organ doses for the imaging modalities investigated, given as dose per image or per scan, respectively. (Tables 6.6–6.9)

Organ	Pelvis µGy	Pelvis spot light µGy	Low-dose thorax µGy	High-quality head µGy
Bladder	25400	22600	6970	9960
Bone	5230	7100	1440	2770
Brain and CNS	150	152	38.4	63.4
Colon	6960	7260	1870	2830
Female breast	155	111	43.1	58.4
Heart	161	104	42.9	49.2
Kidney	787	750	193	284
Liver	583	453	158	190
Lung	152	136	40.7	68.5
Mouth and pharynx	46	23.5	11.9	12.7
Oesophagus	105	95.7	27.2	46.6
Rectum	28300	40300	7690	17500
Remainder	16200	18600	4570	7280
Salivary gland	46.2	25.4	12.1	14.6
Skin	9950	11100	2880	4140
Small intestine	12700	7330	3490	3020
Stomach	273	197	73	81.6
Thyroid	56.9	29.4	14.7	14.3

Table 6.5: Different CBCT imaging protocols at the Varian OBI: Mean organ doses in µGy per scan.

Organ	Elekta kV CBCT µGy	Siemens MV CBCT µGy	TomoTherapy MV CT µGy	TrueBeam kV CBCT µGy
Bladder	35500	24100	7940	16500
Bone	6210	6860	1010	3050
Brain and CNS	114	138	11.7	86.6
Colon	6740	9960	708	3790
Female breast	195	95.8	12.4	129
Heart	164	112	14	120
Kidney	498	533	49.5	353
Liver	409	350	36.6	283
Lung	163	94.5	13	116
Mouth and pharynx	52	34.5	3.13	41.2
Oesophagus	111	83.4	10.9	84.9
Rectum	38500	22600	6810	17200
Remainder	22900	16100	3860	9600
Salivary gland	52.4	34.2	3.4	44.6
Skin	12100	9280	1170	5460
Small intestine	12300	18600	712	7730
Stomach	237	188	22.1	172
Thyroid	62.5	45.5	4.67	46.4

Table 6.6: Computed tomography devices mounted on treatment machines: Mean organ doses in µGy per scan.

Organ	GE LightSpeed planning CT µGy	GE LightSpeed planning 4DCT µGy
Bladder	13600	172000
Bone	3350	40800
Brain and CNS	81.8	828
Colon	4600	52500
Female breast	45.7	513
Heart	50.8	547
Kidney	458	4570
Liver	333	2790
Lung	54.3	630
Mouth and pharynx	6.14	74.1
Oesophagus	38.6	424
Rectum	13700	182000
Remainder	9210	123000
Salivary gland	6.83	80.3
Skin	5860	84800
Small intestine	8180	93600
Stomach	119	1260
Thyroid	10.1	117

Table 6.7: 3D- and 4DCT for treatment planning: Mean organ doses in µGy per scan.

Organ	CyberKnife Live Image µGy	GE HiSpeed scout view µGy	Varian OBI planar AP µGy	Varian OBI planar LAT µGy
Bladder	181	430	102	202
Bone	57.3	101	9.98	56.2
Brain and CNS	8.91	5.23	0.168	1.34
Colon	167	140	20.9	29.3
Female breast	3.99	2.3	0.306	1.63
Heart	4.78	2.29	0.246	1.07
Kidney	69.1	26.5	1.24	5.38
Liver	54.8	22.6	1.51	6.39
Lung	3.56	1.77	0.172	1.17
Mouth and pharynx	0.707	0.209	0.0255	0.586
Oesophagus	2.83	1.47	0.0788	0.965
Rectum	106	297	53.8	142
Remainder	203	372	60.2	224
Salivary gland	0.653	0.303	0.0246	0.6
Skin	133	217	39.1	266
Small intestine	274	417	66.2	82
Stomach	13	5.36	0.447	1.43
Thyroid	1.43	0.368	0.0476	0.644

Table 6.8: Different planar kV imaging modalities for patient positioning: Mean organ doses in µGy per image.

Organ	Elekta portal AP+LAT double exposure µGy	Siemens portal AP+LAT µGy	Varian portal AP µGy
Bladder	158000	31300	13400
Bone	18600	6390	2840
Brain and CNS	140	71.5	31.1
Colon	22600	6910	3300
Female breast	123	64	24.3
Heart	137	79.4	32.3
Kidney	452	267	121
Liver	311	193	90.2
Lung	120	66.6	26
Mouth and pharynx	65.6	30.1	7.02
Oesophagus	107	57.9	22.3
Rectum	131000	29800	11100
Remainder	61400	16200	5890
Salivary gland	64.3	28.9	7.21
Skin	23300	6510	1930
Small intestine	31600	12000	6280
Stomach	197	127	54.1
Thyroid	66.5	36.5	10.2

Table 6.9: Different MV portal imaging modalities: Mean organ doses in µGy per image.

6.B Imaging procedure settings

List of the settings of all the imaging modalities investigated.

Cone beam computed tomography

- **Varian OBI CBCT pelvis protocol**
  Voltage: 125 kV, Current: 80 mA, Pulse width: 13 ms
  Blades: X1 6.8 cm, X2 23.5 cm, Y1 10.3 cm, Y2 10.3 cm
  Imager vrt 50.0 cm, Imager lng 0.0 cm, Imager lat 14.8 cm
  SAD: 100.0 cm, Focal spot: large, Acquisition mode: half fan
  Reconstruction volume: 384 × 384, Slice distance: 2.5 mm

- **Varian OBI CBCT pelvis spot light protocol**
  Voltage: 125 kV, Current: 80 mA, Pulse width: 25 ms
  Blades: X1 13.6 cm, X2 13.6 cm, Y1 9.2 cm, Y2 9.2 cm
  Imager vrt 50.0 cm, Imager lng 0.0 cm, Imager lat 0.0 cm
  SAD: 100.0 cm, Focal spot: large, Acquisition mode: full fan
  Reconstruction volume: 384 × 384, Slice distance: 2.5 mm

- **Varian OBI CBCT low-dose thorax protocol**
  Voltage: 110 kV, Current: 20 mA, Pulse width: 20 ms
  Blades: X1 13.6 cm, X2 13.6 cm, Y1 10.3 cm, Y2 10.3 cm
  Imager vrt 50.0 cm, Imager lng 0.0 cm, Imager lat 14.8 cm
  SAD: 100.0 cm, Focal spot: small, Acquisition mode: half fan
  Reconstruction volume: 384 × 384, Slice distance: 2.5 mm

- **Varian OBI CBCT high-quality head protocol**
  Voltage: 100 kV, Current: 80 mA, Pulse width: 25 ms
  Blades: X1 13.6 cm, X2 13.6 cm, Y1 10.3 cm, Y2 10.3 cm
  Imager vrt 50.0 cm, Imager lng 0.0 cm, Imager lat 0.0 cm
  SAD: 100.0 cm, Focal spot: small, Acquisition mode: full fan
  Reconstruction volume: 384 × 384, Slice distance: 2.5 mm

- **Varian TrueBeam XI CBCT pelvis protocol**
  Voltage: 125 kV, Current × time: 686.40 mA s
  Imager vrt 50.0 cm, Imager lng 0.0 cm, Imager lat 984.0 cm
  SAD: 100.0 cm, Fan type: half, Trajectory: full
  Gantry rotation: 184.5 E to 175.5 E

- **Elekta XVI CBCT prostate protocol**
  Voltage: 120 kV, Current: 64 mA, Pulse width: 40 ms

Filter: F1, Collimator: M10, Current × time: 1652.2 mA s
Gantry rotation: −179° to 178°

- **Siemens** MV **CBCT pelvis protocol**
  Voltage: 6 MV, Dose rate: 50 MU/min, Dose: 3 MU
  Collimation: X 27.4 cm, Y 27.4 cm
  Gantry rotation: 270° to 110°

Fan beam computed tomography

- **GE LightSpeed planning CT pelvis protocol**
  Scout frontal: Voltage: 120 kV, Current: 80 mA
  Scout length: S300, I300
  CT scan: Voltage: 120 kV, Current: 110 mA, Exposure time: 15.7 s
  CT scan length: S110, I85, Slices: 79, Slice thickness: 2.5 mm

- **GE LightSpeed planning CT 4DCT + gating protocol**
  Scout frontal: Voltage: 120 kV, Current: 80 mA
  Scout length: S300, I300
  CT scan: Voltage: 120 kV, Current: 400 mA, Exposure time: 90.1 s
  CT scan length: S110, I87.5, Slices: 880, Slice thickness: 2.5 mm

- **GE HiSpeed scout view protocol**
  Scout frontal: Voltage: 120 kV, Current: 80 mA
  Scout sagittal: Voltage: 120 kV, Current: 100 mA
  Scout length: S148, I185

- **TomoTherapy pelvis protocol**
  Voltage: 3 MV, Slice thickness: coarse
  Scan length: PTV + 1 slice cranial and caudal

Planar imaging

- **CyberKnife Life Image protocol**
  Voltage: 120 kV, Current: 100 mA
  Direction: stereoscopic

- **Varian OBI pelvis-ap-med protocol**
  Voltage: 75 kV, Current: 100 mA, Pulse width: 50 ms
  Blades: X1 10.0 cm, X2 10.0 cm, Y1 10.0 cm, Y2 10.0 cm
  Imager vrt 50.0 cm, Imager lng 0.0 cm, Imager lat 0.0 cm

SAD: 100.0 cm, Size: normal
Direction: AP, Gantry rtn: 90.0°, Source rtn: 0.0°

- **Varian OBI pelvis-lat-med protocol**
  Voltage: 105 kV, Current: 40 mA, Pulse width: 200 ms
  Blades: X1 10.0 cm, X2 10.0 cm, Y1 10.0 cm, Y2 10.0 cm
  Imager vrt 50.0 cm, Imager lng 0.0 cm, Imager lat 0.0 cm
  SAD: 100.0 cm, Size: normal
  Direction: LAT, Gantry rtn: 0.0°, Source rtn: 270.0°

Portal imaging

- **Elekta iView prostate protocol**
  Voltage: 6 MV
  Direction: AP, Gantry: 0°, Field size: 10 cm × 10 cm, Dose: 5 MU
  Direction: AP, Gantry: 0°, Field size: 16 cm × 16 cm, Dose: 5 MU
  Direction: LAT, Gantry: 90°, Field size: 8 cm × 10 cm, Dose: 5 MU
  Direction: LAT, Gantry: 90°, Field size: 14 cm × 16 cm, Dose: 5 MU

- **Siemens pelvis protocol**
  Voltage: 6 MV
  Direction: AP, Gantry: 0°, Field size: 20 cm × 16 cm, Dose: 2 MU
  Direction: LAT, Gantry: 90°, Field size: 16 cm × 16 cm, Dose: 2 MU

- **Varian PVI protocol**
  Voltage: 6 MV, Acquisition: low dose image (two frames averaged)
  Direction: AP, Gantry: 0°, Field size: 20 cm × 20 cm, Dose: 1 MU

Chapter 7

Conclusion and Outlook

Advances in the application of ionising radiation to treat patients in radiation oncology over the last few decades have lead to a substantial increase in the cure rates or to a higher probability to at least control the disease. On the other hand, there are concerns about radiation-related late effects in long-term radiotherapy survivors. Survivors of a primary cancer are at risk of developing a treatment induced second primary cancer and consequently the need to be able to predict cancer risks after exposure to high radiation doses has arisen. Available cancer risk estimates for radiation protection purposes focus on the dose range from zero to one Gray and should only be used with extreme care for the quantification of the risks in radiotherapy. The time has come to analyse contemporary treatment techniques in radiation oncology not only in terms of tumour control probability and acute toxicity, but also in terms of the risk of late effects such as second cancers.

In this thesis a complete assessment of radiation doses involved in the process of a typical treatment of cancer patients has been presented. The same measurement setup and treatment intention has been applied to measure the dose distributions for the treatment and imaging irradiations. For the determination of neutron stray dose during high-energy photon or proton radiotherapy, a new calibration procedure has been developed. This calibration of the dosimeters allows the measurement of local neutron dose equivalent inside phantoms, which is not possible with commonly available neutron dosimeters. The photon stray dose from treatment irradiations using various treatment machines and delivery techniques has been measured. This allows a detailed comparison of the treatment machines and the delivery techniques in terms of the treatment dose, the out-of-field dose, and the dose in radiation sensitive organs. To our

knowledge, this is the most comprehensive study on photon stray dose in radiation therapy in the literature. The importance of imaging procedures in radiation oncology is steadily increasing and the trend is to apply even more imaging modalities in clinical routine in the future. The acquired list of whole-body imaging dose distributions covers all major imaging procedures applied in modern radiotherapy. This gives the clinician the possibility to compare the imaging modalities in terms of dose burden to the patient and consequently to judge the cost and benefit for an optimised image-guided treatment. The presented catalogue of imaging doses is not only one of the most extensive available nowadays. It also allows a direct combination of imaging dose and stray dose from therapy to evaluate the whole-body dose distribution for a complete image-guided radiotherapy treatment course. The outcome of this thesis is a comprehensive basis for the modelling of radiation related cancer risk in modern radiation oncology.

The stray doses from different therapy techniques and imaging modalities used for image-guided radiation therapy have been presented in Chapters 5 and 6. The doses were combined to estimate the dose burden for a complete treatment including imaging modalities for patient setup. To further investigate the influence of the different imaging modalities on the increase of the total dose to the patient, image-guidance schemes can be defined and the resulting dose increase can be determined. A list of four possible examples of imaging schemes for IGRT are shown in Table 7.1. An imaging scheme based on cone beam computed tomography (scheme CBCT) is compared to setup procedures of the patient using planar imaging with only kilovoltage images (scheme kV-kV), to a mixed setup using kilo- and megavoltage images (scheme kV-MV) and to a scheme used before image-guidance where only megavoltage portal images are used for treatment field verification (scheme MV). The number of applied imaging procedures furthermore depends on the fractionation of the therapy: a daily application of an imaging procedure incurs a total of 26 applications for the 3D-conformal fractionation scheme ($26 \times 2.0\,\mathrm{Gy}$), whereas imaging on a daily basis leads to 23 applications for the intensity-modulated treatments ($23 \times 2.2\,\mathrm{Gy}$). This is shown in Table 7.1 with the numbers left and right of the slash. The use of portal megavoltage images for treatment field verification is limited to the 3D-conformal treatment for IGRT. Treatment plans applying intensity-modulated beams are usually verified using phantom measurements before the patient is irradiated for the first time. The irradiation using the 3D-conformal four field treatment plan is applied in two series, which leads to a total of 8 portal images. For

Scheme	CBCT	Portal MV	Planar kV-kV	Planar kV-MV
Scheme CBCT	26/23	8/0	0/0	0/0
Scheme kV-kV	0/0	8/0	26/23	0/0
Scheme kV-MV	0/0	8/0	0/0	26/23
Scheme MV	0/0	20/20	0/0	0/0

Table 7.1: Irradiation schemes for the combination of treatment stray dose and dose from different imaging procedures. On the left side of the slash, the number of image procedure applications for the 3D-conformal therapy fractionation ($26 \times 2.0\,\mathrm{Gy}$) and on the right side the number for the fractionation of the intensity-modulated treatments ($23 \times 2.2\,\mathrm{Gy}$) is shown.

the non-IGRT scheme, a weekly verification of the four treatment fields is assumed, resulting in a total of 20 portal images.

The resulting total dose from combinations of different IGRT imaging schemes is plotted relative to the therapy dose in Figures 7.1 and 7.2. Thus the additional dose burden from imaging can be quantified in terms of the unavoidable therapeutic dose. The dose is shown along the medial patient axis from the isocenter in the prostate at $x = 0\,\mathrm{cm}$ to the head ($x = 82.5\,\mathrm{cm}$). The vertical lines represent the border of the target volume along this direction. For each irradiation technique the resulting dose for all the imaging schemes in Table 7.1 is plotted, except for the TomoTherapy unit, where only megavoltage fan beam CTs are available for patient positioning. The local relative increase of the dose because of the applied imaging scheme varies between below 0.5 % and 30 %. The results from Figures 7.1 and 7.2 can be used as a guideline for dose monitoring in the clinical practise for the management of IGRT doses.

The aim of this thesis was to assess as many different contributions to the integral dose of a patient in radiation therapy as reasonably possible. A potential extension of the dose measurements presented here would be the measurement of stray doses from high-energy photon treatments. Most of the delivery techniques investigated in Chapter 5 can also be applied using different photon energies. The presented photon therapy stray dose measurements were done using 6 MV beams. Higher photon energies have the advantage of more forward directed patient scatter and a larger build-up region, which increases the skin-sparing effect of the radiation. High-energy photon beams have shown benefits for the treatment of deep seated tumours. The disadvantages are an increase in head leakage radiation, the production of neutrons and a higher exit dose. It would be interesting to assess the photon stray dose for the high-energy photon beams from Chapter 3 in order to combine it with the neutron dose and

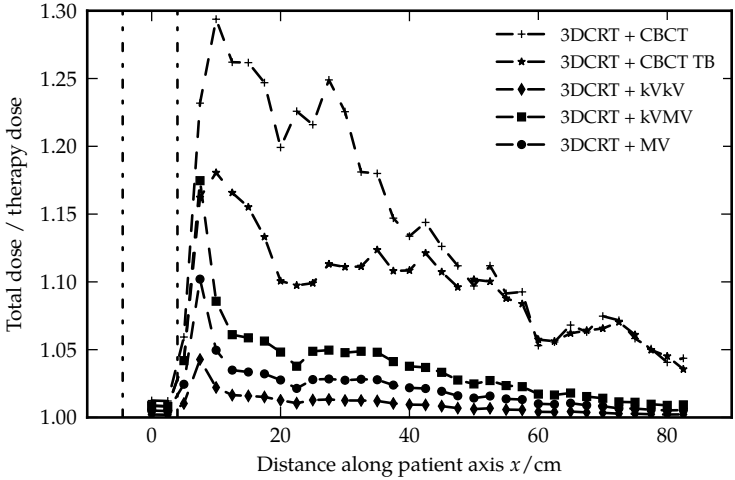

(a) Additional relative dose: Varian 3DCRT with imaging

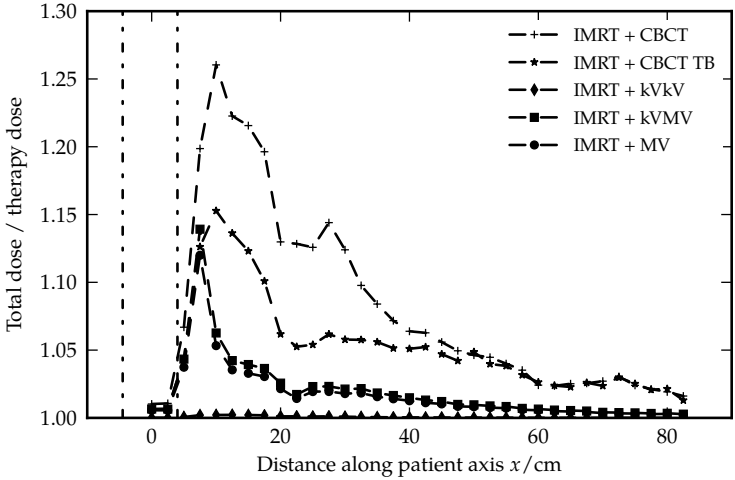

(b) Additional relative dose: Varian IMRT with imaging

Figure 7.1: Comparison of the additional dose from different IGRT schemes. In (a), for the 3D-conformal irradiation (3DCRT) and in (b) for the intensity-modulated radiotherapy irradiation (IMRT) at the Varian Clinac 21 iX. The cone beam computed tomography using the imaging device on the Varian TrueBeam linear accelerator is abbreviated with "CBCT TB".

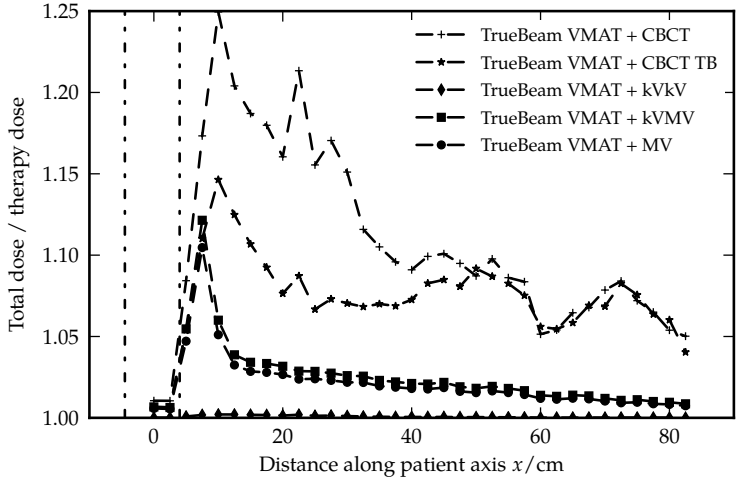

(a) Additional relative dose: Varian VMAT FFF with imaging

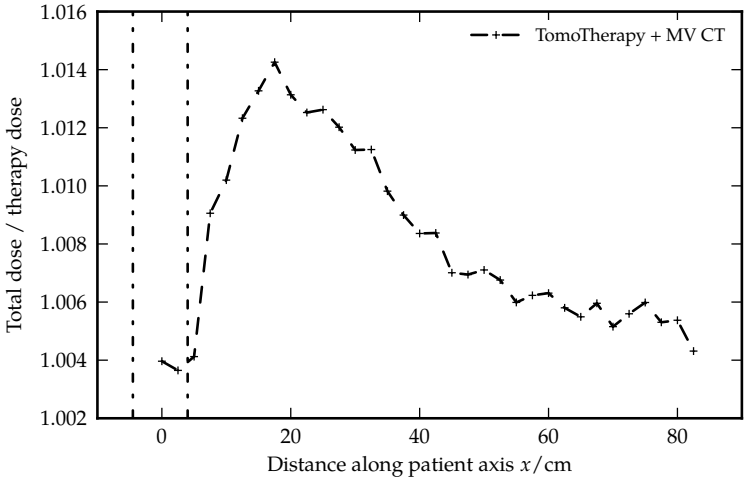

(b) Additional relative dose: Accuray TomoTherapy with imaging

Figure 7.2: Comparison of the additional dose from different IGRT schemes. In (a) for the flattening filter-free volumetric modulated arc therapy irradiation (VMAT FFF) at the TrueBeam and in (b) for the helical TomoTherapy irradiation and the TomoTherapy unit. The cone beam computed tomography using the imaging device on the Varian TrueBeam linear accelerator is abbreviated with "CBCT TB".

determine the total dose to the patient. This would give the possibility to compare the total dose from high-energy photon treatments to low-energy photon and proton treatments. As pointed out in Section 5.4.4, the measurement of photon stray dose in a mixed field of photons and neutrons is not possible with the detectors used there. A different neutron-blind thermoluminescent material and an adapted handling protocol would be necessary to perform these measurements.

The application of heavy charged particles in radiation therapy is not limited to protons. The first beam line for radiotherapy using heavy ions was built at the University of California in Berkeley in 1977 and the interest in ion radiotherapy has steadily been increasing especially in Japan and Europe [108]. This interest is accompanied by intensive technical, physical, and clinical research and important progress is being made [109]. Most beam lines use carbon ions to treat patients. They share some of the advantages and disadvantages with proton beams. One of the disadvantages is the production of neutrons. The measurement series in this study could be expanded with neutron dose measurements at an ion beam therapy facility. This would allow the comparison of neutron dose from carbon ion treatments with neutron dose from proton and high-energy photon beams.

The extent of the presented dose catalogue for procedures in radiation oncology is a good starting point for modelling of cancer induction for radiotherapy survivors. A basis is provided to use sophisticated models for cancer risk estimation. Usually, the formalism of effective dose has been applied for estimations of cancer risk, which is not advisable for doses in the radiotherapy regime and is heavily overrating cancer risk from IGRT. The results of this work in combination with sophisticated dose response models for radiation induced cancer would allow more realistic cancer risk estimates for patients who are simultaneously imaged and treated with ionising radiation.

There are efforts in radiation oncology to include the determination of normal tissue complication probability (NTCP) into clinical routine for the evaluation of different treatment plans for the same patient. To go one step further, it would be interesting to link the determined NTCP with the estimation of the risk for second cancer induction. Modern treatment techniques lead to higher conformity of the dose to the target volume compared to conventional treatments. This leads to a reduction of the NTCP. On the other hand, modern treatment techniques using intensity modulation increase the out-of-field dose compared to conventional techniques. As has been discussed in this thesis, this is expected to lead to an increased

rate of second cancers. A balancing of these two aspects should be investigated for the benefit of the patient. However, flattening filter-free delivery of treatment plans showed that the stray dose can be reduced although intensity modulation is applied, which is a promising aspect for further developments in radiation therapy.

One of the most important goals for the optimisation of radiation therapy is to reduce the volume of the irradiated tissue. The application of image-guidance has lead to reductions in the safety margins added to the target structures for the irradiation. The imaging procedures allow the verification of the accuracy of the position of the target before or possibly during the treatment, which justifies the reduction of the margins. But the ionising radiation used by the imaging modalities increases the risk for radiation induced cancers. Further studies are necessary to investigate the correlation between these two aspects and to judge the importance of stray dose to the patients in radiation oncology.

Since modern radiotherapy methods progressively decrease the stray dose and can be expected to continue to do so in the future, the stray dose incurred by imaging methods could become more troublesome. Alternative non-ionising image guiding methods like ultrasound or magnetic resonance imaging may become valuable options to further reduce the integral dose of a patient.

Bibliography

[1] H. Suit, S. Goldberg, A. Niemierko, M. Ancukiewicz, E. Hall, M. Goitein, W. Wong, and H. Paganetti. *Secondary carcinogenesis in patients treated with radiation: A review of data on radiation-induced cancers in human, non-human primate, canine and rodent subjects*. Radiation Research, **167**, 12–42 (2007)

[2] R. L. Cumberlin, A. Dritschilo, and K. L. Mossman. *Carcinogenic effects of scattered dose associated with radiation-therapy*. International Journal of Radiation Oncology, Biology, Physics, **17**, 623–629 (1989)

[3] W. Dorr and T. Herrmann. *Second primary tumors after radiotherapy for malignancies—Treatment-related parameters*. Strahlentherapie und Onkologie, **178**, 357–362 (2002)

[4] Neugut and Meadows. *Multiple Primary Cancers* (Lippincott Williams & Wilkins1999)

[5] D. Followill, P. Geis, and A. Boyer. *Estimates of whole-body dose equivalent produced by beam intensity modulated conformal therapy*. International Journal of Radiation Oncology, Biology, Physics, **38**, 667–672 (1997)

[6] E. J. Hall and C. S. Wuu. *Radiation-induced second cancers: The impact of 3D-CRT and IMRT*. International Journal of Radiation Oncology, Biology, Physics, **56**, 83–88 (2003)

[7] J. Rowland, A. Mariotto, N. Aziz, G. Tesauro, E. J. Feuer, D. Blackman, P. Thompson, and L. A. Pollack. *Cancer survivorship — United States, 1971-2001*. MMWR; Morbidity and Mortality Weekly Report, **53**, 526–529 (2004)

[8] S. Bhatia and C. Sklar. *Second cancers in survivors of childhood cancer*. Nature Reviews Cancer, **2**, 124–132 (2002)

[9] W. D. Newhauser and M. Durante. *Assessing the risk of second malignancies after modern radiotherapy*. Nature Reviews Cancer, **11**, 438–448 (2011)

[10] U. Schneider. *Modeling the risk of secondary malignancies after radiotherapy*. Genes, **2**, 1033–1049 (2011)

[11] T. Bortfeld, R. Schmidt-Ullrich, W. De Neve, and D. E. Wazer. *Image-Guided IMRT* (Springer Berlin Heidelberg2006)

[12] H. A. Bethe and J. Ashkin. *Passage of radiations through matter*. Experimental Nuclear Physics, **1**, 309 (1953)

[13] A. Fassò, A. Ferrari, J. Ranft, and P. R. Sala. *FLUKA: a multi-particle transport code*. Tech. Rep. CERN-2005-10, INFN/TC-05/11, SLAC-R-773, CERN - Organisation europenne pour la recherche nucleaire / European organization for nuclear research (2005)

[14] G. Battistoni, F. Cerutti, A. Fassò, A. Ferrari, S. Muraro, J. Ranft, S. Roesler, and P. R. Sala. *The FLUKA code: description and benchmarking*. Hadronic Shower Simulation Workshop, **896**, 31–49 (2007)

[15] V. Vlachoudis. *FLAIR: A powerful but user friendly graphical interface for FLUKA*. In *Proc. Int. Conf. on Mathematics, Computational Methods & Reactor Physics (M&C 2009)* (Saratoga Springs, New York2009)

[16] E. Pedroni, R. Bacher, H. Blattmann, T. Bohringer, A. Coray, A. Lomax, S. X. Lin, G. Munkel, S. Scheib, U. Schneider, and A. Tourovsky. *The 200-MeV proton therapy project at the Paul Scherrer Institute: Conceptual design and practical realization*. Medical Physics, **22**, 37–53 (1995)

[17] A. J. Lomax. *Intensity modulation methods for proton radiotherapy*. Physics in Medicine and Biology, **44**, 185–205 (1999)

[18] A. J. Lomax, T. Boehringer, A. Coray, E. Egger, G. Goitein, M. Grossmann, P. Juelke, S. Lin, E. Pedroni, B. Rohrer, W. Roser, B. Rossi, B. Siegenthaler, O. Stadelmann, H. Stauble, C. Vetter, and L. Wisser. *Intensity modulated proton therapy: A clinical example*. Medical Physics, **28**, 317–324 (2001)

[19] X. G. Xu, B. Bednarz, and H. Paganetti. *A review of dosimetry studies on external-beam radiation treatment with respect to second cancer induction*. Physics in Medicine and Biology, **53**, R193–R241 (2008)

[20] A. M. Kellerer and L. Walsh. *Risk estimation for fast neutrons with regard to solid cancer*. Radiation Research, **156**, 708–717 (2001)

[21] C. Z. Jarlskog and H. Paganetti. *Risk of developing second cancer from neutron dose in proton therapy as function of field characteristics, organ, and patient age*. International Journal of Radiation Oncology, Biology, Physics, **72**, 228–235 (2008)

[22] R. Takam, E. Bezak, L. G. Marcu, and E. Yeoh. *Out-of-field neutron and leakage photon exposures and the associated risk of second cancers in high-energy photon radiotherapy: Current status*. Radiation Research, **176**, 508–520 (2011)

[23] International Commission on Radiological Units and Measurements. *Determination of Dose Equivalents Resulting from External Radiation Sources*. No. 39 in ICRU Report (International Commission on Radiation Units and Measurements, Bethesda, MD, USA1985)

[24] International Commission on Radiological Units and Measurements. *Determination of Dose Equivalents from External Radiation Sources – Part II*. No. 43 in ICRU Report (International Commission on Radiation Units and Measurements, Bethesda, MD, USA1988)

[25] International Commission on Radiological Protection. *1990 Recommendations of the International Commission on Radiological Protection. ICRP publication 60*. Annals of the ICRP, **21**, 1–201 (1991)

[26] International Commission on Radiological Protection. *The 2007 Recommendations of the International Commission on Radiological Protection. ICRP Publication 103*. Annals of the ICRP, **37**, 1–332 (2007)

[27] N. Chofor, D. Harder, K. C. Willborn, and B. Poppe. *Internal scatter, the unavoidable major component of the peripheral dose in photon-beam radiotherapy*. Physics in Medicine and Biology, **57**, 1733–1743 (2012)

[28] L. Cozzi, F. M. Buffa, and A. Fogliata. *Dosimetric features of linac head and phantom scattered radiation outside the clinical photon beam: experimental measurements and comparison with treatment planning system calculations*. Radiotherapy and Oncology, **58**, 193–200 (2001)

[29] R. M. Howell, S. B. Scarboro, S. F. Kry, and D. Z. Yaldo. *Accuracy of out-of-field dose calculations by a commercial treatment planning system*. Physics in Medicine and Biology, **55**, 6999–7008 (2010)

[30] S. F. Kry, U. Titt, F. Ponisch, D. Followill, O. N. Vassiliev, R. A. White, R. Mohan, and M. Salehpour. *A Monte Carlo model for calculating out-of-field dose from a Varian 6 MV beam*. Medical Physics, **33**, 4405–4413 (2006)

[31] J. Lehmann, R. L. Stern, T. P. Daly, D. M. Rocke, C. W. Schwietert, G. E. Jones, M. L. Arnold, C. L. Hartmann Siantar, and Z. Goldberg. *Dosimetry for quantitative analysis of the effects of low-dose ionizing radiation in radiation therapy patients*. Radiation Research, **165**, 240–247 (2006)

[32] B. Bednarz and X. G. Xu. *Monte Carlo modeling of a 6 and 18 MV Varian Clinac medical accelerator for in-field and out-of-field dose calculations: development and validation*. Physics in Medicine and Biology, **54**, N43–N57 (2009)

[33] A. Joosten, F. Bochud, S. Baechler, F. Levi, R.-O. Mirimanoff, and R. Moeckli. *Variability of a peripheral dose among various linac geometries for second cancer risk assessment*. Physics in Medicine and Biology, **56**, 5131–5151 (2011)

[34] R. Mohan, X. H. Wang, A. Jackson, T. Bortfeld, A. L. Boyer, G. J. Kutcher, S. A. Leibel, Z. Fuks, and C. C. Ling. *The potential and limitations of the inverse radiotherapy technique*. Radiotherapy and Oncology, **32**, 232–248 (1994)

[35] C. Burman, C. S. Chui, G. Kutcher, S. Leibel, M. Zelefsky, T. LoSasso, S. Spirou, Q. W. Wu, J. Yang, J. Stein, R. Mohan, Z. Fuks, and C. C. Ling. *Planning, delivery, and quality assurance of intensity-modulated radiotherapy using dynamic multileaf collimator: A strategy for large-scale implementation for the treatment of carcinoma of the prostate*. International Journal of Radiation Oncology, Biology, Physics, **39**, 863–873 (1997)

[36] A. Pirzkall, M. P. Carol, B. Pickett, P. Xia, M. Roach, and L. J. Verhey. *The effect of beam energy and number of fields on photon-based IMRT for deep-seated targets*. International Journal of Radiation Oncology, Biology, Physics, **53**, 434–442 (2002)

[37] D. R. Simpson, J. D. Lawson, S. K. Nath, B. S. Rose, A. J. Mundt, and L. K. Mell. *A survey of image-guided radiation therapy use in the United States*. Cancer, **116**, 3953–3960 (2010)

[38] U. Schneider, S. Agosteo, E. Pedroni, and J. Besserer. *Secondary neutron dose during proton therapy using spot scanning*. International Journal of Radiation Oncology, Biology, Physics, **53**, 244–251 (2002)

[39] D. S. Followill, M. S. Stovall, S. F. Kry, and G. S. Ibbott. *Neutron source strength measurements for Varian, Siemens, Elekta, and General Electric linear accelerators*. Journal of applied clinical medical physics, **4**, 189–194 (2003)

[40] F. Vanhavere, D. Huyskens, and L. Struelens. *Peripheral neutron and gamma doses in radiotherapy with an 18 MV linear accelerator*. Radiation Protection Dosimetry, **110**, 607–612 (2004)

[41] S. F. Kry, M. Salehpour, D. S. Followill, M. Stovall, D. A. Kuban, R. A. White, and I. I. Rosen. *Out-of-field photon and neutron dose equivalents from step-and-shoot intensity-modulated radiation therapy*. International Journal of Radiation Oncology, Biology, Physics, **62**, 1204–1216 (2005)

[42] R. M. Howell, N. E. Hertel, Z. Wang, J. Hutchinson, and G. D. Fullerton. *Calculation of effective dose from measurements of secondary neutron spectra and scattered photon dose from dynamic MLC IMRT for 6 MV, 15 MV, and 18 MV beam energies*. Medical Physics, **33**, 360–368 (2006)

[43] C. S. Reft, R. Runkel-Muller, and L. Myrianthopoulos. *In vivo and phantom measurements of the secondary photon and neutron doses for prostate patients undergoing 18 MV IMRT*. Medical Physics, **33**, 3734–3742 (2006)

[44] P. J. Binns and J. H. Hough. *Secondary dose exposures during 200 MeV proton therapy*. Radiation Protection Dosimetry, **70**, 441–444 (1997)

[45] X. Yan, U. Titt, A. M. Koehler, and W. D. Newhauser. *Measurement of neutron dose equivalent to proton therapy patients outside of the proton radiation field*. Nuclear Instruments & Methods in Physics Research, Section A: Accelerators, Spectrometers, Detectors, and Associated Equipment, **476**, 429–434 (2002)

[46] S. C. Roy and G. A. Sandison. *Scattered neutron dose equivalent to a fetus from proton therapy of the mother*. Radiation Physics and Chemistry, **71**, 997–998 (2004)

[47] G. Mesoloras, G. A. Sandison, R. D. Stewart, J. B. Farr, and W. C. Hsi. *Neutron scattered dose equivalent to a fetus from proton radiotherapy of the mother*. Medical Physics, **33**, 2479–2490 (2006)

[48] R. Tayama, Y. Fujita, M. Tadokoro, H. Fujimaki, T. Sakae, and T. Terunuma. *Measurement of neutron dose distribution for a passive scattering nozzle at the Proton Medical Research Center (PMRC)*. Nuclear Instruments & Methods in Physics Research, Section A: Accelerators, Spectrometers, Detectors, and Associated Equipment, **564**, 532–536 (2006)

[49] A. Wroe, A. Rosenfeld, and R. Schulte. *Out-of-field dose equivalents delivered by proton therapy of prostate cancer*. Medical Physics, **34**, 3449–3456 (2007)

[50] M. Yoon, S. H. Ahn, J. Kim, D. H. Shin, S. Y. Park, S. B. Lee, K. H. Shin, and K. H. Cho. *Radiation-induced cancers from modern radiotherapy techniques: intensity-modulated radiotherapy versus proton therapy*. International Journal of Radiation Oncology, Biology, Physics, **77**, 1477–1485 (2010)

[51] S. F. Kry, M. Salehpour, U. Titt, R. A. White, M. Stovall, and D. Followill. *Monte Carlo study shows no significant difference in second cancer risk between 6-and 18-MV intensity-modulated radiation therapy*. Radiotherapy and Oncology, **91**, 132–137 (2009)

[52] A. Fiechtner and C. Wernli. *Individual neutron monitoring with CR-39 detectors at an accelerator centre*. Radiation Protection Dosimetry, **85**, 35–38 (1999)

[53] A. Fiechtner and C. Wernli. *Neutronendosimetrie mit CR-39-Detektoren und AUTOSCAN 60. Anwendung bei PSI-Beschleunigerspektren*. Tech. Rep. TM-23-97-10, Paul Scherrer Institut (PSI), Villigen, Switzerland (1998)

[54] A. M. Kellerer. *Weighting factors for radiation quality: How to unite the two current concepts*. Radiation Protection Dosimetry, **110**, 781–787 (2004)

[55] A. M. Kellerer, G. Leuthold, V. Mares, and H. Schraube. *Options for the modified radiation weighting factor of neutrons*. Radiation Protection Dosimetry, **109**, 181–188 (2004)

[56] H. Hoedlmoser, C. Schuler, G. Butterweck, N. Chételat, and S. Mayer. *Characterization of the ^{241}Am-Be neutron source of the PSI Calibration Laboratory*. Tech. Rep. TM-96-11-02, Paul Scherrer Institut (PSI), Villigen, Switzerland (2011)

[57] H. Schuhmacher. *Neutron calibration facilities*. Radiation Protection Dosimetry, **110**, 33–42 (2004)

[58] IAEA Safety Reports Series No. 16. *Calibration of Radiation Protection Monitoring Instruments* (International Atomic Energy Agency, Vienna, Austria2000)

[59] ISO 4037-1:1996. *X and gamma reference radiation for calibrating dosemeters and doserate meters and for determining their response as a function of photon energy – Part 1: Radiation characteristics and production methods* (International Organization for Standardization, Geneva, Switzerland1996)

[60] ISO 4037-2:1997. *X and gamma reference radiation for calibrating dosemeters and doserate meters and for determining their response as a function of photon energy – Part 2: Dosimetry for radiation protection over the energy ranges from 8 keV to 1,3 MeV and 4 MeV to 9 MeV* (International Organization for Standardization, Geneva, Switzerland1997)

[61] ISO 4037-3:1999. *X and gamma reference radiation for calibrating dosemeters and doserate meters and for determining their response as a function of photon energy – Part 3: Calibration of area and personal dosemeters and the measurement of their response as a function of energy and angle of incidence* (International Organization for Standardization, Geneva, Switzerland1999)

[62] ISO 8529-3:1998. *Reference neutron radiations – Part 3: Calibration of area and personal dosimeters and determination of response as a function of energy and angle of incidence* (International Organization for Standardization, Geneva, Switzerland1998)

[63] IAEA Technical Reports Series 403. *Compendium of Neutron Spectra and Detector Responses for Radiation Protection Purposes Supplement to TRS 318* (International Atomic Energy Agency2001)

[64] A. Fiechtner. *Messung von thermischen Neutronen mit CR-39-Detektoren*. Tech. Rep. TM-96-05-03, Paul Scherrer Institut (PSI), Villigen, Switzerland (2005)

[65] S. F. Kry, U. Titt, D. Followill, F. Poenisch, O. N. Vassiliev, R. A. White, M. Stovall, and M. Salehpour. *A Monte Carlo model for out-of-field dose calculation from high-energy photon therapy*. Medical Physics, **34**, 3489–3499 (2007)

[66] B. Clasie, A. Wroe, H. Kooy, N. Depauw, J. Flanz, H. Paganetti, and A. Rosenfeld. *Assessment of out-of-field absorbed dose and equivalent dose in proton fields*. Medical Physics, **37**, 311–321 (2010)

[67] R. M. Howell, S. F. Kry, E. Burgett, N. E. Hertel, and D. S. Followill. *Secondary neutron spectra from modern Varian, Siemens, and Elekta linacs with multileaf collimators*. Medical Physics, **36**, 4027–4038 (2009)

[68] A. Zanini, E. Durisi, F. Fasolo, C. Ongaro, L. Visca, U. Nastasi, K. W. Burn, G. Scielzo, J. O. Adler, J. R. M. Annand, and G. Rosner. *Monte Carlo simulation of the photoneutron field in linac radiotherapy treatments with different collimation systems*. Physics in Medicine and Biology, **49**, 571–582 (2004)

[69] M. P. Little. *Estimates of neutron relative biological effectiveness derived from the Japanese atomic bomb survivors*. International Journal of Radiation Biology, **72**, 715–726 (1997)

[70] H. Paganetti, A. Niemierko, M. Ancukiewicz, L. E. Gerweck, M. Goitein, J. S. Loeffler, and H. D. Suit. *Relative biological effectiveness (RBE) values for proton beam therapy*. International Journal of Radiation Oncology, Biology, Physics, **53**, 407–421 (2002)

[71] R. D. Timmerman and M. Mendonca. *In regard to Donaldson et al: Results from the IRS-IV randomized trial of hyperfractionated radiotherapy in children with rhabdomyosarcoma — A report from the IRSG. IJROBP 2001;51 : 718-728*. International Journal of Radiation Oncology, Biology, Physics, **54**, 1579–1580 (2002)

[72] British Institute of Radiology. *Central axis depth dose data for use in radiotherapy*. British Journal of Radiology. Supplement, **11**, 1–110 (1972)

[73] R. A. Hälg, J. Besserer, and U. Schneider. *Comparative simulations of neutron dose in soft tissue and phantom materials for proton and carbon ion therapy with actively scanned beams*. Medical Physics, **38**, 3149–3156 (2011)

[74] A. Fiechtner, K. Gmür, and C. Wernli. *A personal neutron dosimetry system based on etched track and automatic readout by Autoscan 60*. Radiation Protection Dosimetry, **70**, 157–160 (1997)

[75] P. J. Gilvin, D. T. Bartlett, and J. D. Steele. *The NRPB PADC neutron personal dosimetry service*. Radiation Protection Dosimetry, **20**, 99–102 (1987)

[76] A. Fiechtner. *Bestrahlung von cr39-neutronendetektoren mit hochdosisphotonenstrahlung*. Tech. Rep. AN-96-02-16, Paul Scherrer Institut (2002)

[77] R. A. Hälg, J. Besserer, M. Boschung, S. Mayer, B. Clasie, S. F. Kry, and U. Schneider. *Field calibration of PADC track etch detectors for local neutron dosimetry in man using different radiation qualities*. Nuclear Instruments & Methods in Physics Research, Section A: Accelerators, Spectrometers, Detectors, and Associated Equipment, **694**, 205–210 (2012)

[78] R. A. Hälg, J. Besserer, M. Boschung, S. Mayer, and U. Schneider. *Monitor units are not predictive of neutron dose for high-energy imrt*. Radiation Oncology, **7**, 138 (2012)

[79] M. Stovall, C. R. Blackwell, J. Cundiff, D. H. Novack, J. R. Palta, L. K. Wagner, E. W. Webster, and R. J. Shalek. *Fetal dose from radiotherapy with photon beams: Report of AAPM Radiation Therapy Committee Task Group No. 36*. Medical Physics, **22**, 63–82 (1995)

[80] R. A. Hälg, J. Besserer, and U. Schneider. *Systematic measurements of whole-body imaging dose distributions in image-guided radiation therapy*. Submitted to Medical Physics (2012)

[81] R. A. Hälg, J. Besserer, and U. Schneider. *Systematic measurements of whole-body dose distributions for various treatment machines and delivery techniques in radiation therapy*. Submitted to Medical Physics (2012)

[82] S. F. Kry, R. M. Howell, U. Titt, M. Salehpour, R. Mohan, and O. N. Vassiliev. *Energy spectra, sources, and shielding considerations for neutrons generated by a flattening filter-free Clinac*. Medical Physics, **35**, 1906–1911 (2008)

[83] K. Otto. *Volumetric modulated arc therapy: IMRT in a single gantry arc*. Medical Physics, **35**, 310–317 (2008)

[84] O. Cahlon, M. Hunt, and M. J. Zelefsky. *Intensity-modulated radiation therapy: Supportive data for prostate cancer*. Seminars in Radiation Oncology, **18**, 48–57 (2008)

[85] E. J. Hall. *Intensity-modulated radiation therapy, protons, and the risk of second cancers*. International Journal of Radiation Oncology, Biology, Physics, **65**, 1–7 (2006)

[86] S. D. Davis, C. K. Ross, P. N. Mobit, L. Van der Zwan, W. J. Chase, and K. R. Shortt. *The response of LiF thermoluminescence dosemeters to photon beams in the energy range from 30 kV x rays to Co-60 gamma rays*. Radiation Protection Dosimetry, **106**, 33–43 (2003)

[87] L. Duggan, C. Hood, H. Warren-Forward, M. Haque, and T. Kron. *Variations in dose response with x-ray energy of LiF:Mg,Cu,P thermoluminescence dosimeters: Implications for clinical dosimetry*. Physics in Medicine and Biology, **49**, 3831–3845 (2004)

[88] C. R. Edwards, P. J. Mountford, S. Green, J. E. Palethorpe, and A. J. Moloney. *The low energy x-ray response of the LiF:Mg:Cu:P thermoluminescent dosemeter: a comparison with LiF:Mg:Ti.* British Journal of Radiology, **78**, 543–547 (2005)

[89] L. Freire, A. Calado, J. V. Cardoso, L. M. Santos, and J. G. Alves. *Comparison of LiF (TLD-100 and TLD-100H) detectors for extremity monitoring*. Radiation Measurements, **43**, 646–650 (2008)

[90] C. R. Edwards and P. J. Mountford. *Near surface photon energy spectra outside a 6 MV field edge*. Physics in Medicine and Biology, **49**, N293–N301 (2004)

[91] S. B. Scarboro, D. S. Followill, R. M. Howell, and S. F. Kry. *Variations in photon energy spectra of a 6 MV beam and their impact on TLD response*. Medical Physics, **38**, 2619–2628 (2011)

[92] J. D. Ruben, C. M. Lancaster, P. Jones, and R. L. Smith. *A comparison of out-of-field dose and its constituent components for intensity-modulated radiation therapy versus conformal radiation therapy: Implications for carcinogenesis*. International Journal of Radiation Oncology, Biology, Physics, **81**, 1458–1464 (2011)

[93] L. B. Travis, M. Gospodarowicz, R. E. Curtis, E. A. Clarke, M. Andersson, B. Glimelius, T. Joensuu, C. F. Lynch, F. E. van Leeuwen, E. Holowaty, H. Storm, I. Glimelius, E. Pukkala, M. Stovall, J. F. Fraumeni, J. D. Boice, and E. Gilbert. *Lung cancer following chemotherapy and radiotherapy for Hodgkin's disease*. Journal of the National Cancer Institute, **94**, 182–192 (2002)

[94] R. A. Hälg, J. Besserer, M. Boschung, S. Mayer, and U. Schneider. *Measurements of neutron dose for various radiation qualities, treatment machines and delivery techniques in radiation therapy*. Submitted to Physics in Medicine and Biology (2012)

[95] S. F. Kry, M. Price, D. Followill, F. Mourtada, and M. Salehpour. *The use of LiF (TLD-100) as an out-of-field dosimeter*. Journal of Applied Clinical Medical Physics, **8**, 169–175 (2007)

[96] M. J. Murphy, J. Balter, S. Balter, J. A. BenComo, Jr., I. J. Das, S. B. Jiang, C.-M. Ma, G. H. Olivera, R. F. Rodebaugh, K. J. Ruchala, H. Shirato, and F.-F. Yin. *The management of imaging dose during image-guided radiotherapy: Report of the AAPM Task Group 75*. Medical Physics, **34**, 4041–4063 (2007)

[97] J. R. Perks, J. Lehmann, A. M. Chen, C. C. Yang, R. L. Stern, and J. A. Purdy. *Comparison of peripheral dose from image-guided radiation therapy (IGRT) using kV cone beam CT to intensity-modutated radiation therapy (IMRT)*. Radiotherapy and Oncology, **89**, 304–310 (2008)

[98] D. Yan. *Adaptive radiotherapy: Merging principle into clinical practice*. Seminars in Radiation Oncology, **20**, 79–83 (2010)

[99] S. S. Samant, J. Xia, P. Muyan-Oezcelilk, and J. D. Owens. *High performance computing for deformable image registration: Towards a new paradigm in adaptive radiotherapy*. Medical Physics, **35**, 3546–3553 (2008)

[100] G. X. Ding, D. M. Duggan, and C. W. Coffey. *Accurate patient dosimetry of kilovoltage cone-beam CT in radiation therapy*. Medical Physics, **35**, 1135–1144 (2008)

[101] G. X. Ding and C. W. Coffey. *Radiation dose from kilovoltage cone beam computed tomography in an image-guided radiotherapy procedure*. International Journal of Radiation Oncology, Biology, Physics, **73**, 610–617 (2009)

[102] M. Stock, A. Palm, A. Altendorfer, E. Steiner, and D. Georg. *IGRT induced dose burden for a variety of imaging protocols at two different anatomical sites*. Radiotherapy and Oncology, **102**, 355–363 (2012)

[103] G. X. Ding, D. M. Duggan, and C. W. Coffey. *Characteristics of kilovoltage x-ray beams used for cone-beam computed tomography in radiation therapy*. Physics in Medicine and Biology, **52**, 1595–1615 (2007)

[104] G. X. Ding and C. W. Coffey. *Beam characteristics and radiation output of a kilovoltage cone-beam CT*. Physics in Medicine and Biology, **55**, 5231–5248 (2010)

[105] P. Downes, R. Jarvis, E. Radu, I. Kawrakow, and E. Spezi. *Monte Carlo simulation and patient dosimetry for a kilovoltage cone-beam CT unit*. Medical Physics, **36**, 4156–4167 (2009)

[106] S. L. Dong, T. C. Chu, G. Y. Lan, T. H. Wu, Y. C. Lin, and J. S. Lee. *Characterization of high-sensitivity metal oxide semiconductor field effect transistor dosimeters system and LiF:Mg,Cu,P thermoluminescence dosimeters for use in diagnostic radiology*. Applied Radiation and Isotopes, **57**, 883–891 (2002)

[107] C. R. Ramsey, R. Seibert, S. L. Mahan, D. Desai, and D. Chase. *Out-of-field dosimetry measurements for a helical TomoTherapy system*. Journal of Applied Clinical Medical Physics, **7**, 1–11 (2006)

[108] O. Jäkel, D. Schulz-Ertner, C. P. Karger, A. Nikoghosyan, and J. Debus. *Heavy ion therapy: Status and perspectives*. Technology in Cancer Research & Treatment, **2**, 377–387 (2003)

[109] O. Jäkel, C. P. Karger, and J. Debus. *The future of heavy ion radiotherapy*. Medical Physics, **35**, 5653–5663 (2008)

Acknowledgements

Entering the field of medical physics for my doctoral thesis was a very exciting experience, following the diploma thesis in particle physics at DESY in Hamburg. I felt like a little boy when suddenly all my Christmases came at once. I can use a linear accelerator all on my own? Awesome!

This enthusiasm stayed for the whole time of my doctoral studies and this has been certainly not only because of the linear accelerator at hand. I am very thankful that this thesis has not only been demanding but also a great experience. Beside getting to know the spirit of radiation oncology, where multidisciplinary teams work together for the benefit of the patient, I have been introduced to many interesting people. Many people have contributed their share to the completion of my thesis. A lot of things would have not been possible without the great help and support I received during this time. At this point I would like to thank all of those people.

Firstly, I would like to thank Prof. Dr. Antony 'Tony' Lomax for making this doctoral thesis possible and for supervising me. Despite his very busy agenda, he has always had a sympathetic ear for my questions, problems, and demands. Although my working place has not been at Paul Scherrer Institut, I always felt as a part of the group at PSI and it has been like coming home when I visited.

Special thanks go to Prof. Dr. Uwe Schneider who is simply the best mentor a doctoral student can think of. The countless hours we spent together thinking about experiments, performing measurements, travelling for measurements and conferences, and writing manuscripts will always be joyful memories. I learnt so many things from him not limited to good practise in medical physics and science in general, but for instance also to appreciate excellent Bavarian wheat beer. I am very happy and proud to have you as my twin! Thank you!

Sincere thanks are due to Jürgen Besserer for asking the right questions and his innumerable ideas to get further insights into the subjects. I have always benefited a lot from his outstanding explanations no matter if it was in the middle of the night or during weekends. If there is something like a human encyclopedia, then it would definitely be him. I am very grateful that I have the opportunity to work with him and really enjoyed our trips together with Pierre for the measurements at the different institutions. You are a great person! Thank you!

I am also indebted to Prof. Dr. Bertram Batlogg for being part of my committee and Prof. Dr. Andreas Vaterlaus for being the representative of the Department of Physics. I am happy that they accepted being my co-examiners and want to thank them for their feedback.

Further, I would like to thank PD Dr. Raphaël Moeckli for being my co-examiner, for his feedback, and for his help to perform the measurements in Lausanne.

I enjoyed the collaboration with the Division for Radiation Protection and Security at

the Paul Scherrer Institut for the neutron dose measurements. Namely I want to thank Dr. Sabine Mayer and Markus Boschung for the constructive discussions, their help and support and last but not least for the supply of the numerous detectors needed for all the neutron measurements.

For financial support I thank the Federal Office of Public Health (BAG) and personally Dr. Philipp Trueb.

I would like to express my gratitude to the following people for their help to perform the measurements at the different institutions or the calibration of the neutron detectors:

- Miriam Gantert, Shaka Khan, and Dr. Gerd Lutters from Canton Hospital Aarau
- Samuel Peters and Dr. Hans Schiefer from Canton Hospital St. Gallen
- Dr. Andreas Joosten from Centre Hospitalier Universitaire Vaudois, Lausanne
- Dr. Desiree Klass and Dr. Peter Pemler from City Hospital Triemli, Zurich
- Dr. Stephen F. Kry from MD Anderson, Houston
- Dr. Benjamin Clasie, Dr. Martijn Engelsman, and Dr. Jay Flanz from MGH, Boston
- Alexander Lehde and Dr. Carlo Algranati from Paul Scherrer Institut, Villigen
- Peter Nobis and PD Dr. Dr. Andreas Mack from Radiotherapie Hirslanden AG, Zurich
- Stephanie Lang and Jan Hrbacek from University Hospital Zurich

I am pleased with the openness in the evaluation of devices and the thoughtful and impartial response to the results. I would like to thank everybody in the field who has helped to maintain this spirit of openness.

I want to say thank you to the whole Department of Radiation Oncology and Nuclear Medicine at the City Hospital Triemli for the great time I spent there.

A warm thank you goes to the whole teams at the Radiotherapy Hirslanden AG in Aarau and Zurich. I have always been met with a kind reception and the social events are always fun with you guys.

A big thank you goes to Anne Marie MacArtain for so many things. She is a great office mate and a good friend. I will always remember the great times we shared. She helped me a lot by proof reading nearly every sentence I wrote in the past months with diligence and patience.

I want to thank Dr. Martin Hoffmann, who has been sharing his computer skills with me unhesitatingly, Dr. Robert Jördens, who explained so many different things to me with a never ending endurance, and Dr. Stefan Kaufmann for proof reading and his good advice.

On a more personal note I want to thank my family and friends, especially my parents and my sister, who encouraged and supported me throughout my studies.